RICE UNIVERSITY

Low-Energy Charge and Spin Dynamics in Quantum Confined Systems

by

William D. Rice

A THESIS SUBMITTED
IN PARTIAL FULFILLMENT OF THE
REQUIREMENTS FOR THE DEGREE

Doctor of Philosophy

APPROVED, THESIS COMMITTEE:

Junichiro Kono, Chair
Professor of Electrical and Computer
Engineering and Physics and Astronomy

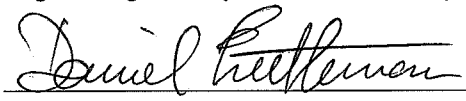

Daniel Mittleman
Professor of Electrical and Computer
Engineering

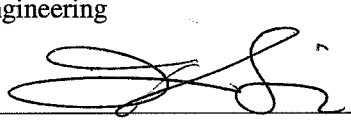

Qimiao Si
Professor of Physics and Astronomy

Houston, Texas

April, 2012

ABSTRACT

Low-Energy Charge and Spin Dynamics in Quantum Confined Systems

by

William D. Rice

Condensed matter systems exhibit a variety of dynamical phenomena at low energy scales, from gigahertz (GHz) to terahertz (THz) frequencies in particular, arising from complex interplay between charge, spin, and lattice. A large number of collective and elementary excitations in solids occur in this frequency range, which are further modified and enriched by scattering, interactions, and disorder. Recent advancements in spectroscopic methods for probing low-energy dynamics allow us to investigate novel aspects of charge and spin dynamics in solids. In this dissertation work, we used direct current (DC) conductivity, GHz, THz, and mid-infrared (MIR) techniques to provide significant new insights into interaction and disorder effects in low-dimensional systems. Specifically, we have studied temperature-dependent magnetoresistance (MR) and electron spin resonance (ESR) in single-wall carbon nanotubes (SWCNTs), intra-exciton scattering in InGaAs quantum wells, and high-field MIR-induced band gaps in graphene.

Temperature-dependent resistance and MR were measured in an ensemble of SWCNTs from 0.3 to 350 K. The resistance temperature behavior followed a 3D variable range hopping (VRH) behavior from 0.3 to $\sim$100 K. A positive MR was observed at temperatures above 25 K and could be fit with a spin-dependent VRH model; negative MR was seen at low temperatures. In the GHz regime, the ESR linewidth for SWCNTs was observed to narrow by as much as 50% as the temperature was increased from 3 to 300 K,

a phenomenon known as motional narrowing, suggesting that we are detecting the ESR of hopping spins. From the linewidth change versus temperature, we find the hopping frequency to be 285 GHz. For excitons in InGaAs quantum wells, we demonstrate the manipulation of intra-excitonic populations using intense, narrow-band THz pulses. The THz radiation temporarily quenches the $1s$ emission, which is then followed by an enhancement and subsequent decay of $2s$ emission. After the quenching, the $1s$ emission recovers and then eventually becomes enhanced, a demonstration of energy storage in intra-exciton states known as excitonic shelving. We show that the diffusive Coulomb scattering between the $2p$ and $2s$ states produces a symmetry breaking, leading to a THz-field-induced $1s$-to-$2s$ exciton population transfer.

Acknowledgments

First, I would like to sincerely thank Professor Junichiro Kono for his patience and insightful guidance. His support has been invaluable throughout the years. I have learned much from his deep and broad knowledge of research and condensed matter physics. Also, I would like to thank the committee members, Professors Daniel Mittleman and Qimiao Si; I am indebted to them for their input and guidance during this process.

I would not have been able to complete the ESR data without Dr. Ralph Weber of Bruker Biospin and Dr. Vladimir Burka and Professor Ah-lim Tsai both of the University of Texas Medical Center. The three of them have spent countless hours both teaching and working with me on the spin resonance project; they have also kindly extended themselves far beyond what was reasonable of me to ask.

Numerous people helped on the intra-excitonic scattering project. Without their continual, substantial, and important contributions this project would not have been possible: Stephan Winnerl, Martin Wagner, Jayeeta Bhattacharya, Sabine Zybell, Harald Schneider, Manfred Helm, and Joachim Wagner. The theoretical support for that project was almost entirely done by the group at Marburg, Germany: Mackillo Kira, Lukas Schneebeli, Benni Breddermann, and Stephan W. Koch.

The magnetoresistance project was greatly aided by Dr. Sebastian Nanot and Dr. Ivan Knez, who spent numerous hours discussing and working on this project with me. Also, I would like to thank Prof. Rui-Rui Du for allowing me to work in his lab to complete the low temperature, high-magnetic field transport work.

Without a doubt, I could not have survived this process without support from my labmates. A special mention should go out to Dr. Thomas Andrew Searles Jr., Dr. Darius Thomas Morris Jr., and G. Timothy Noe II for their friendship and help over the years. Additionally, I thank the **many** friends who have helped me keep my sanity when times were tough and made me laugh when I needed it most. Their backing was (and is) the reason that the last seven years have been so full of great memories. I thank all of them for their deep and abiding friendship and love.

Also, I would be remiss if I failed to specifically thank Dr. Jonathan Bruce Puritz Jr., Jessica Lin, Dr. Daniel MacArthur, Erin Arcand, Dr. Leslie Herrmann, Dr. Manuel Mendes, Britian Willingham, Dr. Jeffrey Worne, Dr. Victoria Astley, Dr. Budahipta Dan, Dr. Jose Castro, Dr. Maria Vidart, and Cary D'Alo Place for all of their generous support and friendship. In particular, I thank Dr. Jill Renee Delsigne for her constant support and understanding over the years; she has always been there for me both in good times and in bad. I also wish to specifically thank her for her insight on a broad range of subjects, including spiritually, on which she has taught me much. I also thank Liane Slaughter for her help, encouragement, love, and support over the last year, as well for her useful suggestions and careful reading of several of my written works.

Last, I wish to thank my family, especially my mother, father, and sister, for their understanding, encouragement, and backing. Their help, guidance, wisdom, insight, and love have been an unceasing and continual source of support for me. I thank them with all my heart.

Contents

Illustrations

Tables

Chapter 1

Introduction

Quantum wells (2D structures) and carbon nanotubes (1D structures) have emerged as two of the most physically interesting and technologically important reduced dimensional materials in condensed matter physics. In both cases, increased quantum confinement enhances the density of states (DOS) for collective and single-particle excitations, such as excitons, phonons, and plasmons. The augmented DOS provides for exciting, and in some cases exotic, observations of physical phenomena in a range of different experimental conditions. Strong electron-electron interactions in metallic SWCNTs, for example, have made them attractive candidates for Luttinger liquid physics (see, e.g., [1]). Meanwhile, quantum wells have continued to yield fascinating physical insights into many-body interactions, such as the recent work done on self-organized superfluorescence at high excitation fluences [2].

Most collective excitations in solids, e.g., plasmons, phonons, polarons, polaritons, occur in the gigahertz (GHz) to terahertz (THz) frequency range. Also, many resonance phenomena, such as electron spin resonance (ESR), cyclotron resonance (CR), intersubband transitions, exciton internal transitions, and superconductivity energy gaps, occur in the range. Furthermore, a number of dynamical processes in condensed matter, like carrier scattering, spin dephasing, and carrier tunneling, have time scales on the order of picoseconds to femtoseconds, corresponding to the THz frequencies. However, experimental investigations of the properties of these correlations have been hindered by the lack of low-energy excitation sources. The high-field, low-energy excitation regime is even more restrictive, with only a few sources, such as optical parametric amplifiers and free-electron

lasers, technologically developed enough for precise physical observations. Recent advances in high-field, table-top THz radiation sources [3–9] have only just now begun to open up this experimental region.

1.1 Thesis Outline

In this thesis, we use four different low-energy techniques to study a variety of charge and spin dynamics in low-dimensional systems. In Chapter 2, temperature-dependent resistance and magnetoresistance (MR) measurements are performed to study the hopping conduction of electrons in bulk SWCNT networks before and after thermal annealing. Since hopping conduction is a thermally driven process, the energy scale for this type of conduction mechanism is on the order of meV. By utilizing temperature-dependent MR, we were able to observe spin-dependent variable-range hopping (VRH) at high temperatures ($T \geq 100$ K) and weak localization at low temperatures ($T < 25$ K). At temperatures below 5 K, a positive MR component was observed at higher magnetic fields. A very thorough investigation of the temperature-dependent MR in this region shows that this positive contribution gradually becomes larger, eventually overwhelming the negative MR weak localization.

Chapter 3 shows our long-standing efforts in the ESR of ensembles of SWCNTs. Using a 9.6 GHz cavity resonator, we looked at the temperature-dependent ESR of acid-purified SWCNTs before and after thermal annealing. Interestingly, we observed a marked decrease in the ESR linewidth as the temperature was raised from 3 to 300 K. This phenomenon, which we identify as motional narrowing, results from the spin hopping of the ESR-active species in SWCNTs, a situation similar to the P-doped Si and Ge. Fitting to the temperature-dependent ESR linewidth gives a hopping energy for both the pre-annealed and post-annealed SWCNT sample conditions as $\sim$1.2 meV. Further, we observed that the spin susceptibility of the SWCNTs is substantially increased when physisorbed oxygen is

removed. This effect, which is reversible, suggests that the bulk ESR response is related to SWCNT defects. A localization length of the wavefunction is obtained through examining the ratio of the real and imaginary parts of the spin susceptibility, which follow a 3D VRH behavior at $T < 25$ K; we find the spin localization length to be $\sim$100 nm. Last, we present microwave power-dependent ESR curves as a function of temperature. An analysis of this data will lead to an extraction of the spin-lattice relaxation time. From these values as a function of temperature, we can reconstruct a spin-lattice relaxation mechanism.

In Chapter 4, we explore intra-excitonic population manipulation in InGaAs quantum wells using narrow-band, intense THz radiation generated from a free-electron laser. In the first experiment, we optically create excitons using a Ti:sapphire (Ti:Sa) picosecond laser. Several tens to hundreds of picoseconds later, we resonantly coupled the $1s$-$2p$ levels using 10.5 meV THz radiation and measure time-resolved photoluminescence (TRPL); the introduction of the THz pulse causes a temporary cessation of the $1s$ emission. Shortly after the $1s$ PL quench, an enhancement of the $2s$ emission is seen. When no external Coulombic interactions are present, the transfer of population from the $2p$ to the $2s$ state is forbidden on the grounds of conservation of angular momentum. However, a microscopic analysis of the system finds that the $2s$ emission can be traced back to many-body-induced symmetry breaking, which enables the diffusive Coulomb scattering between $2p$ and $2s$ exciton states. Since only a portion of the $2p$ population scatters into the $2s$ state, the non-emitting $2p$ state acts to feed the luminescing $1s$ state over the course of hundreds of picoseconds. The re-population of the $1s$ state allows the emission from that level to recover, and then become enhanced, over the course of roughly a nanosecond. This type of intra-excitonic energy storage using the dark $2p$ and bright $1s$ states is a demonstration of what we refer to as excitonic shelving.

The second experiment examines how the TRPL quenching responds to different THz

radiation conditions. We tune the THz photon energy around the $1s$-$2p$ (10.5 meV) energy to see how moving on and off this resonance changes the PL quenching efficacy. Since exciton formation takes several tens to hundreds of picoseconds, we also changed the time delay between the Ti:sapphire excitation pulse and the THz quenching pulse. At all THz wavelengths tested, we observed that the quenching became more prominent as the system moved from an electron-hole plasma to exciton-like. Generally, we see a trend towards larger PL quenching as the THz wavelength becomes longer. At certain pump-quench delay times, we performed THz radiation power dependence to see how the PL quenching responded to increased electric fields. When we were at long pump-quench delay times, we observed saturation of the quenching; at short pump-quench delay times, we do not. We tentatively attribute this observation to decreased electric field penetration due to electron-hole screening when the system is more plasma-like.

Chapter 5 explores our most recent effort in the low-energy regime: mid-infrared induced topological phase changes. We present the theoretical basis for this as-yet unexplored region of physics. Our current effort to build a mid-infrared pump, THz probe spectroscopy system is also presented, along with supporting information. We propose to observe optically-created band gaps in graphene, a 2D carbon lattice, using circularly-polarized, intense mid-infrared light. Since this state change is both transient and very large (zero-gap to a gapped system), we refer to this class of effects as non-perturbative, coherent topological changes. Finally, we will also attempt to observe recently predicted photo-induced topological phases or insulators in semiconductor quantum wells in the presence of a circularly-polarized mid-infrared laser field.

Chapter 2

Conductivity in Carbon Nanotube Networks: Hopping Transport

2.1 Introduction

Many groups have explored the electrical properties of single-wall carbon nanotubes (SWCNTs) from a pure-physics point of view, as well as for industrial and applied science applications (see, e.g., the review by Charlier *et al.* [10]). Because of their high optical phonon frequencies (1590 cm^{-1} or 197 meV), SWCNTs have weak backscattering from optical phonons, since the optical phonon population at room temperature (25 meV) is essentially negligible [11]. Therefore, only small momentum interband scattering is possible with phonons, making it the largest scattering source in single metallic SWCNTs [12]. Electron-electron scattering is the other major scattering mechanism in pure samples of SWCNTs, but this process necessarily implies the formation of a Luttinger liquid. Experimentally, the long mean free paths at room temperature (on the order of a micron [12]) and extremely high current carrying capacities (on the order of 10^9 A/cm^2 [13]) have led researchers to continue to attempt to scale up from the single nanotube limit to the bulk response.

The conductivity of ensembles of SWCNTs display a panoply of different behaviors for apparently similar conditions due to differences in alignment, preparation, length, chirality distribution, sample thickness, and contact material/configuration. As such, one of the most significant challenges to understanding conductivity in ensembles of SWCNTs is distinguishing between an extrinsic and intrinsic material response. In particular, the

presence of adsorbates in the system has yielded divergent interpretations. In 2000, Collins *et al.* experimentally showed that oxygen can substantially alter the conductance of bulk SWCNTs [14]. However, this observation was contradicted by Goldoni *et al.* [15], who demonstrated that the probe conductance could be changed by removing adsorbed particles from the contacts. Furthermore, Avouris and co-workers claimed that adsorbates change the Fermi energy relative to the contacts, producing a variable Schottky barrier that appeared like an adsorbate-dependent conductance change [11, 16].

Surprisingly, the magnetic field dependence of the conductivity, better known as magnetoresistance (MR), has not emerged as one of the prime tools used to understand ensemble SWCNT physics. Temperature-dependent MR gives information on both the localization length and the localization mechanism in a material. The application of a magnetic field may inhibit or enhance the conductive response of a condensed matter system depending on the microscopic structure of the material. Previous studies of MR in ensembles of SWCNTs found that 2D weak localization occurred at moderately low temperatures (10 K to 50 K) and that some sort of positive MR component manifested itself at very low temperatures (below 5 K) [17–20]. However, both the sample preparation (i.e., the inclusion of adsorbates) and the data density of temperature-dependent MR data inhibited the conclusions that the researchers could reach. In particular, both Kim *et al.* [18] and Cai and co-workers [19] had difficulty attributing the physical mechanism that produced the positive MR component.

In this chapter, we show a systematic comparison of both the resistance and magnetoresistance as a function of temperature between pre-annealed and post-annealed bulk SWCNTs. We find that for both sample conditions, the resistance shows a 3D variable-range hopping (VRH) temperature scaling across three orders of magnitude in temperature from 0.3 K to $\sim$100 K. This observation suggests that while adsorbed gases do affect trans-

port characteristics in SWCNTs, they do not lead to a cross-over from a 3D VRH scheme to a quasi-1D one. Upon annealing, the characteristic hopping temperature, T_0, rose from 30.9 K to 131 K, indicating that either the density of states at the Fermi energy or the localization length is decreased by removal of physisorbed molecules.

MR measurements were performed from 1.4 K to 250 K on both sample conditions. At temperatures above 25 K, a positive MR was seen for both the pre-annealed and post-annealed samples. We were able to fit these positive MR curves with a spin-dependent VRH model. From 25 K down to 1.4 K, a MR component proportional to $-H^2$ was observed, suggesting weak localization. Starting at 5 K, a positive MR component began to be seen at high magnetic fields. As the temperature was lowered, the positive MR contribution became visible at increasingly lower applied magnetic fields. The magnitude of this component also became increasingly larger as the temperature decreased, eventually causing the MR curve to go from ~ -0.04 at $T = 5.0$ K and $B = 6$ T to ~ 0.16 at $T = 1.43$ K and $B = 6$ T.

2.2 Background

In this project, the VRH conduction mechanism dominates the low temperature regime due to the lack of macroscopic crystal momentum conservation. This section is designed to give an introduction to the physics behind the VRH model. Given the breadth and depth of this field, we will attempt to simply illustrate the major motivation behind VRH physics and detail how it applies to this work.

2.2.1 Hopping Conduction

Typical conduction in crystalline solids occurs because of the very low scattering of electrons in the conduction band. The low scattering results from Bloch wavefunctions span-

ning the entire physical limits of the solid. These wavefunctions, which have the form $\exp(i\mathbf{k}\cdot\mathbf{r})$, are disrupted by a lack of translational invariance (from which momentum conservation arises) created by phonons (dynamic lattice displacements) and electron-electron interactions (prominent in clean low-dimensional structures and at low phonon densities). It is no surprise, therefore, that in metals, the conductivity grows substantially as the phonon density is reduced with decreasing temperature.

As one gradually increases the degree of disorder, translational invariance begins to break down: Bloch wavenumbers begin to no longer be good quantum numbers. Removing translational invariance creates destructive inferences of the constituent wavefunctions, ψ, that comprise the carrier wavefunction, Ψ [21]:

$$\Psi = \sum c_n \exp(i\mathbf{k}\cdot\mathbf{a}_n)\,\psi(|\mathbf{r}-\mathbf{a}_n|)$$
$$\Psi = \sum c_n \exp(i\phi_n)\,\psi(|\mathbf{r}-\mathbf{a}_n|)\,. \tag{2.1}$$

Here, k is the lattice vector, a_n are the lattice points, and c_n are constants. ϕ_n are the random phases that act to limit the extended nature of the unperturbed wavefunction. As the disorder of the lattice increases, Ψ becomes more confined, thus creating a localized state (Anderson localization). When large numbers of carriers become localized at a given energy E, these states form a narrow band near or at the Fermi energy (E_{F}) [22]. We can define an energy, E_{C}, at which states above this energy are delocalized and states below it are localized. If the Fermi energy goes below E_{C}, which is referred to as the mobility edge, conduction no longer occurs through delocalized states when $\varepsilon_2 = E_{\mathrm{C}} - E_{\mathrm{F}} < k_{\mathrm{B}}T$.

When localization is created by disorder, it is called Anderson localization, and it provides a basic starting point for our discussion on VRH. In such a localized system, if electrons can acquire enough energy, they can move to empty or singly occupied states. The energy for this hopping process comes from the thermal reservoir (phonons) and follows

an activation-type behavior, as first proposed by Miller and Abraham [23, 24]:

$$\sigma = \sigma_3 \exp\left(-\varepsilon_3 / k_B T\right), \tag{2.2}$$

where σ is the hopping conductivity, ε_3 is the mean energy between impurity sites, and σ_3 is the conductivity of impurity conduction at infinite temperature.

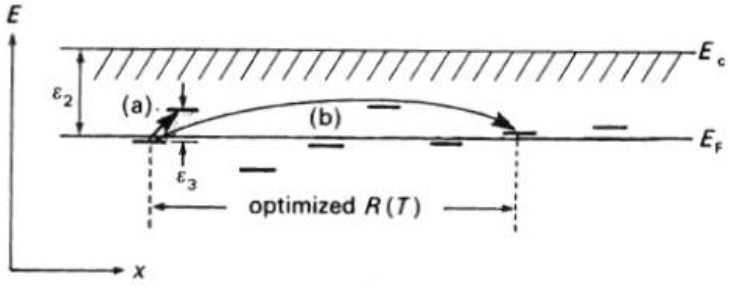

Figure 2.1 : When states are localized, i.e., E_F is below the mobility edge, E_C, two types of hopping can occur. (a) A typical activation-type hopping between neighboring sites, and (b) variable-range hopping can occur between non-adjacent sites. For (b), there is an optimized balance between the normalized energy, $\Delta E / k_B T$, and distance $R(T)/\xi$. Figure adapted from [24].

However, this activation-type model fails at low temperatures, because hopping can take place between spatially non-adjacent locations. When calculating the probability of a successful jump from one state to another, p, one actually needs to take into account the temperature-dependent spatial confinement of the electron, $R(T)$, as compared to the localization length, ξ, of the disorder-confined wavefunction [24]:

$$p = \nu_{ph} \exp\left(-2R/\xi - \Delta E / k_B T\right), \tag{2.3}$$

where ν_{ph} is the phonon density of states multiplied by the square of the electron-phonon matrix element and ΔE is the mean energy necessary to hop between sites. We can see the balancing of the spatial and energetic factors if we consider what happens when we have

a large $R(T)$: on the one hand, an increase in $R(T)$ allows for a better energy matching between hopping sites, but on the other, it decreases the probability of hopping [transfer integral $\propto \exp(-2R/\xi)$]. Figure 2.1 shows the qualitative difference between the Miller-Abraham approach (activation-type hopping) and the Mott VRH mechanism. Maximizing the transfer probability, p, we find that the resistivity, ρ_{hop}, gives a dimensionally dependent temperature dependence:

$$\rho \propto \exp\left[(T_0/T)^{1/(1+d)}\right], \tag{2.4}$$

where $T_0 = 18.1/[k_{\text{B}} * D(E_{\text{F}})\xi^3]$ and is known as the characteristic hopping parameter and d is the dimensionality of the system. This unique temperature dependence is one of the most important facets of the VRH model.

The hopping rate can quantitatively be written down in terms of four elementary hopping processes [24]: (1) singly occupied state to an empty state; (2) singly occupied state to another singly occupied state; (3) doubly occupied state to an empty state; and (4) doubly occupied state to a singly occupied state. Figure 2.2 shows these processes in the presence of intrastate interactions, which raise the doubly occupied state energy by an amount U above the singly occupied energy. Only processes within $k_{\text{B}}T$ of the Fermi energy, E_{F}, can occur, since each state is localized. The summation of hopping rates of these four processes makes up the total hopping rate. Quantitatively, this summation is usually not very useful; however, qualitatively, this model will help us to explain why positive MR occurs.

2.3 Experiment

Bulk SWCNT samples are very difficult to prepare properly, since the current SWCNT production methodologies create ferromagnetic catalyst containing nanotubes in powder form. Nanotube parameters, such as length, diameter, chirality, and alignment are difficult to control, producing very heterogeneous samples. In this section, we describe the steps

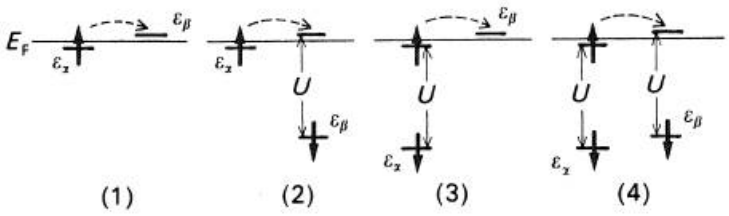

Figure 2.2 : The VRH conduction mechanism can be broken down into four elementary processes: (1) singly occupied to an empty state; (2) singly occupied to singly occupied state; (3) doubly occupied to an empty state; and (4) doubly occupied to a singly occupied state. The energy separation, U, represents the presence of intrastate interactions that raises the doubly occupied state energy by U. Figure adapted from [24].

taken to control some of these variables during sample preparation. Further, we discuss the design of the magnetoresistance setup and how the experiment was executed.

2.3.1 Sample Production

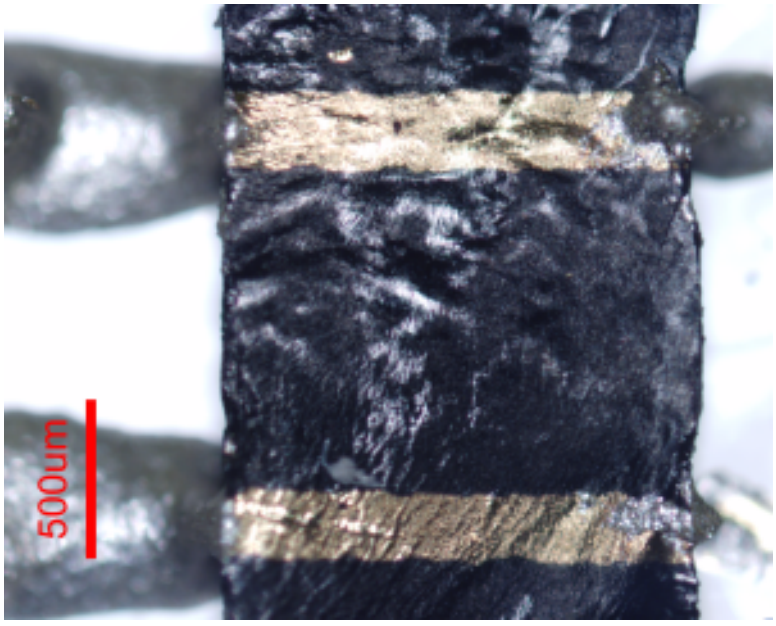

Figure 2.3 : Photograph of the actual sample used in the experiments. The 250 μm wide evaporated gold contacts were 1.01 mm away from one another. The sample was roughly 300 μm thick as measured using an optical microscope.

In previous studies, gold contacts were sputtered on top of the sample, which facilitated the generation of a current and the subsequent probing of the voltage. Given the thickness of our sample, we feared that replicating this procedure would generate a current that stayed only penetrated a portion of the sample before being detected by the voltage contacts. To avoid generating a current that might not fully propagate through the sample, we completely coated the ends of the rectangular sample with silver epoxy, which forced the current to move through the cross-sectional area of the sample. The epoxy also served to affix the sample to a 1-mm thick sapphire substrate, which we used to mount the sample assembly on the heater apparatus. The voltage was probed using 250 μm wide evaporated gold contacts that were banded around the sample on three sides (see Fig. 2.3). The gold contacts were spaced 1.01 mm apart from one another and were 50 nm thick. 25 μm gold wires were attached via silver epoxy to the current sources and the voltage probes. A picture of the sample with scale bars is given in Fig. 2.3.

We used acid purified laser oven tubes in powdered form procured from NASA [25]. To prepare the SWCNT sample, we utilized the same procedure as described later in Chapter 3 (see also [26,27]). The resulting SWCNT sample had a total material density of 0.38 g/cm^3, although from Nikolaev *et al.* [25] it is estimated that only $\sim$27% of the total mass is from SWCNTs.

2.3.2 Experimental Setup

The experiment was built around a Cryomagnetics, Inc. magnet with a Janis variable temperature insert (VTI) (see Fig. 2.4). The top field of the magnet was rated as 6.87 T at 4.24 K. The bore of the VTI was 1.5", which made sample positioning straightforward. We typically observed a decrease of 1% of the LHe volume per hour, where the total volume of the LHe in the magnet was $\sim$30 L.

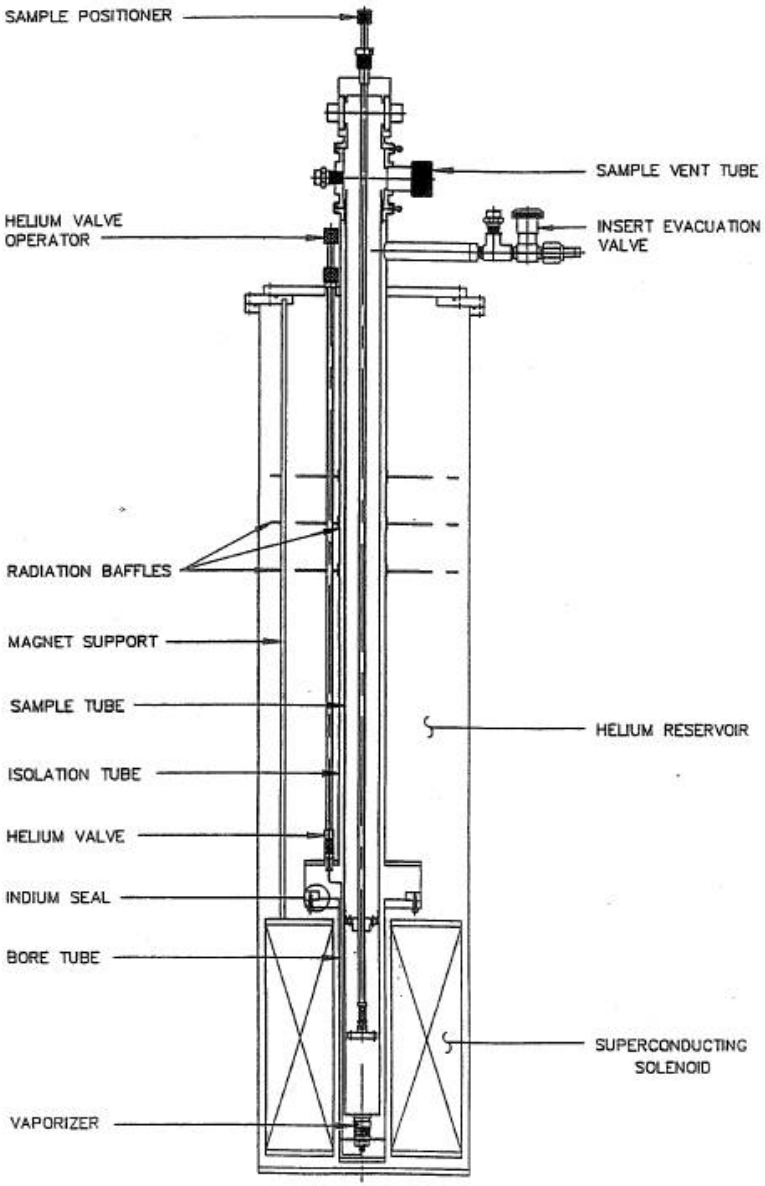

Figure 2.4 : Schematic of the 6 T magnet with the variable temperature insert from the Janis manual.

The top sample stick has three output pronged connections for various experiments. One is reserved for optical fibers (light pipes), while the other two we fashioned into 18 pin Fischer quick connections. Double-stranded P-Bronze wire was used to electrically connect the Fischer plugs to the sample via three, non-magnetic breakout stations. Although these breakouts were not entirely necessary, we found that at least two wire breakouts are very helpful in case of wire or bond breakages. The wires were wrapped around the stainless steel (316 series) stick with Teflon tape encasing them to hold everything in place. A homemade heater was attached to a sample mount at the end of the stick. We wrapped the heater using Nichrome, a resistive wire that is common for heater applications. To avoid generating magnetic fields via current being passed through the heater wire, we wrapped half of the wire for the heater in one direction and then half of it in the other direction, so as to have the heater-current-created magnetic fields cancel one another. To fix the wires in place, we used Stycast epoxy (1266 series). This epoxy is an excellent potting material, especially for cryogenic work, since its coefficient of thermal expansion at low temperature is very small ($\approx 3 \times 10^{-5}$ K^{-1}*).

The custom-made sample holder was designed specifically to hold a condensed ensemble of SWCNTs (see Fig. 2.5). It consisted of a G10 circular end piece that encased a copper assembly (denoted as the heater assembly in the figure) attached to the end of the sample stick. 35 brass (non-magnetic) pins penetrate the upper side of the G10 case. These provided the electrical feedthroughs from the last breakout on the sample stick into the G10 case. The sheer number of 0-80 thread brass pins was challenging to deal with because of the complexity of installation. However, we chose to design the apparatus to accommodate several different configurations. For the experiment described here, we needed 13 pins:

*Data obtained from the Lakeshore, Inc. website: http://www.lakeshore.com/products/cryogenic-accessories/epoxy/pages/Specifications.aspx

four for the Cernox temperature sensor, two for the heater, one for grounding the copper sample holder, and six for the sample.

To connect to the sample, six brass pins were attached directly to the sample holder, which sat just below the heater assembly. These pins were positioned very close to the sample (approximately a few mm's away) to minimize how far the 25 μm gold wire needed to go. Although we performed a four-point probe measurement, six pins were used as a practical matter due to the high possibility that at least one connection would fail/break. From the six pins, 25 μm gold wire was strung to the sample and attached via silver epoxy. To avoid shorting the wires to the copper sample holder, as well as to prevent the wires from breaking, we attached them using Stycast epoxy to the copper holder surface after they were silver epoxied into place. As mentioned above, the copper sample holder was grounded using a wire attached directly to the single-point ground at the breakout panel outside the magnet. A G10 cover sealed the entire sample assembly to avoid radiative heating and abrasive environment of the VTI.

For all of the measurements presented here up to 6 T (Janis magnet), two lock-in amplifiers (LIA) were used. One generated a time-varying signal at a given frequency and measured it across a known, large ($\approx$1 MΩ) resistor to obtain the sourced current, while the second LIA measured the voltage across the sample. A time constant of 1 second was used for most measurements, and the LIA frequency was set around 17 Hz. Due to the small resistance measured, we used 1 mA of sourcing current. This value is rather large, especially since heating effects are possible at the lowest temperatures. However, when I-V curve measurements were done, I_{source} = 1 mA was always found to be in the linear regime.

For the measurements in the larger magnet (8 T curves, Oxford magnet), which were performed in Professor Rui-Rui Du's lab in the Department of Physics and Astronomy at Rice University, only one LIA was used; its frequency was set to 23 Hz. I_{source} was set to

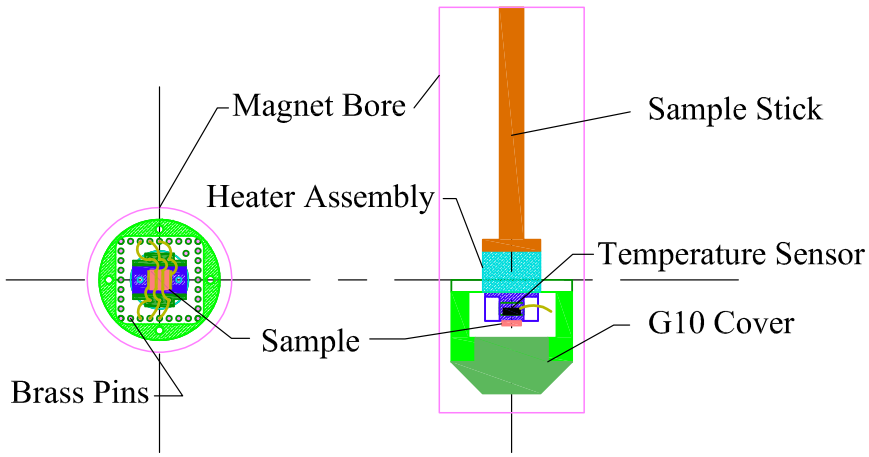

Figure 2.5 : Two schematic views of the sample holder that we designed for the conductivity experiment. The Cernox temperature sensor is held in the hole just below the sample in the figure at the right using GE varnish. At left, a head-on view of the sample, sample holder, and wire attachments. The G10 cover would normally obscure this view. At right, a side view of the bottom of the sample stick, showing the heater assembly, sample holder, and G10 cover.

100 μA, rather than 1 mA, since temperatures as low as 0.3 K were reached. A lower current was used for these measurements, since it was feared that the low temperatures would be affected by current heating (i.e., a combination of an increasingly large resistance, which approaches nearly 7 Ω at 0.3 K, and a high current).

The I-V curve measurements were performed using a Keithley 2400 sourcemeter that logarithmically increased the sourcing current, I_{source}. At currents above 10 mA, heating effects could sometimes be observed: a non-linear I-V trend at higher currents was presumed to indicate either localized or global sample heating.

To compare the non-annealed versus annealed sample conditions, we built an annealing tube outside the magnet. In addition, a small G10 roof was installed directly over the sample for the non-annealed portion of the temperature-dependent resistance and MR experiments. This piece was installed to hinder the escape of physisorbed species once the sample was placed into the magnet, since the partial pressure of gases is extremely small (except for He) within the magnet. The annealing tube was a simple construction: a stainless steel tube with a 1.75" inner diameter that was mounted vertically to the wall. A Ladish (now known as the Tri-Clamp series) fixture was built on the top of the tube, which allowed the sample stick to mate to the annealing tube in the same way it connected to the magnet. The heater on the sample stick was used to anneal the sample in a controlled way. A roughing vacuum and a tank of 99.99% argon were both hooked up to the annealing tube. For the first part of the annealing, the roughing vacuum pulled at full strength (total pressure estimated to be on the order of mTorr) for 12 hours while the sample was heated to $\sim$415 K. A very small flow of argon was streamed into the tube during this time. After 12 hours, the vacuum was nearly closed off and the pressure of the argon was raised to nearly 2 atm for another 12 hours. Because of increased gas flow, the PID of the temperature controller easily stabilized the sample temperature at 415 K. After this second 12 hour stretch, we moved the sample stick out of the annealing tube, quickly re-attached to the G10 cap on the sample assembly, and plunged the stick back into the magnet. Any gaseous adsorbates that attached themselves during this short interlude between the annealing and the re-entry into the magnet were believed to be removed by the vacuum pumping on the VTI.

2.4 Results

For each sample condition (pre-annealed or post-annealed), three major tests were performed: a logarithmic sweep of current ($I-V$ curve) at fixed temperatures (T), a steady

ramp of temperature between 1.3 K and 350 K, and temperature-dependent MR. The current sweeps were done at several temperatures spanning from 1.3 K to 250 K, which covered most of the probed temperature range. A typical plot of V_{measured} versus I_{source} is given in Fig. 2.6. A linear fit is applied to both curves to test for Ohmic behavior. At T = 1.254 K [Fig. 2.6(a)], a non-linear $I-V$ curve is seen at source currents approaching 10 mA, which suggests either localized or global heating. In contrast, when the lattice temperature is raised to 50 K, the curve is fully linear across the whole range.

To quickly estimate the heat load being placed on the sample, we can use simple thermodynamics. The resistance of the sample, R, at 1.3 K is $\approx 1\ \Omega$. Since $\Delta P = I^2 \times R$, where ΔP is the change in power, we can estimate that at I_{source} = 10 mA, $\Delta P = 10^{-4}$ W, or 10^{-4} J per second. The mass of the sample was measured to be $\sim$0.6 mg, which allows us to calculate the change in temperature of the sample, ΔT:

$$\begin{aligned} \Delta P &= mC_p\Delta T, \\ \Delta T &= \tfrac{\Delta P}{mC_p}, \\ \Delta T &= \tfrac{I^2R}{mC_p}. \end{aligned} \tag{2.5}$$

A rough estimate for C_p for an ensemble of SWCNTs at 1 K is on the order of 1 J/(g-K) [28]. Plugging these numbers into Eq. (2.5), we find $\Delta T \approx 0.1$ K. As we will see shortly, this change in temperature at 1.25 K corresponds to $\Delta R \sim -0.1\ \Omega$, which is significant enough to observe a deviation from linearity. Conversely, at T = 50 K, the change in ΔT is expected to be one order of magnitude lower, since C_p is $\approx$25 J/(g-K) [28]. A 0.01 K change in temperature causes a resistance change of $\sim 6 \times 10^{-4}\ \Omega$, which is nearly at our detection limit.

The temperature dependence of the electrical conductivity was one of the main aims of this experiment. We performed a temperature ramp directly after the sample was placed inside the magnet and just before it was removed to see how time inside a very low pressure

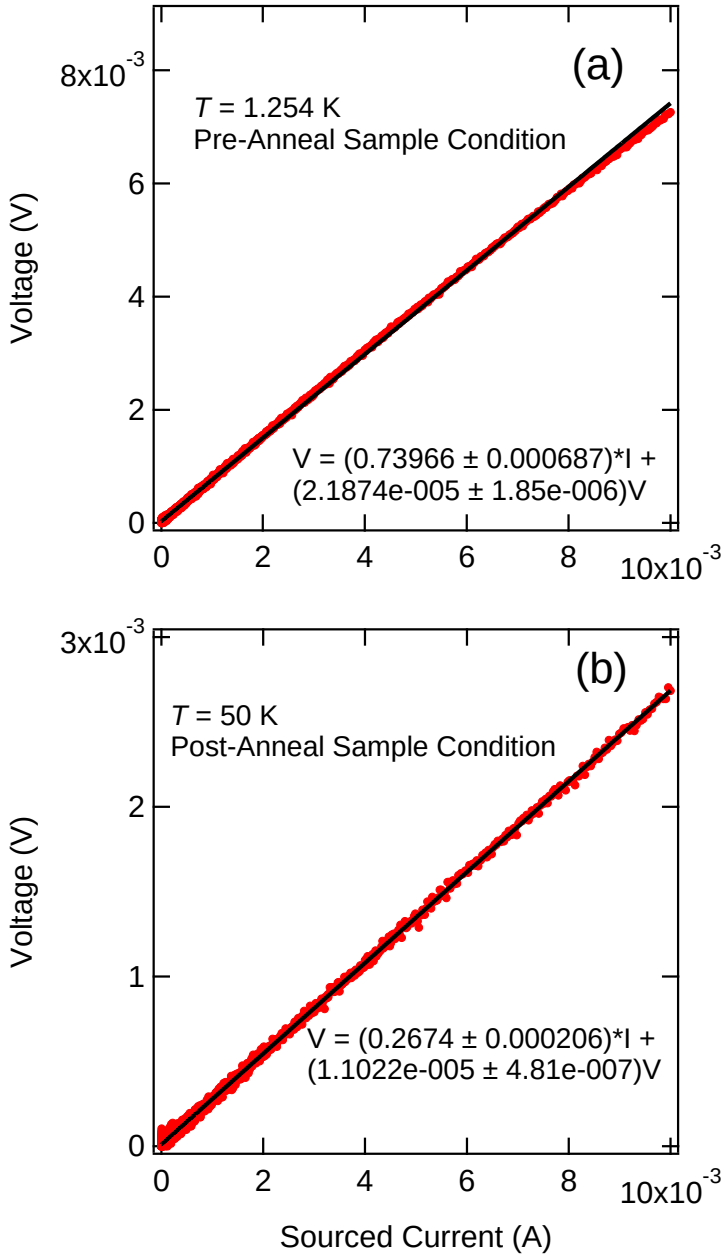

Figure 2.6 : Measured voltage versus sourced current for two temperatures. In (a), a clear non-linearity develops at the highest source currents, which is indicative of heating. In (b), the measured voltage is linear up to 10 mA, since the heating effect is minimized at the higher lattice temperature.

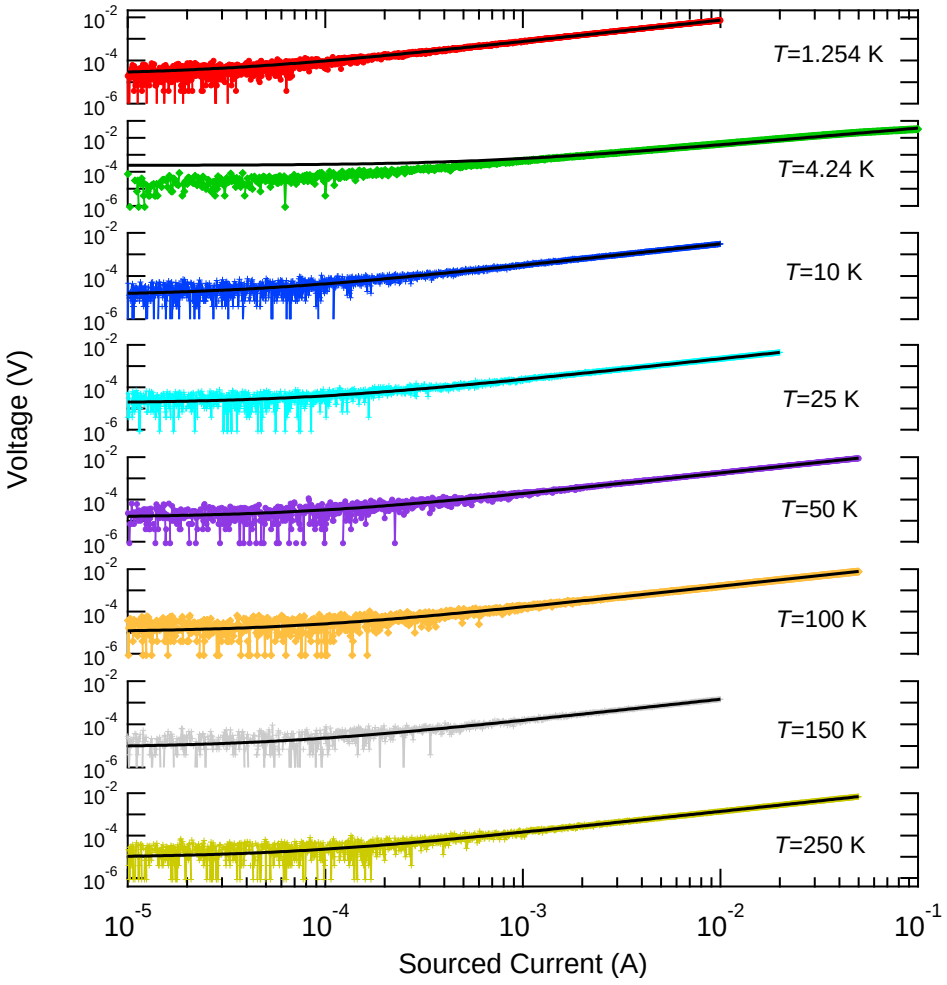

Figure 2.7 : Measured voltage versus sourced current for the non-annealed SWCNT sample for selected temperatures. A linear fit is applied to each curve, demonstrating that I_{source} = 1 mA is within the linear regime across the full temperature range.

environment affected the sample resistance. The temperature was ramped upwards from 1.35 K to 350 K very slowly: we used a ramp rate of 1 mK/sec at low temperatures and 20 mK/sec at the highest temperatures. By slowly changing the lattice temperature in this manner, a very accurate determination of the resistance as a function of temperature could be obtained.

Figure 2.8 shows the sample resistance (R)versus temperature for each temperature

ramp we performed. Two temperature-dependent resistance sweeps were done before the sample was annealed and two were done after annealing. In all cases, the sample resistance increases by an order of magnitude as the temperature is dropped from 350 K to 1.3 K. Interestingly, the resistance of the two pre-annealed temperature ramps are different from one another, while the two post-annealed ramps are the same. A small, reproducible kink in the resistance can be seen at 1.3 K. To test if this irregularity was real or not, we brought the sample (after re-annealing it using the same conditions described above) to a ^{3}He magnet. A moderately slow temperature ramp was done from 14 K down to 0.3 K, as seen in Fig. 2.10. The resistance displays a smooth rise upward, following the same trend seen in Fig. 2.8. The kink seen in the ^{4}He magnet is therefore an artifact.

The large increase in resistance with decreasing temperature suggests that we are observing conduction from a semiconductor or an insulator. In particular, given the observations of previous nanotube researchers [18–20], the most likely conduction mode is VRH. As shown in Fig. 2.9 where $\ln(R)$ is plotted against $T^{-1/4}$, we observed a 3D VRH behavior [$d = 3$ in Eq. (2.4)] up to 125 K. The 3D nature of the VRH suggests that the SWCNT-SWCNT coupling is rather strong, which may be a result of the high compaction densities that were used in the experiment (0.38 g/cm^3 total material density). For the pre-annealed sample, before any MR experiments were performed, we obtained a characteristic hopping temperature, T_0, of 30.9 K. This value rose to 36.4 K at the end of several days of experimentation. We attribute the higher value to decreased adsorbed gas species, such as molecular oxygen, caused by the very low partial pressure of the variable-temperature insert in the magnet. Upon annealing, T_0 rose substantially to 131 K, which is very similar to what Jaiswal *et al.* observed [29], but about a factor of two lower than the value reported by Kim *et al.* [18]. After annealing, we saw no change in the temperature dependence of the resistance before or after MR experiments were performed. This observation suggests that

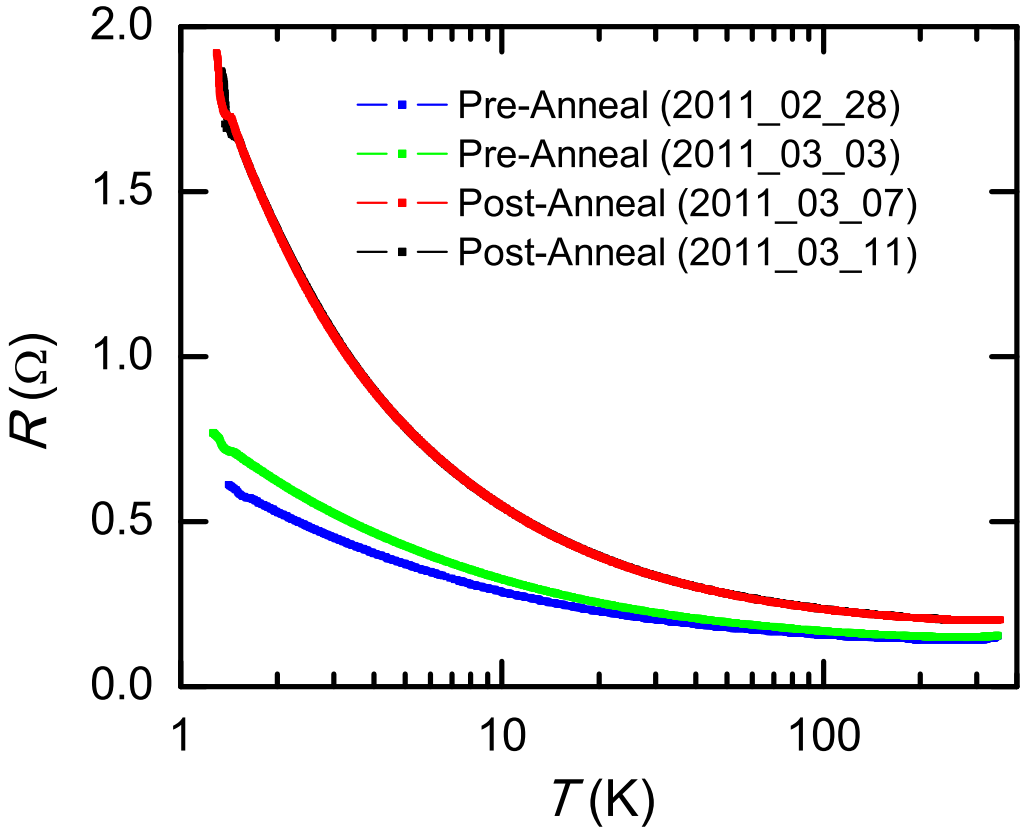

Figure 2.8 : Resistance of SWCNT sample versus temperature for each temperature scan. Before the anneal, the resistance day-to-day is not the same since adsorbates are being removed by the vacuum. After the anneal, the resistance is steady, since physisorbed molecules have been removed.

most of the adsorbed species have been removed by the lengthy, low-temperature thermal annealing procedure. An increased value of T_0 means that either $D(E_F)$ or ξ (or both) have decreased [see Eq. (2.4)]. If the adsorbates are lowering barriers between nanotubes, then it seems reasonable to believe that the removal of physisorbed species reduces ξ.

Figure 2.10 shows the results of temperature-dependent resistance from 14 K to 0.3 K after the sample had been annealed for a second time. We re-annealed the sample to remove the adsorbates that had reattached themselves after the sample had been sitting in atmosphere for over a year. The 3D VRH trend very nicely describes the resistance be-

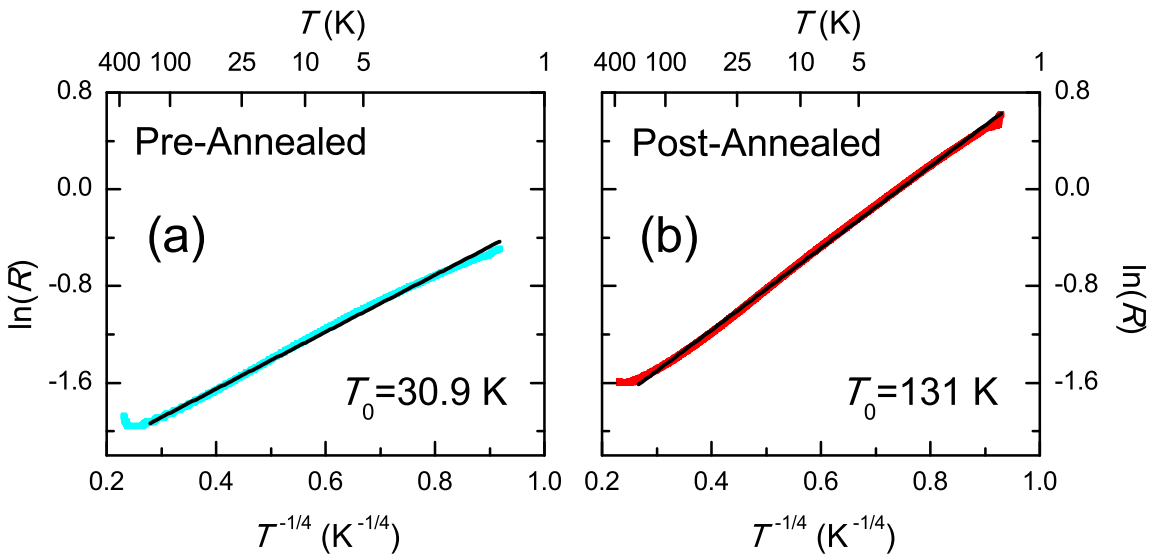

Figure 2.9 : Natural log of the resistance for the (a) pre-annealed (cyan curve) and (b) post-annealed (red curve) SWCNT sample versus $T^{-1/4}$ from $T \sim$1.3 K to T = 350 K. At $T <$125 K, a 3D VRH model fits the data very well, as evidenced by the linear fits to the data (black lines).

havior at low T, as indicated by the linear fit to the $\ln(R)$ versus $T^{-1/4}$ plot. We observe that T_0 = 126 K, which is very close to the value seen in Fig. 2.9(b), suggesting that both post-annealed sample conditions are similar to one another.

Taken together, our temperature-dependent resistance measurements show a 3D VRH behavior over three orders of magnitude. Although other groups have seen such a VRH temperature trend before [18–20,29,30], there is a substantial divergence on the dimensionality of the VRH scaling. Some groups have observed a Coulomb-gap type behavior [29], while others have seen 2D [18, 20] and 3D [30] VRH. In the studies done by Yanagi *et al.*, for example, a 2D VRH behavior makes sense, since they are using condensed, 2D-like SWCNT films. However, it is puzzling why Kim and co-workers observed the same scaling law in bulk SWCNT ensembles [18].

MR scans were done on the pre-annealed sample at several discrete temperatures from

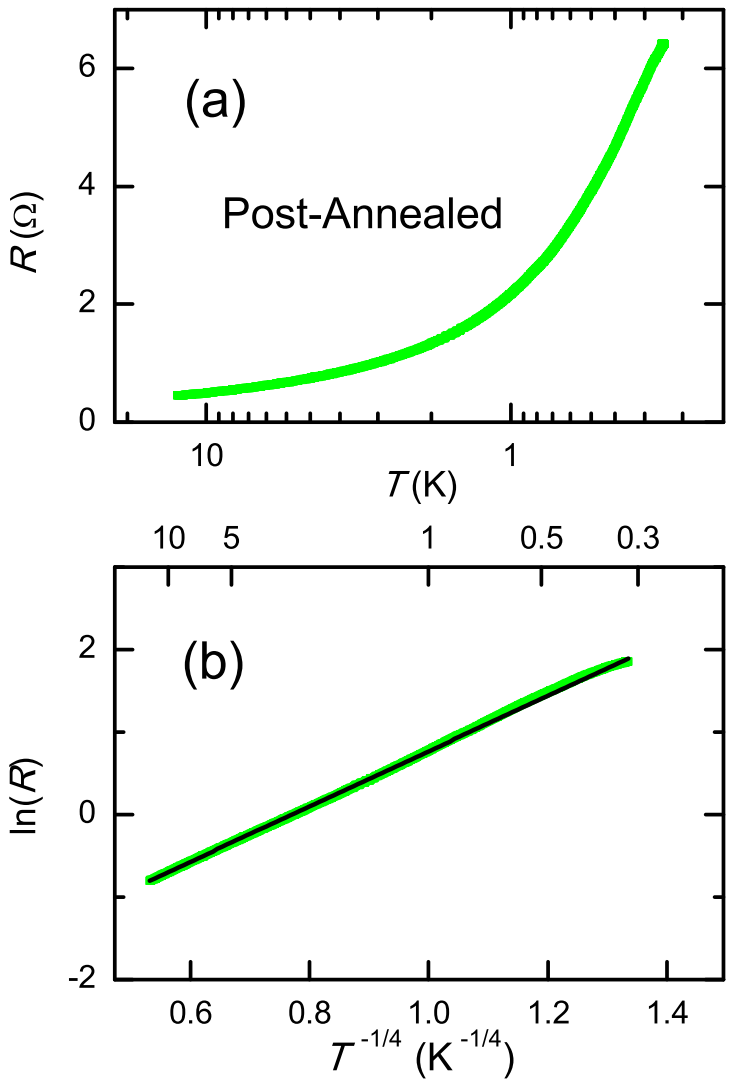

Figure 2.10 : (a) Log-log plot of R versus T from 0.3 K to 14 K. (b) Natural log of R plotted against $T^{-1/4}$ shows a very linear trend. A 3D VRH model fits very well to the data down to 0.3 K.

1.50 K to 250 K. MR is a measure of the change of the resistance with applied magnetic field, B, at a given temperature, T:

$$MR(B,T) \equiv \frac{R(B,T) - R(0,T)}{R(0,T)}, \tag{2.6}$$

where $R(0,T)$ is the resistance of the sample in no magnetic field. As shown in Fig. 2.11, a positive MR is observed at temperatures 50 K and above. At fields above 4.0 T, the 50 K dips below 0, beginning a trend of increasingly negative MR at lower temperatures. Negative MR is most prominently seen at T = 4.24 K, where it follows a $-B^2$ behavior. When the temperature is lowered to 1.50 K, a strong positive MR component is seen at $B > 2.0$ T. For all of the temperatures examined, the MR up to 6 T does not go above 0.005 or below -0.04. The step-like changes seen along the curve, especially for T = 1.50 K, are artifacts from the LIA. Different settings of the LIA frequency filter and integration time modify the duration and magnitude of these steps.

Figure 2.12(a) shows the post-annealed MR curves for $T \geq$25 K. For these MR curves, the data was averaged to improve the SNR. As with the pre-annealed sample condition, a positive MR is seen for $T >$25 K, with the 50 K MR curve becoming negative at $\sim$4.0 T. Starting in Fig. 2.12(a) and then continuing in Fig. 2.12(b), a clear transition from positive to negative MR is seen as T is reduced; the MR increasingly become negative until 6 K. Interestingly, the MR from 25 K to 12 K is linear, while from 10 K to 6 K, it is quadratic. This behavior may indicate that the lowest MR occurs at higher magnetic fields for higher temperatures; as T is decreased, the minimum of the MR moves to lower and lower fields.

As the temperature is further lowered, the MR displays a $-B^2$ behavior with an increasingly large positive MR component. Figure 2.12(c) clearly shows that the bottom of the MR both shifts to lower fields and occurs at smaller negative values as T is decreased. From 5 K to 1.43 K, we observe a marked shift in the MR: it goes from completely negative at 5 K to nearly completely positive at 1.43 K. Not only does the sign of the MR switch,

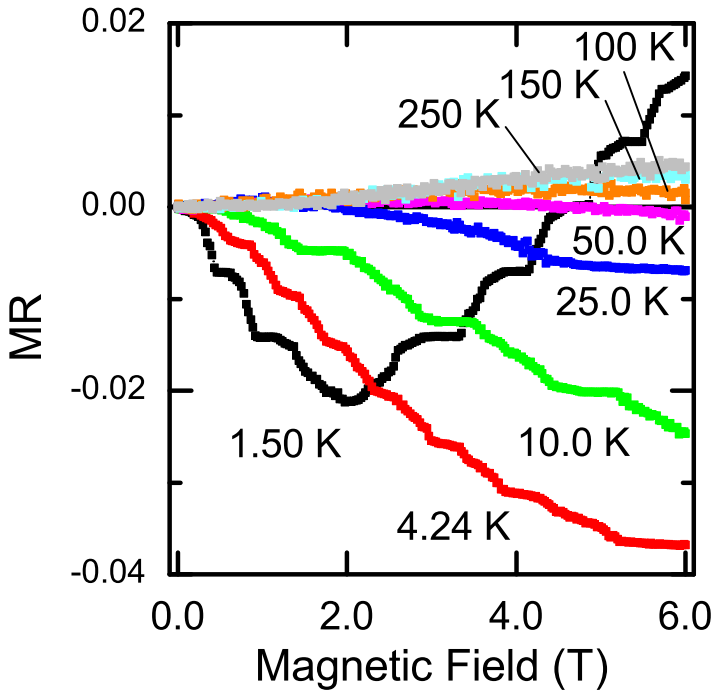

Figure 2.11 : Temperature-dependent MR curves from the pre-annealed SWCNT sample.

but the MR increases by an order of magnitude (~ -0.04 at 5 K to $\sim$0.16 at 1.43 K) by changing the thermal energy by a factor of 3.5.

2.5 Analysis

The clear observation of *positive* MR in bulk SWCNTs for both pre-annealed (Fig. 2.11) and post-annealed [Fig. 2.12(a)] SWCNTs at $T >$50 K is unique. To explain such behavior, we look at how VRH is altered in the presence of a magnetic field. In the Section 2.2.1, we saw how there were four fundamental processes that composed the VRH behavior. When a sufficiently strong magnetic field is present, the magnetic moments of the electrons align with the field, which adds a restriction to the hopping condition: two electrons can only

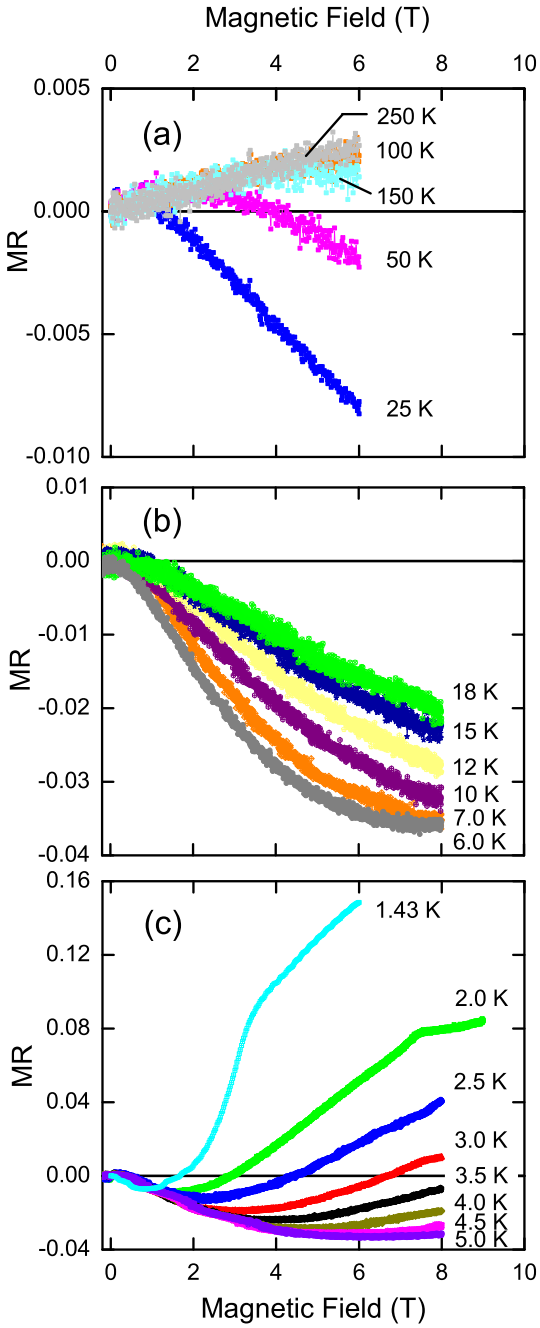

Figure 2.12 : Temperature-dependent MR curves from the post-annealed SWCNT sample for (a) $T \geq 25$ K (b) 25 K$> T \geq 6$ K and (b) $T < 6$ K.

doubly occupy a state if their spins are anti-parallel [24]. This added criterion limits the ability of the hops to already singly occupied states, meaning that half of the processes that compose the VRH mechanism now have reduced hopping rates. Thus, the resistance of the system will become larger. As the magnetic field increases, this Pauli blocking condition will only become harder to satisfy as the spins become fully polarized. However, at some field, spin polarization will become complete and the increased resistance will saturate [24].

We can quantitatively describe the changes of the MR with magnetic field, B, as [31,32]:

$$MR = \frac{A_{KK}}{1 + (B_{KK}/B)^2 - A_{KK}}, \tag{2.7}$$

where A_{KK} is the MR saturation value and B_{KK} is the characteristic magnetic field for spin alignment [18]. For 3D VRH, $A_{KK} = 1 - \exp\left[-b\left(\frac{T_0}{T}\right)^{1/4}\right]$ and $B_{KK} = \frac{ak_{\mathrm{B}}T\left(\frac{T_0}{T}\right)^{1/4}}{\mu_{\mathrm{B}}}$. Since we have already determined T_0, we only need to solve for a and b. We can condense the form further if we set $T^* = \left(\frac{T_0}{T}\right)^{1/4}$ and $M = \frac{k_{\mathrm{B}}T}{\mu_{\mathrm{B}}B}T^*$:

$$MR = \frac{1 - \exp(-bT^*)}{(aM)^2 + \exp(-bT^*)}. \tag{2.8}$$

We can fit Eq. (2.8) to our high-T magnetic field scans, as seen in Fig. 2.13. Despite only two parameters, the fits seem to describe the MR behavior very well. From the values of a and b that we extracted from the fitting, we find A_{KK} and B_{KK} for the pre-annealed and post-annealed sample conditions for T = 100, 150, and 250 K. These quantities, which are plotted in Fig. 2.14, show that both B_{KK} and A_{KK} become larger as T is increased. The trends hold well for the pre-annealed state much better than the post-annealed sample condition. The saturation MR agrees well in both magnitude and overall temperature trend with our findings in Fig. 2.13: the MR curves become more positive as the temperature is increased. The rise of B_{KK} with T is difficult to see in the data. However, we can make a physical argument that a higher field is needed to suppress the thermal agitation of the spins; therefore, it is natural to expect that B_{KK} rises with T. Indeed, if we follow this

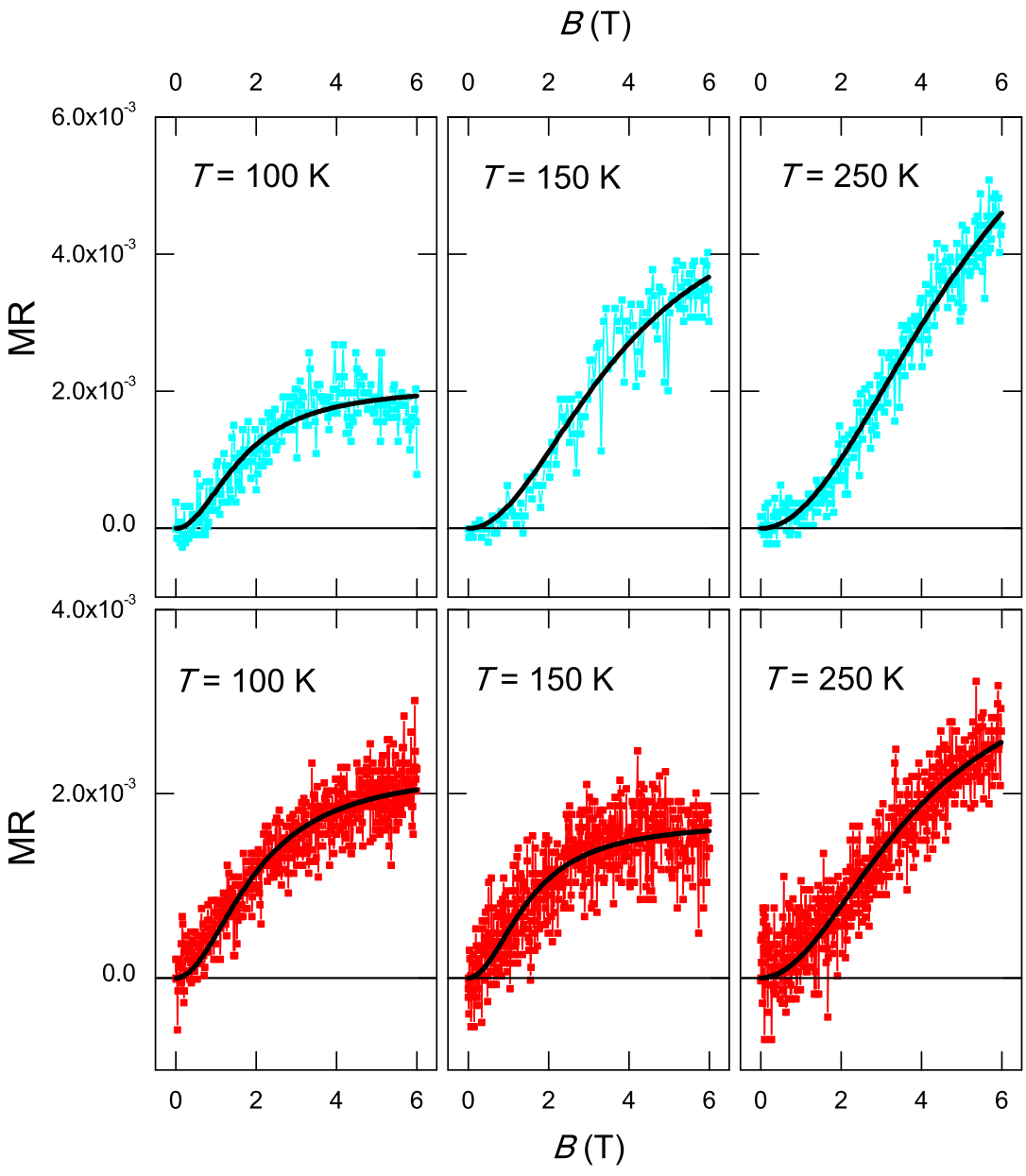

Figure 2.13 : MR for T = 100, 150, and 250 K. Top panels (cyan) show the MR versus magnetic field for the pre-annealed sample, while the bottom traces show the post-annealed MR. The black curves are the best fit lines from Eq. (2.8).

argument, since the thermal energy scales as $k_B T$, then so should B_{KK}. Although we only measured three temperatures for each sample condition, B_{KK} appears to scale linearly with (especially the post-anneal sample condition). More data over a wider thermal range is needed to substantiate this hypothesis.

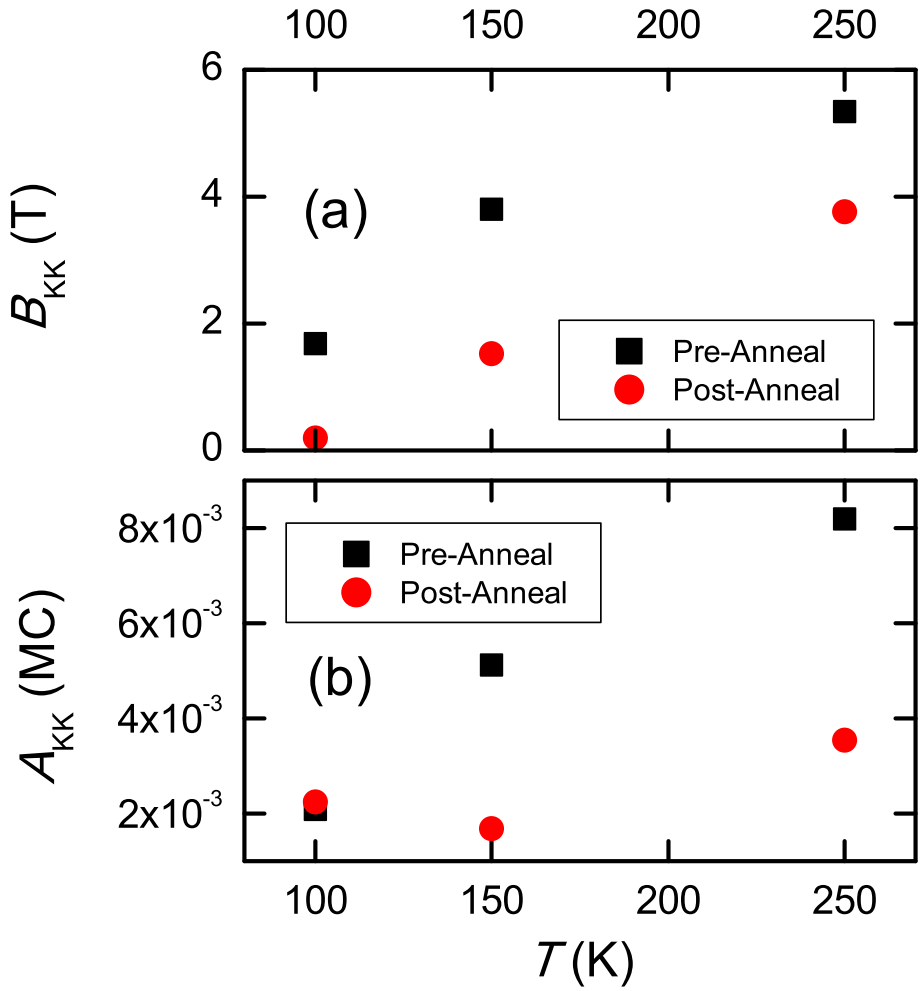

Figure 2.14 : The extracted quantities (a) B_{KK} and (b) A_{KK} for the pre-annealed (black squares) and post-annealed (red circles) versus T.

For the MR data at low T, we employ a simple scaling argument to forward the case that we are observing weak localization. For both the pre-annealed and post-annealed

curves at T <50 K, a linear or quadratic negative MR trend was observed. This behavior corresponds very closely to the observations made by both Kim *et al.* [18] and Vavro *et al.* [30]. In weak localization theory, a negative quadratic MR is seen when the magnetic field is smaller than the B_ϕ. We define B_ϕ as the field at which a flux unit, $\phi_0 = h/e = A_\phi B_\phi$, is created by threading the field through an area, $A_\phi \propto L_\phi^2$, where L_ϕ is the characteristic coherence length scale [30]. L_ϕ can be related to the temperature by $L_\phi \simeq aT^{p/2}$, where p is related to the orbital dephasing time, τ, by $\tau^{-1} \propto T^p$ [18]. Putting this altogether, we find $B_\phi = \frac{\phi_0}{4\pi} T^p$. Therefore, we should expect the value of B for which MR is proportional to $-B^2$ to decrease as T^p. If p is on the order of one, the negative, quadratic MR component will occur at smaller and smaller magnetic field ranges, a behavior we clearly see in panels (b) and (c) of Fig. 2.12. This scaling behavior needs to be quantitatively checked after the MR curves are fit before more can be said. However, as the rough qualitative argument indicated, we appear to be observing weak localization at low temperatures.

2.6 Conclusion

A 3D VRH trend was observed in both the pre-annealed and post-annealed sample conditions from ∼100 K down to 0.3 K. The characteristic hopping temperature increased by over a factor of four after thermal annealing, suggesting that either the localization length, ξ, or $D(E_F)$ is being reduced by the removal of adsorbates. Positive MR was observed for T >50 K. We were able to fit these curves using a spin-dependent 3D VRH model. We found that the saturation MR and the characteristic field both became larger as the temperature increased. Due to the data density and variability, only general conclusions could be reached. At low temperatures, a linear and then quadratic negative MR component was observed as temperature was decreased. We presented a scaling argument to show that this scaling qualitatively agrees with weak localization. Future steps include fitting the

low temperature data and establishing why a positive MR component occurs at the lowest temperatures investigated.

Chapter 3

Electron Spin Resonance in Single-Wall Carbon Nanotubes: Motional Narrowing

One of the most important fields in modern physics is dedicated to understanding spin dynamics in condensed matter systems [33–40] and applied devices [41,42]. Spin transport is a sensitive probe of many-body correlations, as well as an indispensable process for spintronics. When spins are dimensionally confined, especially to one dimension (1D), they are predicted to show strong correlations [35,36,38–40,43] and long coherence times [37]. Single-wall carbon nanotubes (SWCNTs) are ideal materials for studying 1D spin physics due to their long mean free paths and weak spin-orbit coupling [44]. Exotic spin properties in metallic SWCNTs at low temperatures and high magnetic fields have been predicted, including the appearance of a peak splitting in the spin energy density spectrum, which can be used to probe spin-charge separation in Luttinger-liquid theory [38–40].

Despite the predictions of unique and exciting spin-related phenomena, the spin properties of SWCNTs are still poorly understood. One of the most ubiquitous experimental methods for studying spin dynamics, electron spin resonance (ESR) spectroscopy, has been the prime method used to measure the spin dynamics of SWCNTs, since it provides information on spin-orbit coupling, phase relaxation time, spin susceptibility, and spin diffusion. However, there are substantial disagreements in the literature on SWCNT ESR linewidth, spin susceptibility, g-factor, and lineshape [26, 45–53]. In particular, the temperature dependence of the spin susceptibility of SWCNTs has been surprisingly difficult to reproduce [47, 49, 51]. The experimental evidence is so conflicting that even the ori-

gin of the ESR in SWCNTs is under substantial uncertainty, with certain authors claiming that it results from defects [46, 49, 53, 54] and others suggesting that it is intrinsic to nanotubes [47, 48, 51, 52, 55][†].

To complicate matters further, adsorbed molecular gas species, such as oxygen and hydrogen, have long been known to strongly affect spins in carbonaceous systems [56–62]. ESR studies done on adsorbed gas species in carbon nanotubes have focused solely on the adsorption of hydrogen [54, 55, 63–65], with only an ambiguous mention of oxygen effects in a polymer-SWCNT film sample [65]. Interestingly, adsorbed hydrogen produces an *increase* in the multi-wall carbon nanotube (MWCNT) ESR, while creating a *decrease* in the ESR signal in SWCNTs [63, 64]. These diametrically opposing trends are not currently understood, especially given the fact that the origin of the SWCNT ESR is still under considerable debate. However, many experimental studies have postulated that the signal from MWCNTs occurs from defects [54, 55, 63, 64], suggesting that hydrogen may not affect the intrinsic nanotube response. Several groups have utilized high temperature annealing of SWCNT samples to remove extraneous carbonaceous material [46, 47, 50], but a rigorous investigation of the role of adsorbed gas species has not been performed.

In this chapter, we show that adsorbed molecular oxygen has a considerable influence on the spin susceptibility of SWCNT ensembles, while having only a very small impact on spin movement. By looking at the ESR of SWCNTs as a function of temperature (T) both before (pre-annealed) and after (post-annealed) thermal annealing, we were able to quantitatively evaluate the impact of adsorbed oxygen spins in SWCNTs. Strikingly, we found that oxygen desorption increased the ESR signal by nearly a factor of four. When oxygen was added back to the system, the ESR signal was once again quenched, indicating

[†]Nafradi *et al.* [50] say the ESR signal is intrinsic to SWCNTs as well, but one co-author in private communications argues that is not what they meant in the paper

reversibility. Despite the change in signal intensity with oxygen, the spin hopping energy stayed around $\sim$1.2 meV for both annealing sample conditions. We hypothesize that the ESR SWCNT signal is due to *n*-type defects, which are compensated by *p*-type oxygen acceptor states when present in the sample.

We also present ESR data demonstrating that the probed spins in SWCNTs are localized species that undergo phonon-assisted hopping. Specifically, we find that the ESR linewidth becomes smaller as T is increased, a hallmark of the phenomenon of motional narrowing [66, 67]. This spin mobility accounts for the Dysonian lineshape [68] seen throughout the full T range examined. The Dysonian lineshape asymmetry parameter, which is proportional to the conductance of the probed spins, is shown to follow the 3D variable-range hopping (VRH) trend. From our ESR data, we find the density of states at the Fermi energy to be $\sim 10^{19}$ states/eV-cm^3, and we estimate the localization length of the spins to be $\sim$100 nm. Power-dependent ESR scans are also shown in this chapter, along with the corresponding weak Dysonian formulation including the spin-lattice relaxation time, T_1.

3.1 Materials and Methods

The sample consisted of acid-purified laser-oven SWCNTs obtained from NASA [25]. We used extreme care to prepare the SWCNT sample for ESR measurements, since both compaction density and particle looseness have an effect on the ESR signal. A pictorial scheme, given in Fig. 3.1, shows the steps taken to anneal the sample after it has been created. The powdered SWCNT ensemble was gently bath sonicated (Cole-Parmer, Model B3-R) at 12 W and a frequency of 55 kHz. Sonication lasted for two hours in water before the mixture was ultracentrifuged at 26000 rpm (an average force of 88000 g's using a Sorvall AH-629 rotor with 36 mL centrifuge tubes) for four hours. After ultracentrifugation, the supernatant was removed, and the resulting SWCNT pellet was extracted from the cen-

trifuge tube and placed into an open-air oven at 115°C for 15 minutes to remove most of the water. At this point, the pellet was dry enough to be handled as a solid unit. It was then placed into a dessicator for several days to create a water-free SWCNT pellet; this sample condition is denoted in the text as "pre-annealed." The 0.6 mg (0.38 g/cm^3) SWCNT pellet was held in a 3-mm diameter quartz ESR tube using a quartz wool.

The sample was then placed into a vacuum furnace kept at 115°C for 24 hours. For the first 12 hours, the pressure inside the furnace was maintained at 10-mTorr vacuum with a 250-sccm flow of purified argon; for the last 12 hours, the argon pressure was increased to $\approx$2 atm pressure with a 250-sccm argon flow. After the annealing, the ESR tube was partially filled with degassed mineral oil; the mechanical integrity of the pellet was completely preserved despite the addition of the mineral oil. While the mineral oil was being inserted into the ESR tube, a helium gas flow was simultaneously being applied so as to create a positively pressurized helium blanket. Both the mineral oil and the gas were introduced into the ESR tube while it lay in the furnace using 12" syringes. Helium gas was blanketed on top of the mineral oil before the ESR tube was mechanically sealed to prevent exposure to air. In the text, we refer to this sample condition as "post-annealed."

Temperature-dependent ESR measurements of the pellet were taken at discrete temperatures from $\sim$3 K to 300 K using a Bruker EMX X-band (9.6 GHz) spectrometer. An Oxford ESP900 cryostat with an ITC503 temperature controller and GFS600 transfer line was used for temperatures from 3.4 K to 100 K, and a BVT3000 temperature controller with a silver-coated double-jacketed glass transfer line was used for temperatures above 100 K. From 3 K to 100 K, 200 μW of microwave power was applied to the cavity; above 100 K, a microwave power of 1 mW was used. To ensure that we were in the linear power regime, we performed power dependence from 6 μW to 200 mW at temperatures from 4 K to 100 K and from 50 μW to 200 mW at temperatures from 125 K to 300 K. The ESR signal

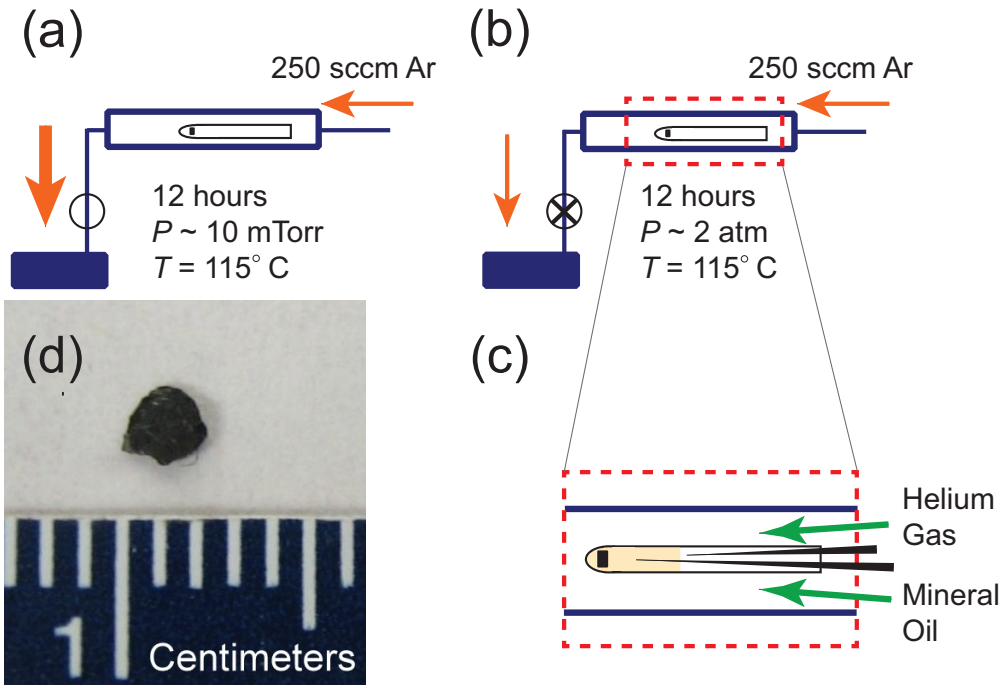

Figure 3.1 : The steps for annealing the sample are given in (a)–(c). (a) First 12 hour anneal stage with T=115°C and pressure held at 10 mTorr with a 250 sccm argon flow (argon gas flow indicated by the orange arrows). (b) Second 12 hour anneal stage. For this step, we raised the pressure inside the furnace to 2 atm with the vacuum valve held open just enough to keep the pressure steady. (c) To insure that oxygen did not re-contaminate the sample during ESR measurements, we backfilled the ESR tube with degassed mineral oil while streaming helium gas before the sample was removed from the furnace. (d) A picture of the sample before it was placed inside the ESR tube. Figure adapted from [27].

was not saturated until the power exceeded 10 mW, ensuring the measurements were performed within the linear regime. In addition, we extracted estimates of our measurement error from fitting results performed on spectra in the linear regime.

A 2,2-diphenyl-1-picrylhydrazyl (DPPH) standard was used to calibrate the applied magnetic field. We used a 1-mM $CuSO_4{\cdot}5H_2O$ solution as a spin concentration standard to extract a numerical estimate of χ_g; its ESR signal was measured at numerous temperatures from 4 K to 300 K. We placed the standard in the same configuration as the SWCNT sample

with approximately the same microwave cavity volume to minimize differences between the sample and reference.

Despite the soft-bake acid-purification procedure used to remove ferromagnetic catalyst particles (cobalt and nickel), it is evident from the large ferromagnetic resonance (FMR) background seen in ESR spectroscopy that they remain in the sample (Fig. 3.5). We performed both thermogravimetric analysis (TGA) and x-ray photoelectron spectroscopy (XPS) to determine the mass concentration of the metallic catalyst particles. Using XPS, we determined the ratio of the Co to Ni catalyst to be 0.9:1.0, which is very close to the values reported by Nikolaev et al. [25]. Subsequently, this ratio enables one to compute how much of the resulting oxidized mass produced by TGA (Fig. 3.3) is due to the catalytic metal. TGA was performed on a $\sim$6.2 mg sample of the acid-purified laser-oven SWCNTs from room temperature to 950°C using a 10°C/min. ramp rate in air. The resulting mass percentage of 7.8% (see Fig. 3.3) reflects the metallic oxide formed from the catalyst particles (nickel and cobalt) in the now-incinerated SWCNTs. The most probable oxide species that formed during burning in oxygen were NiO, CoO, and Co_3O_4. With this assumption, we calculated that the average catalyst mass percentage of the metallic oxides remaining after TGA was 74.7% (assuming a Ni to Co ratio of 1.0:0.9, as obtained via XPS). Using this information, we estimate that 5.8% of the total mass of the SWCNT sample is due to metallic catalysts. This non-negligible mass percentage explains why the ferromagnetic resonance (FMR) from the catalyst particles dominates the background of the ESR scans of SWCNTs, as seen in Fig. 3.5 (a).

We performed Raman spectroscopy at discrete excitation wavelengths (514 nm, 633 nm, and 785 nm) to obtain an idea of lattice disorder in the sample and to provide an estimate of the average nanotube diameter. We examined the D-band (around 1350 cm^{-1}) to G-band ($\sim$1590 cm^{-1}) peak ratio to qualitatively estimate how defective the nanotubes are. As

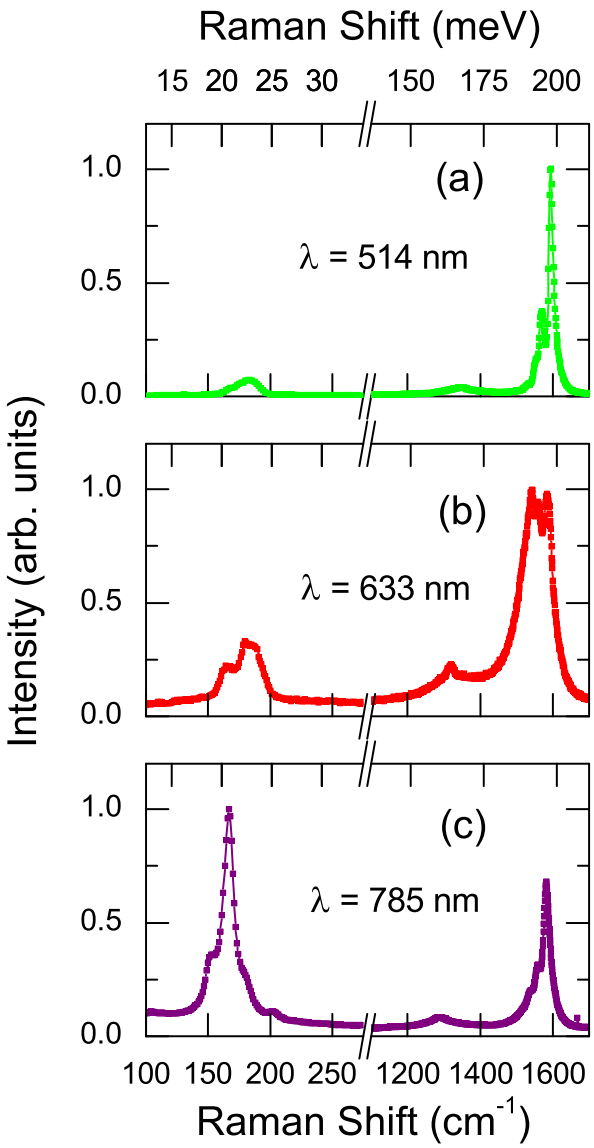

Figure 3.2 : Raman spectra from the SWCNT sample before ESR experiments using excitation laser wavelengths of (a) 514 nm, (b) 633 nm, and (c) 785 nm. The radial breathing mode peaks below 300 cm^{-1} suggest that the sample contains nanotubes with a diameter distribution centered on $\sim$1.36 nm. Figure adapted from [27].

Fig. 3.2 shows, the D-band to G-band peak ratio is not negligible, ranging from 0.075 at the 633 nm excitation wavelength to 0.039 at a 514 nm excitation. These numbers indicate that the SWCNTs that constitute the sample have some measure of lattice inhomogeneity. Further, using the radial breathing modes (RBMs) that occur in the region from 100 cm^{-1} to 250 cm^{-1}, one can utilize the $1/d_t$ dependence, where d_t is the SWCNT diameter, of the RBM frequency to extract SWCNT diameter estimates [69,70]. For our particular sample, we observed diameters from 1.2 nm to 1.6 nm with an average of $\sim$1.36 nm, which signifies that I have a distribution of semiconducting and metallic nanotubes roughly centered around the (10,10) armchair SWCNT species. Our average diameter estimation is very similar to the results obtained with more exacting methods on similarly prepared samples [71]. However, since we are using discrete Raman lines for the analysis, we are only able to provide a rough experimental approximation of the average SWCNT diameter.

3.1.1 ESR Curve Fitting

As seen in Figs. 3.5 and 3.6, the ESR signal is an irregular shape: it has a nearly linear background and an asymmetric ESR Lorentzian derivative lineshape. Starting with Feher and Kip [72] (experimental) and Dyson's [68] (theoretical) work in 1955, the so-called Dysonian shape has been recognized to be symptomatic of movement of the probed spins in and out of the rf skin depth of the sample, in analogy with Ramsey fringes [73]. Indeed, previous studies of the ESR on SWCNTs have observed Dysonian lineshapes [47,51]. For this work, we use a reduced form of the Dysonian given in Sitaram et al. [74]

$$\frac{d\chi}{dH_0} = \left(\frac{\cos\varphi}{\Delta H^2}\right)\frac{-2y+(1-y^2)\tan\varphi}{(1+y^2)^2}, \tag{3.1}$$

where $y = \frac{H_0-H_r}{\Delta H}$, ΔH is the half-width, and H_r is the resonance field. The weak form of Dysonian can be used here, because the conductivity and diffusion of the electrons in the

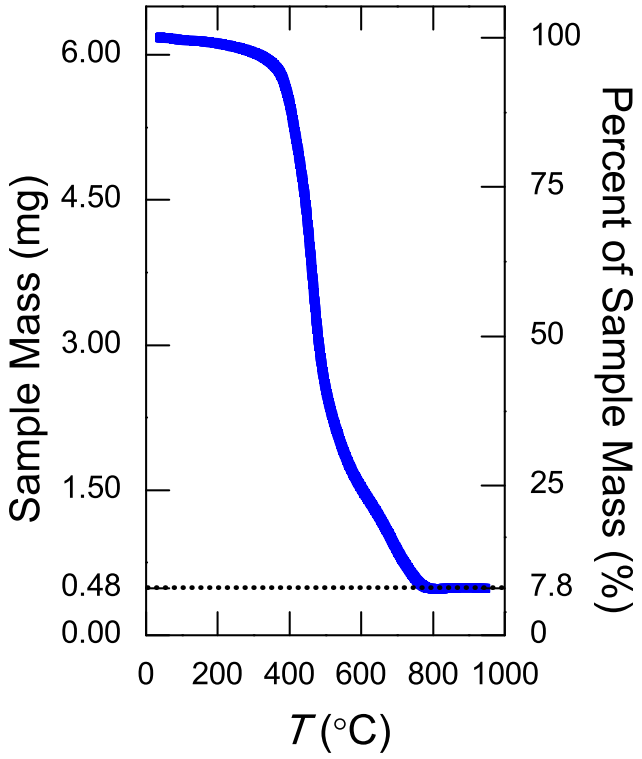

Figure 3.3 : TGA of the acid purified laser-oven powder SWCNTs used to create the sample. In combination with XPS results and assumptions about probable oxide formation, the final 7.8% sample mass percentage can be used to calculate the mass concentration of the catalyst particles. Figure adapted from [27].

SWCNT powder are both low as compared to a traditional metal. Nevertheless, unlike traditional magnetic resonance in insulating materials where the signal depends entirely on the imaginary part of the AC spin susceptibility, χ'', the Dysonian lineshape is also influenced by the real component, χ'. Taking the AC susceptibility, χ, to be

$$\chi = \chi'' \cos\varphi + \chi' \sin\varphi, \tag{3.2}$$

We define $\alpha \equiv \tan\varphi$, which is a dimensionless measure of the relative contribution of the real part (= 0 for the ESR of bound spins). To describe the FMR of the catalyst particles, Co and Ni, we use simple derivative Lorentzians. As Fig. 3.4 shows, the three curve de-

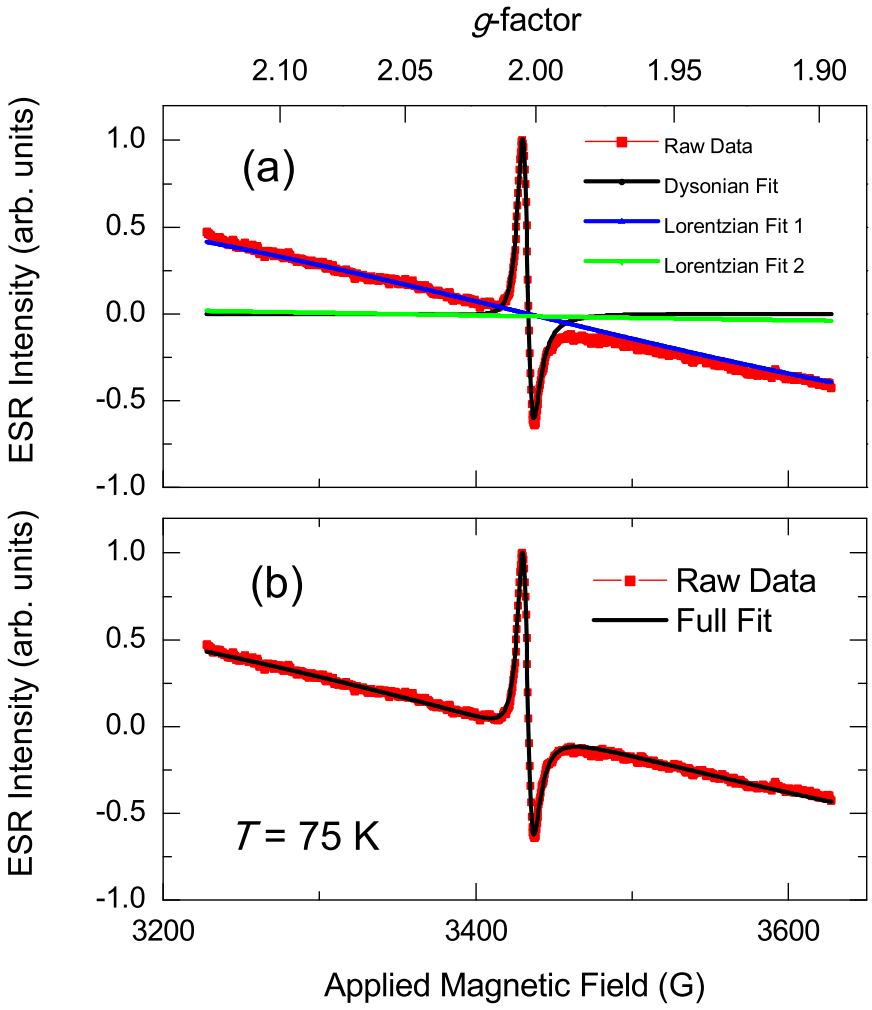

Figure 3.4 : (a) Raw ESR data at T = 75 K with decomposition of three curves used to fit data: Dysonian lineshape (black), Lorentzian 1 (blue), and Lorentzian 2 (green). (b) Raw ESR data with full fit (black curve). The full fit is a summation of curves used in (a). Figure adapted from [27].

composition accurately describes the observed lineshape. In some respect, there is a certain arbitrariness of the linewidth of the Co and Ni FMRs since we do not have a good idea of what they should be for this system, nor are we capturing the FMRs for the short scan data. However, for Fig. 3.4, good fitting is obtained when both Lorentzians have a linewidth above 1000 G, which agrees with the full scan data presented in Fig. 3.5. Each curve was fit using the patternsearch algorithm in Matlab utilizing limits on the values of the variables and a maximum evaluation run of 5.0×10^5. For each fit obtained, the R^2 value was above 0.93, although most curves had a R^2 of 0.95.

3.2 Experimental Results

Figure 3.5 shows the remarkable difference that occurs upon thermal annealing: the SWCNT ESR peak goes from being buried in the large catalyst FMR background to dominating the spectrum. Despite the tremendous increase in the SWCNT ESR signal, the FMR hardly changes, demonstrating that the annealing *only* affects the nanotube ESR. For the long scans, we are able to capture nearly the full FMR of the catalyst particles. As Fig. 3.5 shows, the fitting using two Lorentzian derivatives (FMR of catalyst particles) and a Dysonian (SWCNT ESR) very nicely captures the total ESR behavior of the sample.

A more detailed set of scans covering two orders of magnitude in temperature, which are shown in Fig. 3.6, allow a more quantitative understanding of the SWCNT ESR. The raw data traces presented in Fig. 3.6 are fit with a Dysonian lineshape (black traces) for each different temperature. The baseline, which becomes more prominent at higher temperatures, is simultaneously fit using two large linewidth Lorentzians to account for the slowly varying FMR background. The lack of secondary peaks and anomalous shapes, as is seen in other publications [45,49,53], attests to the purity of our sample. If MWCNTs [75], amorphous carbon [76], or graphite [77] contributed to the ESR signal, they would each

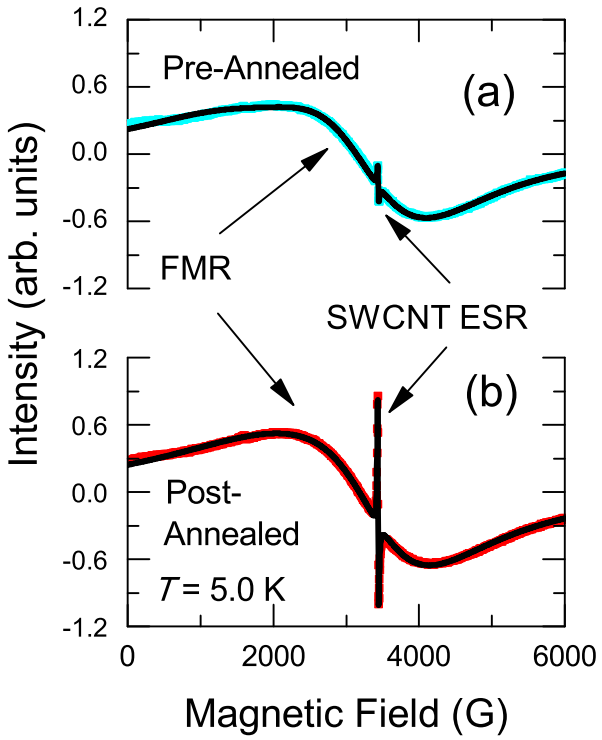

Figure 3.5 : (a) Full range ESR scan at 5.0 K of SWCNT sample before annealing (cyan), where the ESR signal is buried in the large FMR background. (b) Full scan of SWCNT sample at 5.0 K after annealing (red), where the SWCNT ESR is the dominant feature. Black curves indicate fits composed of two large linewidth Lorentzian lines, which describe the FMR background, and a Dysonian line describing the SWCNT ESR. The FMR intensities stay the same before and after annealing. Figure adapted from [27].

manifest themselves differently in lineshape and as a function of temperature. Therefore, we conclude that we are observing a spin resonance from SWCNTs. Figure 3.6 shows that for both sample conditions, the SWCNT ESR increases as T decreases. Since the signal intensity is proportional to the mass spin susceptibility, χ_g, the ESR signal change as a function of T strongly suggests that we are not observing Pauli law behavior, in which χ_g is independent of T. Further, as seen in both Figs. 3.5 and 3.6, the ESR signal size changes dramatically upon annealing.

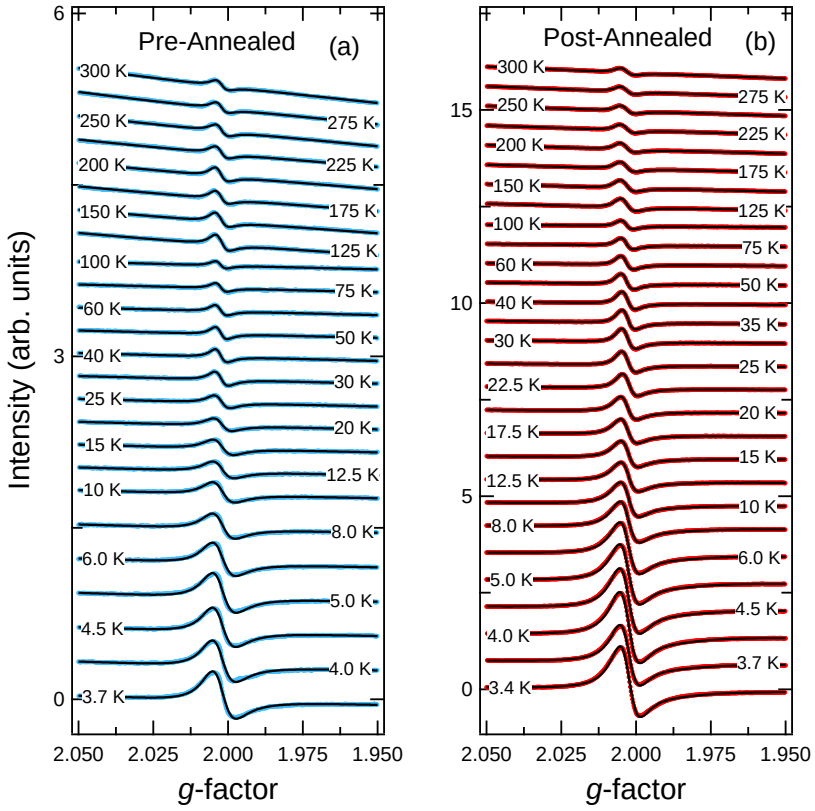

Figure 3.6 : Raw ESR scans of sample (a) before (cyan curves) and (b) after (red curves) annealing as a function of T. Black lines indicate fits to the traces. Figure adapted from [27].

3.2.1 Spin Susceptibility

A net magnetization, M, is created in a material when a static magnetic field, H_0, is applied to a substance. Typically, one defines the spin susceptibility, χ_s, to be: $\chi_s = \partial M/\partial H|_{H_0} \cong M/H_0$. Often, experimentalists approximate χ_s to be the proportionality between the magnetization and the applied field, such that $M = \chi_s H_0$. In the following, we present the some of the physics behind spin susceptibility, taking the case of Pauli susceptibility as an example. In the initial approach to this project, we hoped to observe a Pauli-law spin susceptibility, which would indicate that we were probing metallic SWCNTs. How-

ever, as we will see later on, we have clear evidence for Curie-law spin susceptibility, which strongly suggests that our probed spin species is finite-leveled.

Derivation of Pauli Spin Susceptibility

When a magnetic field, H_0, is applied to a metal at absolute zero temperature, the concentration of the spins parallel to the field, N_+, are changed:

$$N_+ = \frac{1}{2}\int_{-\mu H_0}^{\varepsilon_F} d\varepsilon D(\varepsilon + \mu H_0), \tag{3.3}$$

where ε is energy, $D(\varepsilon)$ is the density of electron states at a given energy, and μ is the magnetic moment of a species, which can be taken to be μ_B (Bohr magneton) in almost all cases. Approximating Eq. (3.3) gives

$$N_+ \cong \frac{1}{2}\left\{\int_0^{\varepsilon_F} d\varepsilon D(\varepsilon) + \mu H_0 D(\varepsilon_F)\right\}, \tag{3.4}$$

where the shift of N_+ downwards is $\approx \frac{1}{2}\mu H_0 D(\varepsilon_F)$. This change in the density of states in a magnetic field also occurs for spins anti-parallel to the field, except that the shift in N_- is opposite that of N_+, as shown in Fig. 3.7. Because of the upward shift for N_-, the density of electron states for the anti-parallel case is $D(\varepsilon - \mu H_0)$ where the integral is taken from μH_0 to ε_F:

$$N_- \cong \frac{1}{2}\left\{\int_0^{\varepsilon_F} d\varepsilon D(\varepsilon) - \mu H_0 D(\varepsilon_F)\right\}. \tag{3.5}$$

The net magnetization for any material, which is an experimentally observable quantity, is defined as:

$$M = \mu(N_+ - N_-). \tag{3.6}$$

Typically, the net magnetization and spin populations (N_+ and N_-) are normalized by the volume of the system, V, which corresponds with the usual form of M [78]

$$M = \frac{1}{V}\sum_i^N \mu_i, \tag{3.7}$$

where μ_i is the i^{th} magnetic dipole and the sum is taken over all N dipoles in a given volume, V. Putting Eqs. (3.4) and (3.5) into Eq. (3.6) gives

$$M = \mu_B^2 D(\varepsilon_F) H_0, \tag{3.8}$$

which can be further reduced into spin susceptibility by writing

$$\chi_s^{Pauli} = \mu_B^2 D(\varepsilon_F), \tag{3.9}$$

where $\chi_s \cong M/H_0$. When normalized by mass and presented in cgs, χ_s becomes χ_g (mass spin susceptibility) and has units of emu/g; otherwise, it is typically given as emu or emu/cm^3 if one is talking about volume spin susceptibility.

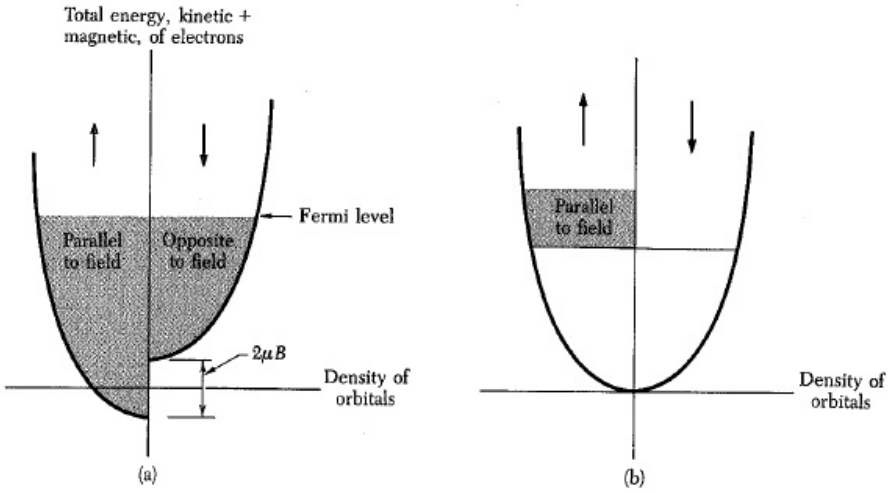

Figure 3.7 : The density of states shifts when a magnetic field is applied [79]. In (a), the lowest parallel spin states are energetically shifted downward to an energy μB below the zero field case, while the anti-parallel states move energetically upward by μB. Because the number of parallel and anti-parallel spins are different as seen in (b), there is a net magnetization of the sample.

A few things are important to note about the spin susceptibility of metals. First, Eq. (3.9) indicates that χ_s^{Pauli} exhibits no temperature dependence. This is a crucial distinction with

the Curie-law, which is described by:

$$\chi_s^{Curie} = C/T, \tag{3.10}$$

where C is the Curie constant and is equivalent to $\frac{\mu_B^2 N}{k_B}$, μ_B is the Bohr magneton, N is the number of probed spins, and k_B is the Boltzmann constant. Hence, one major, but not definitive, test to see whether electrons are localized or free is to perform temperature dependent ESR.

Second, the magnitude of χ_s^{Pauli} is affected by dimensionality through $D(\varepsilon)$. What Eq. (3.9) fails to do is to take into account electron-electron interactions, which are highly dimensionally dependent. Even in the 3D case, this is a substantial correction to even the simplest alkali metals [80].

In addition to not accounting for strong correlations, the issue of dimensionality is also important. A simple examination of the 1D case when $E \propto k^2$ (parabolic dispersion), for instance, will find strongly peaked values of $D(\varepsilon)$ as a function of ε, since $D(\varepsilon) \propto \varepsilon^{-1/2}$. If $D(\varepsilon_F)$ is on (or near) one of those peaks (also known as van Hove singularities), χ_s^{Pauli} could easily be much larger than when $D(\varepsilon_F)$ is far away from a van Hove singularity. This dependence on the magnitude of $D(\varepsilon_F)$ can actually be seen in Fig. 3.8. In that figure, the transition metals, such as Ti and V, have the highest susceptibilities due to their large density of orbitals. As Kittel points out, this is in agreement with heat capacity measurements [79].

The magnitude of χ_s^{Pauli} is small as compared to χ_s^{Curie}, with $\frac{\chi_s^{Pauli}}{\chi_s^{Curie}}$ sometimes on the order of 10^{-2} [80]. If the temperature dependence of χ_s^{Curie} is considered, one can begin to see the origin of the differences in magnitude by plugging in $\frac{\mu_B^2 N}{k_B}$ for C into Eq. (3.10) and

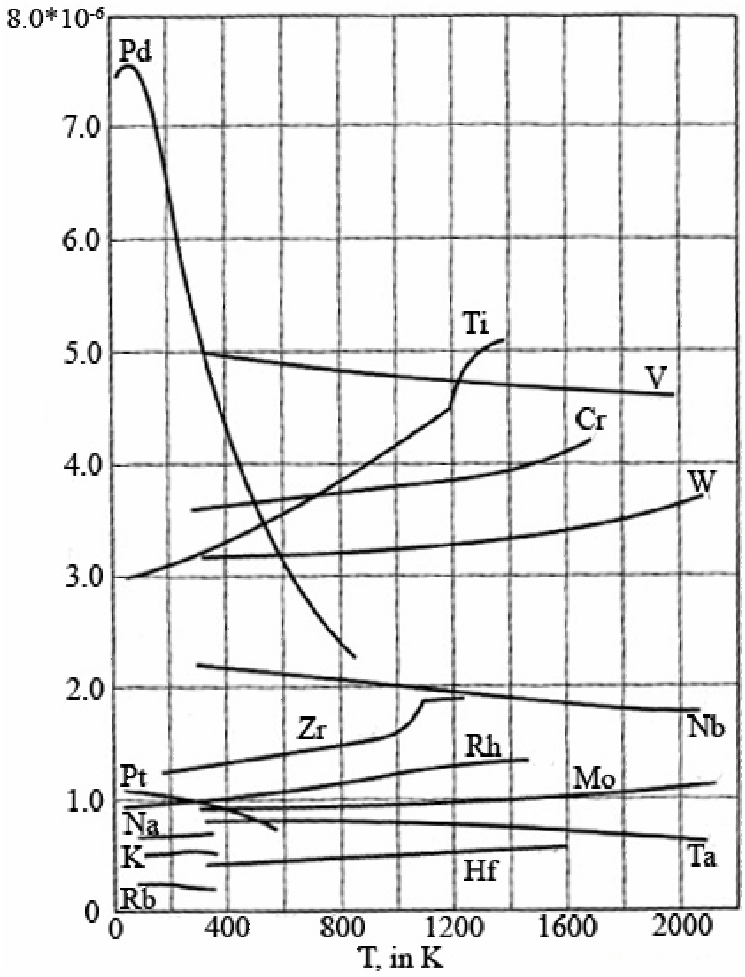

Figure 3.8 : Spin susceptibilities (in cm^3/g) of several metals as a function of temperature [79]. Several of the *d*-metals, such as Pd, Ti, and Zr, have some mild temperature dependence to them, though clearly not a Curie law ($\propto 1/T$) behavior. The more spherical the outer orbit, such as those seen in K and Na, the less temperature dependent χ is.

converting to Eq. (3.9) by multiplying by T/T_F:

$$\begin{aligned} \chi_s^{Pauli} &= \frac{N\mu^2}{3k_BT} \times \frac{T}{T_F} \\ &= \frac{N\mu^2}{3k_BT_F} \\ &= \mu_B^2 D(\varepsilon_F), \qquad (3.11) \\ \text{where} D(\varepsilon_F) &= \frac{Np^2}{3k_BT_F} \end{aligned}$$

where $p \approx 1$ for a metal and T_F can be related to the Fermi energy, $\varepsilon_F = k_B T_F$. Essentially, Eq. (3.12) says that only the electrons within $k_B T$ of the Fermi energy ($k_B T_F$) can contribute to the spin susceptibility in metals [79]. Thus, even though the Pauli spin susceptibility can be described in a similar manner as the Curie law, the inability for spins far away from the Fermi level to align with the applied field prevents metals from becoming strongly magnetized. In contrast, with Curie-law behavior, it is only thermal energy that causes spins to become unaligned, which explains why at very high temperatures, $\chi_s^{Curie} \to 0$. Put another way, the Pauli exclusion prevents total spin alignment with the applied field far better than thermal disordering does [80]; this effect is sometimes called Pauli-blocking.

Spin Susceptibility Results

To examine the change in the curve amplitude more quantitatively, we extracted χ_g from the fitted spectra in Fig. 3.6. We used a $CuSO_4 \cdot 5H_2O$ spin concentration standard measured at temperatures between 4 K and 300 K to obtain mass spin susceptibility values from the measurements. Figure 3.9 shows how χ_g varies as a function of T for both sample conditions. The large increase in χ_g between the pre-annealed and post-annealed sample conditions is striking, especially at low temperatures. Clearly, the annealing process greatly augments the number of spins probed.

Plotting χ_g versus $1/T$ shows that for both the pre and post-annealed sample conditions, the spin susceptibility follows a Curie-law behavior [Eq. (3.10)]. For the pre-annealed sample condition, we fit the values of χ_g from 300 K to 3.7 K using Eq. (3.1) and find that $C = 2.88 \pm 0.21 \times 10^{-8}$ emu-K/g, which translates into 7.9×10^{12} spins. This value for the pre-annealed Curie constant is very close to what Likodimos *et al.* found in their work [51], as well as what other groups have estimated their mass susceptibility to be [49, 50]. Similarly, if we fit the post-annealed data from 300 K to 4.0 K, we extract $C = 1.11 \pm 0.04 \times 10^{-7}$ emu-

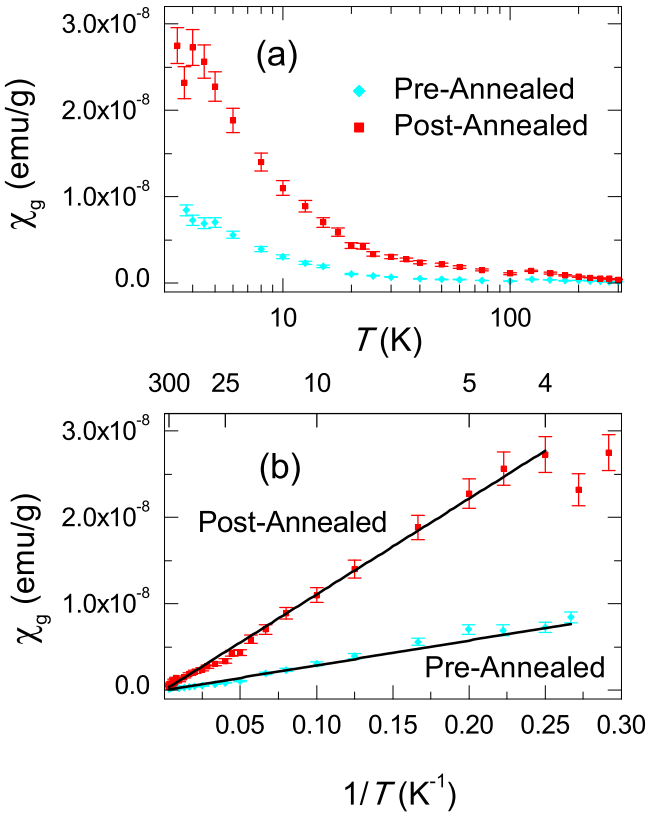

Figure 3.9 : (a) Mass spin susceptibility χ_g as a function of T for the sample before annealing (cyan) and after annealing (red). (b) χ_g versus $1/T$ for the sample before annealing (cyan) and after annealing (red). Annealing produces a large increase in the magnitude of χ_g, but does not change its temperature dependence. Both sets of data can be fit well using a Curie law model (black lines) down to ∼4 K. Figure adapted from [27].

K/g (3.0×10^{13} spins). Therefore, by removing adsorbed gases from the SWCNTs, the number of spins probed is increased by a factor of 3.9. Interestingly, both pre-annealed and post-annealed sample conditions show Curie-law trends down to ∼4 K. However, as the temperature drops below 4 K, χ_g seems to deviate from Eq. (3.10), especially for the post-annealed sample; further investigation is needed to determine how χ_g varies with T at temperatures below 4 K.

3.2.2 Oxygen Exposure Test

As discussed in the previous section, we showed that the ESR signal from SWCNTs could be increased when the sample was annealed at 115°C. This rather low thermal energy suggested that we look for physisorbed species from air that could alter ESR. Since N_2 is diamagnetic, it is a very weak candidate for causing this effect. O_2, on the other hand, has a paramagnetic triplet state, in addition to being known to strongly affect ESR in a variety of systems. As such, we tried to reverse the ESR increase from the thermal annealing using 99.99% pure O_2 to see if this hypothesis was indeed correct.

To investigate how physisorbed molecular oxygen gas species might contribute to the marked rise in the spin susceptibility, we performed an ESR measurement before and after we applied a constant pressure of pure oxygen onto a freshly annealed powdered SWCNT sample. We prepared the SWCNT sample by annealing it for 13.5 hours at 250°C under a 75 sccm flow of pure argon. The ESR tube was then sealed to prevent exposure to air. Next, we ran four ESR scans using 1.00 mW of microwave power using a 1.0 G modulation amplitude at 100 kHz, while staying at room temperature (T = 297 K). If one takes time zero to be when the sample was exposed to oxygen, the four scans done before exposure were performed at -84 minutes, -81 minutes, -67 minutes, and -22 minutes.

The oxygen exposure was accomplished by connecting a bottle of molecular oxygen gas to a simple hose to flow into the now opened ESR tube. We flowed gas for 3 minutes taking care not to mechanically disturb the sample. Next, we ran five ESR scans using the exact same conditions as were used before the O_2 exposure. An ESR scan was done roughly every 30 minutes: 3, 37, 66, 93, and 126 minutes. For each scan, the sample was exposed to atmospheric air; there was no further application of pure O_2.

As Fig. 3.11 shows, the ESR signal does not broaden upon exposure to oxygen. Instead, as oxygen diffuses through the SWCNT sample, the ESR signal becomes smaller. The

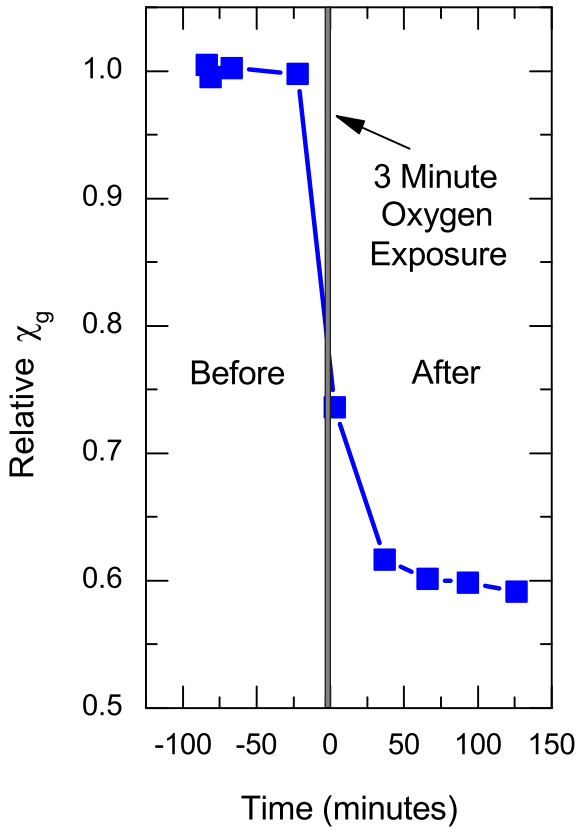

Figure 3.10 : Relative spin susceptibility of an annealed SWCNT sample over several hours shows a sudden decrease once oxygen is introduced (gray shaded region). After nearly two hours, the decrease in spin susceptibility appears to stop, indicating that equilibrium has been reached. Figure adapted from [27].

curves shown depict what we saw just before oxygen flowed onto the sample (black trace), just after (red), and two hours after (green). In addition to the ESR intensity reduction, the baseline seems be slightly changed.

Figure 3.10 shows, the relative spin susceptibility dramatically decreases as the oxygen is adsorbed onto the SWCNTs, dropping to 59% of the initial annealed spin susceptibility. As a comparison, the ratio of the pre-annealed spin susceptibility to the post-annealed spin susceptibility at T = 300 K is 0.42. The fact that the presence of oxygen does not fully

return the ESR to its original suppressed value may be due to the inability of the oxygen to return to its former locations between SWCNTs. Once the oxygen is removed, the strong van der Waals forces between tubes reduce the intertube spacing, thus preventing oxygen from quenching the ESR. This test unequivocally shows that oxygen is a strong spin suppressor in SWCNTs. Importantly, Fig. 3.10 demonstrates that the annealing effect is *reversible*: one can remove molecular oxygen and increase χ_g, and then add molecular oxygen back to the system and suppress χ_g.

3.2.3 Motional Narrowing

In addition to the ESR signal size decreasing as T increases, the half-width at half-maximum of the line, ΔH, becomes smaller as T is raised, as seen in Fig. 3.6. This phenomenon is known as motional narrowing [66, 67]: it occurs because the dephasing time of the spins changes as their translational energy is altered. At high T, the spins move rapidly, allowing for less time around dephasing centers, thus reducing the interaction between the probed spins and the dephasing centers. This decreased interaction gives a longer spin dephasing time (T_2), which in turn narrows the line. Conversely, at low T, the spins are moving more slowly, which broadens the line. Interestingly, we observe that this behavior occurs for both the annealed and non-annealed sample conditions.

One can see the phenomenon of motional narrowing more clearly in Fig. 3.12. The exponential decrease in ΔH is well described by combining Anderson's motional narrowing relation with a hopping wavefunction to model the spin movement [26, 27, 81–84]:

$$\Delta H = \Delta H_0 + \frac{A}{\Delta E \times \left[1 + \coth\left(\frac{\Delta E}{2k_B T}\right)\right]} \tag{3.12}$$

where ΔH_0 is the high-T ("metallic") limit of the linewidth, A is a temperature-independent variable, and ΔE is the energy required to move from one location to another. For the pre-

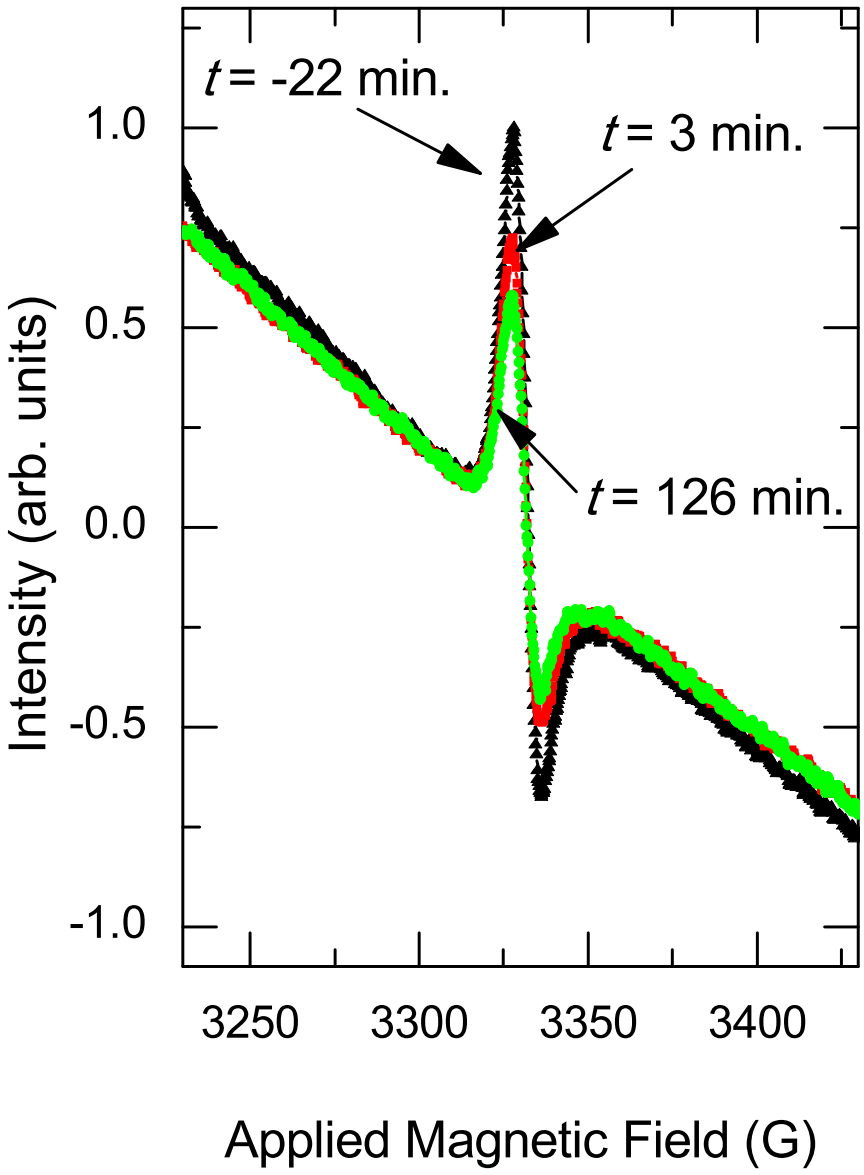

Figure 3.11 : Raw ESR traces of SWCNT ensemble at different times relative to when the sample is first exposed to oxygen: 22 minutes before (black trace), 3 minutes after (red trace), and 126 minutes (green trace). The drop in ESR intensity becomes larger as time from first exposure grows. However, as indicated in Fig. 3.10, the relative spin susceptibility levels off after about one hour. Figure adapted from [27].

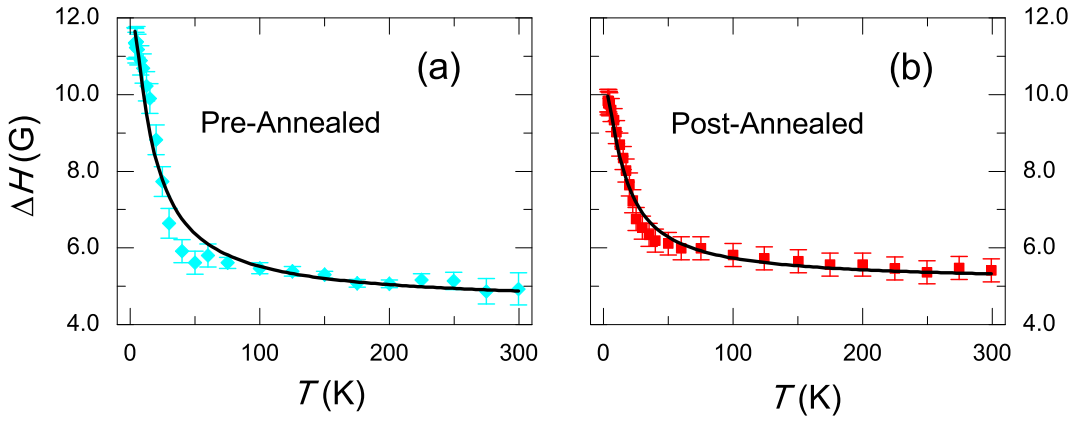

Figure 3.12 : ESR linewidth versus T for the (a) pre-annealed and (b) post-annealed sample conditions. The black lines indicate the fitting of Eq. (3.12) to the data [27].

annealed sample condition, we extract a ΔH_0 of 4.53±0.10 G ($T_2 = \frac{\hbar}{g\mu_B}\frac{1}{\Delta H} = 12.5$ ns) with a hopping energy of 1.26±0.16 meV (T_{hop} = 14.6 K) and $A = 18.3 \pm 1.9$ meV-G. Similarly, we fit the linewidth temperature dependence for the post-anneal sample condition to obtain $A = 11.6 \pm 0.8$ meV-G and $\Delta H_0 = 5.10 \pm 0.08$ G, with the latter quantity giving a T_2 spin dephasing time of 11.1 ns. The activation energy for the post-annealed sample condition, ΔE, is 1.18±0.09 meV (13.7 K).

Quantitatively, the annealing procedure seems to have only a minor effect on the hopping energy, changing T_{hop} from 14.6 K to 13.7 K. This small change in the hopping characteristics suggests that adsorbed gases have little effect on the motion of the spins. In a similar manner, annealing has a small effect on the linewidth in the high-T limit, ΔH_0. Annealing increases ΔH_0 by ∼0.5 G, which correspondingly changes the spin dephasing rate, T_2, from 12.5 ns to 11.1 ns, a relatively small drop. As with the hopping energy, the fact that annealing has only a minor effect on ΔH_0 indicates that adsorbed gases in bulk SWCNT systems have little impact on the mobility of the probed spins.

The fitting of Eq. (3.12) to the linewidth fundamentally captures the narrowing behav-

ior of ΔH as a function of T. As previously mentioned, Eq. (3.12) was derived from a hopping motion wavefunction, which was used to describe motional narrowing in doped semiconductors. Indeed, researchers investigated a similar linewidth behavior in P-doped Si [85, 86] and Ge [83, 84] as we observe in SWCNTs. In these doped semiconductor systems, the concentration of the ESR-active defects determines the lineshape form and its temperature dependence [86, 87]. At low to intermediate donor densities, motional narrowing is expected in these systems because the donor center-to-center distance is smaller than the spatial extent of the spin wavefunction.

Other models, such as those used to examine the linewidth in 1D conducting polymers [88, 89], may also be good fits, but there, a fundamentally different spin behavior would be assumed. More knowledge about spin diffusion in SWCNTs and how defect concentration changes temperature-dependent ESR is needed to more completely determine the SWCNT linewidth temperature dependence.

3.2.4 The α Parameter

To gain deeper insight into the spin hopping mechanism, we examined the asymmetry Dysonian lineshape parameter, α, which is proportional to the conductance of the probed spins [see Eq. (3.2)]. In particular, we were interested to see if α followed a VRH behavior at low T, which is mathematically given as [21, 24]

$$\alpha = \alpha_0 \times \exp\left[-\left(\frac{T_0}{T}\right)^{\frac{1}{1+d}}\right], \tag{3.13}$$

where T_0 is the characteristic temperature and d is the dimensionality of the system. As Fig. 3.13 shows, $\ln(\alpha)$ follows a linear trend with $T^{-\frac{1}{4}}$, indicating that the spins probed by ESR are undergoing phonon-assisted hopping in 3D from 3.4 to 20 K. We find from our fit that T_0 is 17.9$\pm$5.5 K and that α_0 is 1.20. The asymptotic limit of the α parameter, α_0,

approaches 1 as $T \to 0$. This trend is expected, since the asymmetry of the ESR signal is caused by thermally-activated hopping: as the phonon density decreases, so does the asymmetry of the Dysonian. The localization length, ξ, of the electronic wavefunction can be found from T_0 [24]

$$\xi = \left[\frac{18.1}{k_B T_0 D(E_F)}\right]^{1/3}, \tag{3.14}$$

where $D(E_F)$ is the density of states around the Fermi energy, E_F. One can estimate $D(E_F)$ by treating the defect density of states as having an energy separation that can be roughly estimated by ΔE. Thus, $D(E_F) \approx \frac{N(E_F)}{\Delta E} \sim 10^{19}$ states/cm^3-eV, where we utilize the spin density extracted from the Curie constant, $N(E_F) = 1.14 \times 10^{16}$ spins/cm^3. From Eq. (3.14), we estimate ξ to be $\sim$100 nm, similar to previous measurements of defect-induced localization lengths in SWCNTs [90]. The spacing of defects, R_d, can be estimated by $\left(\frac{4\pi}{3}N\right)^{-1/3}$, or $\sim$28 nm. A d = 3 VRH behavior is expected in this wavefunction-overlap regime ($R_d < \xi$) [21]. In addition, in this regime, exchange effects may also be important, but defect concentration dependence is needed to investigate this avenue more fully.

It is important to note that given the difficulty in extracting α, the $T^{-1/4}$ trend that we are observing can be considered robust. We also performed traditional conductance measurements on a similarly prepared sample (see Chapter 2), and although the conductance clearly showed 3D VRH behavior, we believe that our ESR and four-point probe conductivity measurements are probing different species, since the hopping parameters do not agree and the high-T trends are different. In addition, conductivity is probing all conductive electrons in the system, while α is obtained only from the ESR-active conductive species. Further investigation is necessary to fully establish this fact.

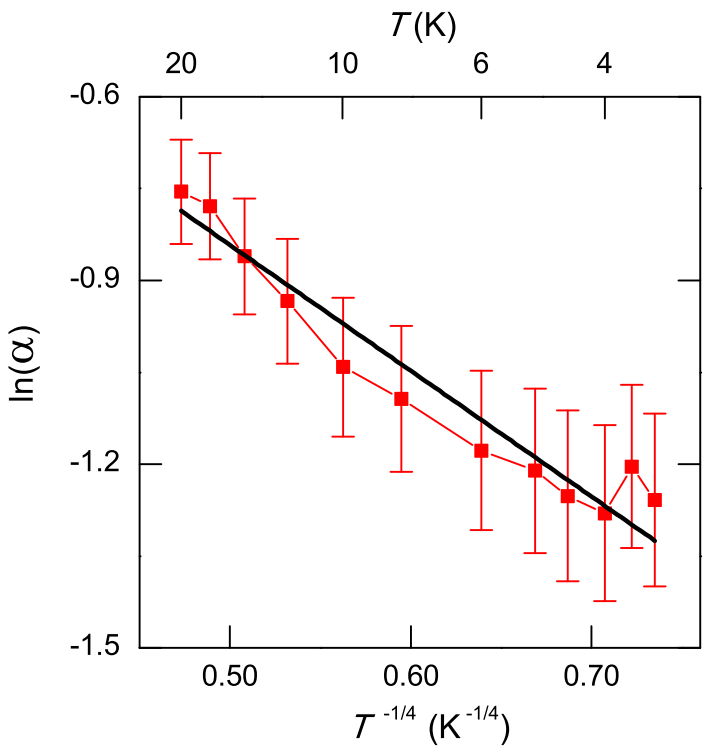

Figure 3.13 : The natural log of α versus $T^{-1/4}$ for $T \leq 20$ K. Figure adapted from [26].

3.2.5 g-factor

As mentioned above, the mobility of the spins is marginally influenced by the presence of adsorbed gases; rather, it seems to be strongly dependent on the sample temperature, as seen in Fig. 3.12. The center position of the resonance, H_0, on the other hand, is only slightly dependent on the temperature (Fig. 3.14). As is typical in magnetic resonance experiments, we define the g-factor as the ratio of the perturbing field energy to the magnetic dipole energy $g \equiv \frac{h\nu_0}{\mu_B H_0}$, where h is Planck's constant and ν_0 is the frequency of the perturbing microwave field. The measured g-factor for the pre-annealed sample condition is nearly temperature independent, staying close to the free electron g-factor value of 2.0023 throughout the full 3.7 K to 300 K temperature range. This behavior is similar to

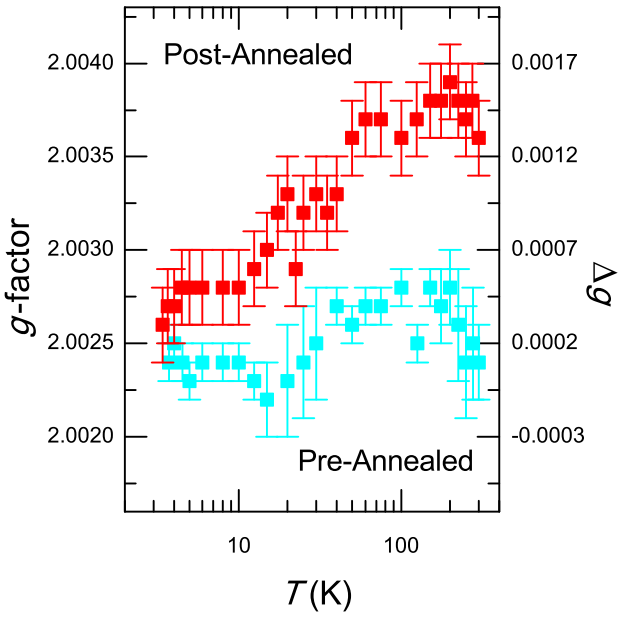

Figure 3.14 : Experimentally obtained g-factor values as a function of T for the sample before (cyan) and after (red) annealing. Figure adapted from [27].

the temperature dependence of the g-factor of graphite in the plane perpendicular to the c-axis [77, 91]. The g-factor of the post-annealed sample condition shows a slight increase with increasing temperature. However, there is a small, but measurable, change in the g-factor upon annealing, especially at high temperatures. If we take g_0 to be the free electron g-factor (2.0023), we can define the quantity $\Delta g \equiv g - g_0$. Following Platzman [92], we interpret Δg to be proportional to the spin-orbit coupling. As such, the upward shift (Δg changes by $\sim$0.001 at T = 300 K) in the g-factor upon annealing indicates that adsorbed gas species weakly quench some of the spin-orbit coupling of the probed spins.

3.2.6 ESR from Nanotube Defects

As Fig. 3.10 shows, the quenching of the spin susceptibility is reversible when molecular oxygen is introduced. Given this information, as well as the fact that we are using a low

annealing temperature of 115°C (33 meV) to create the changes in χ_g, it seems most likely that the spin susceptibility change is caused by physisorbed molecular oxygen: that is, no change in the chemical bonds of the system occurs when oxygen is either added or removed. Indeed, this line of reasoning follows Ulbricht *et al.*, who showed that molecular oxygen primarily physisorbs to SWCNTs [93] (unlike reactive atomic oxygen, which is known to form epoxies and ethers in SWCNTs [94]). In addition, theoretical work has also shown that molecular oxygen should physisorb to SWCNTs [95–97].

Taken as a whole, our results show that molecular oxygen physisorbed onto SWCNTs affects only χ_g, with minimal changes to ΔH and the g-factor. The lack of change in ΔH is especially odd, since in many biological systems, O_2 serves as a general relaxor for various paramagnetic species via spin-spin interaction, which leads to ESR line broadening. This very nature finds wide application of oxygen in membrane topology studies of membrane bound macromolecules [98, 99] and serves as the theoretical basis for oximetry in quantifying O_2 in a particular biological sample present in an aqueous environment [100]. Furthermore, the observation that oxygen does not affect the observed ΔH in SWCNTs also contrasts with previous ESR studies on gas adsorption in 1D polymer systems, such as *trans*-polyacetylene, which show that ΔH increases as the number of gas molecules (pressure) increases. For example, Houzé and Nechtschein [101] show that exchange and dipolar interactions resulting from an adsorbed gas species broaden the ESR linewidth, $\Delta\omega$, with the relation given as $\delta(\Delta\omega) = p\omega_{\text{hop}}C_i$. Here p is the probability of a spin flip due to an interaction, ω_{hop} is the hopping frequency of the probed spin species, and C_i is the concentration of the adsorbed gas. If this type of process was occurring in this system, we should see some change in ΔH $\left(\Delta H = \frac{\hbar\Delta\omega}{g\mu_B}\right)$ when the oxygen is desorbed (annealing) or adsorbed (oxygen exposure test); however, no significant change in ΔH is observed.

A very fast relaxation process (such as dipolar broadening due to the triplet state of

oxygen) could exist in this system. Presumably, this latent ESR signal would show up as a change in the baseline, assuming that the resonance width was on the order of 100 to 1000 G. However, this "spin segregation" into two different relaxation processes seems unlikely, especially since the baseline changes only slightly when the system is exposed to oxygen (see Fig. 3.10). However, given the magnetic field scan range of the spectrometer and signal-to-noise limits, measuring a signal with such a wide linewidth is difficult. Experiments in the time-domain may be necessary to fully support our hypothesis that a very fast relaxing spin from the SWCNTs does not exist.

A more plausible hypothesis is that oxygen is passivating the paramagnetic moments of SWCNT defects. These defects could be caused during SWCNT growth, processing, or even acid purification [25]. As shown in the discrete Raman spectroscopy plot in Fig. 3.2, the SWCNT sample has a measurable amount of lattice defects, so an ESR signal from say, topological defects or dangling bonds is possible. Despite the localized nature of the ESR active species, the unpaired electrons still have mobility in this scenario: the Dysonian signal in this work does not come from electrons in the conduction band, as with ESR from bulk metals, but from thermally-activated finite-level species. In addition, if we were probing defects or dangling bonds, one would expect both a Curie-law spin susceptibility temperature dependence, as well as a *g*-factor that is close to the free electron value; we observe both behaviors in our system. Additionally, ESR arising from non-pristine SWCNTs would explain why the tremendous variation in ESR signals exists in the literature: in essence, different SWCNT purification methods and sample preparation steps would create differing resonance signals.

We can quantify how prevalent these ESR-active defects are by using the extracted estimate for the Curie-coefficient of the post-annealed sample ($1.11 \pm 0.04 \times 10^{-7}$ emu-K/g). If one assume that all of the SWCNTs in the sample are (10,10) nanotubes, one finds that there

is roughly one probed spin for every 3×10^5 carbon atoms. Though this number in itself may not establish that the ESR signal arises from non-pristine SWCNTs, it does suggest an exceedingly weak response (assuming a SWCNT length of 1 μm, $C = 3.60\times10^{-25}$ emu-K/SWCNT).

The quenching of the signal from oxygen exposure may result from a compensation mechanism. If, for example, the defects are responsible for the ESR signal are *n*-type, creating states closer to the conduction band edge within the band gap, then they can be compensated by the introduction of acceptors. Oxygen is thought to be a *p*-type acceptor to SWCNT, especially in the presence of defects [102, 103]. If the oxygen molecule is in the spin-singlet state, even charge transfer (chemisorption) can occur [102–104]. The adsorption of oxygen molecules to the ESR active defects would suppress the ESR signal; subtracting weakly-bound oxygen from the system would reverse this quench. A parametric study of ESR as a function of oxygen pressure is needed to further clarify our observations, including the exact nature of the defects.

3.2.7 Power-Dependent ESR

For several temperatures between 3 K and 300 K, we performed a microwave-power scan to assess how the ESR signal saturates. The advantage of a so-called power scan has two main advantages: first, one can determine the linear power regime (similar to the sweeps of I_{source} that we discussed in Chapter 2), and second, one can extract the spin-lattice relaxation time, T_1. Unfortunately, the down side of a power scan is that one is adding increasingly more energy to the system, which causes it to heat up (in the same manner as the THz radiation heated the quantum well sample in Chapter 4). Therefore, one must be very careful about what is causing saturation of the system: namely, is it due to the lack of states in the excited level, or an increase in the overall temperature of the lattice (ESR SWCNT signal $\propto 1/T$).

Using the same ESR spectrometer described earlier, we ran microwave power-dependent ESR scans from 6 μW to 200 mW for $T \leq 100$ K and from 200 μW to 200 mW for $T > 100$ K. We performed power scans on both the pre-annealed and post-annealed sample conditions at numerous discrete temperatures: 4 (only for the post-annealed sample), 5, 10, 15, 20 (T = 25 K for the pre-annealed sample), 35 (only for the post-annealed sample), 50, 100, 150, 200, 250, and 300 K. We began each scan at the highest power and decreased it by a factor of two until the lowest power was reached. For each power scan, the ESR spectrometer parameters were kept the same, so as to insure that relative spin susceptibility could be extracted.

Figure 3.15 shows a power scan for the post-annealed sample at T = 4.0 K. As the microwave power is increased, the observed un-normalized ESR amplitude also increases up until 25 mW. Above 25 mW, the ESR signal begins to decrease, reflecting sample heating or level saturation or both. At the highest microwave power (200 mW), the large decrease in the ESR signal size from the 25 mW level is mostly due to lattice heating: we would expect that level saturation would show either a leveling of the amplitude or a small decrease, not the very substantial drop we see in Fig. 3.15.

The asymmetry of the Dysonian lineshape significantly changes towards more a dispersive lineshape as power is increased. The asymmetry increase with microwave power is even more significant at higher lattice temperatures. A correct fitting of the power-dependent curves is necessary to say more. However, the observation that χ' becomes a more significant fraction of the ESR lineshape seems to agree with other saturation studies, which showed that the absorptive part of the spin susceptibility saturated while the dispersive part did not [105].

Figure 3.15 shows the raw ESR spectra, which only gives us a rough qualitative idea of how the ESR signal is changing with microwave power. Since the signal scales as

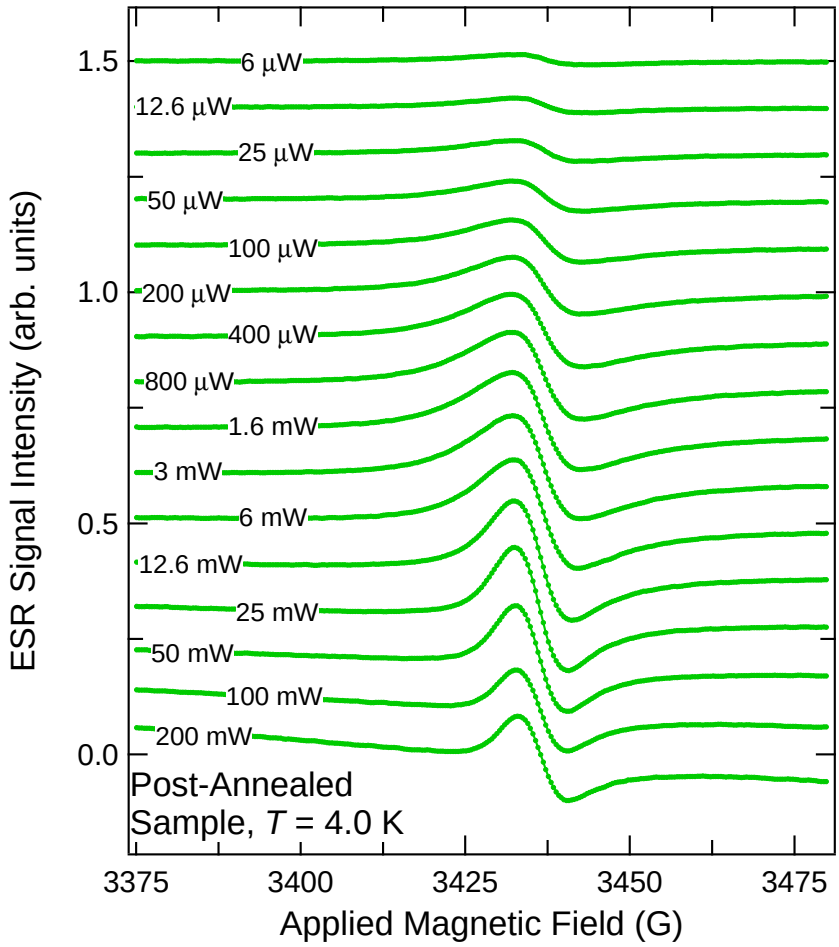

Figure 3.15 : Raw ESR traces for the post-annealed sample at T = 4.0 K for various microwave powers. The changing baseline indicates that the ferromagnetic FMR signal is increasing relative to the SWCNT ESR as microwave power is increased.

$\sqrt{P}$ [106], where P is the microwave power, we can normalize all of traces in Fig. 3.15 for a direct comparison. Figure 3.16 shows the results after normalizing for microwave power. As can be clearly seen, starting at 400 μW, a continuous decrease in the ESR signal size is observed as microwave power is increased. Interestingly, the linewidth does not broaden significantly as power is increased. In fact, at 200 mW, the ESR linewidth is narrower than at low powers.

To extract information from Figs. 3.15 and 3.16, one must consider the spin-lattice

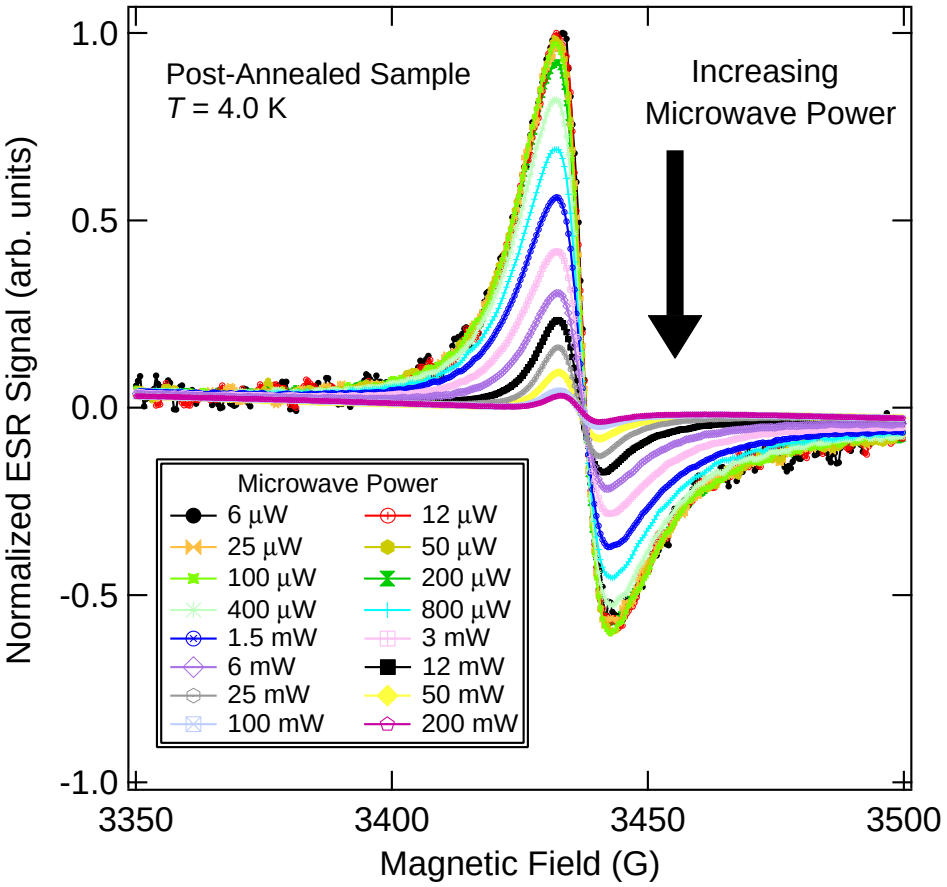

Figure 3.16 : Normalized ESR traces for the post-annealed sample at $T = 4.0$ K for various microwave powers. Deviations from the low power (linear) regime are seen beginning at 400 μW.

relaxation time, T_1, in addition to the dephasing time, T_2. Typically, the linewidth of an ESR trace, $\frac{\Delta\omega}{2}$ can be related to T_1 and T_2 using [78]

$$\frac{\Delta\omega}{2} = \frac{1}{T_2} + \frac{1}{2T_1}. \tag{3.15}$$

T_1 is usually much longer than T_2, which reduces Eq. (3.15) to: $\frac{\Delta\omega}{2} \simeq \frac{1}{T_2}$. (As a side note, in the case of metals, $T_1 = T_2$, so the spin-lattice time does affect the measured linewidth [107].) We made this approximation in Eq. (3.1) when we dropped T_1. In ac-

tuality, the imaginary part of the spin susceptibility is:

$$\chi'' = \frac{1}{2}\chi_0\omega_0 T_2 \left[\frac{1}{1+\gamma^2 T_2^2 (H-H_0)^2 + \gamma^2 H_1^2 T_1 T_2}\right], \tag{3.16}$$

where ω is the Zeeman angular frequency and $\gamma = \frac{g\mu_B}{\hbar}$ is the gyromagnetic ratio. The additional term with T_1 in it is often referred to as the "saturation term," and it will also show up in the equation for χ'. The signal that we obtain on the ESR spectrometer is proportional to $\frac{d\chi}{dH}$. The double integration of the ESR curve, therefore, will give a value that is proportional to $\frac{\pi\chi_0\omega_0}{\gamma\left(1+\gamma^2 H_1^2 T_1 T_2\right)^{1/2}}$. From the double integration value and the measurement of T_2 (from the linewidth), one should be able to extract T_1 from the power-dependent scan. This step will be done in the next few weeks, as the last part of the ESR project analysis.

3.3 Conclusions

In conclusion, we have clearly demonstrated that spin susceptibility in nanotubes is strongly influenced by the presence of physisorbed oxygen. We observe a nearly fourfold increase in spin susceptibility by desorbing gases present in our SWCNT ensemble. The presence of adsorbed gases is shown not to substantially affect the spin hopping energy, which we find to be $\sim$1.2 meV. We observe that the g-factor is very close to the free electron value for both the pre-annealed and post-annealed sample conditions. The decrease of the g-factor with decreasing temperature is not well-explained. Given the dependence on oxygen, the Curie-law spin susceptibility behavior, and the motional narrowing observation, we hypothesize that the spin suppression is due to compensation of donor-type defects by acceptor oxygen states [26, 27].

Further work still remains on this subject, namely, the fitting and analysis of the power-dependent ESR traces. Although we took power-dependent scans for both the pre-annealed and post-annealed sample conditions, the value of T_1 should not depend on the local en-

vironment of the spins. We expect, however, that the temperature dependence of T_1 will yield insights as to the spin-lattice relaxation mechanism. In addition, the change of α with microwave power may also be useful, since that curve should show when the χ'' begins to saturate (i.e. become a smaller fraction of the total lineshape as compared to χ').

The work presented here shows that ESR of bulk SWCNTs is dominated by the presence of defects. However, the original aim of this research was to investigate the spin dynamics of 1D metals using nanotubes. To achieve fundamental physical insight into the exotic nature of metallic 1D spin physics, we must accomplish three things: one, demonstrate that we have a 1D object; two, show bulk magnetization (a spin for every unit cell); and three, convincingly observe conduction electron spin resonance. To achieve these three steps, we propose to measure the spin resonance of a known arm-chair (metallic) nanotube over a trench, probed using DC conductivity.

Growing a nanotube from a chemical vapor deposition process (or something similar to it) ensures that the tube will be defect-free, fact we can confirm using μ-Raman measurements. This step is rather crucial given that carbonaceous defects have a strong spin susceptibility, as shown in this chapter. Using μ-Raman, μ-photoluminescence, and/or DC conductivity, we can determine whether or not our tube is metallic. Once the metallic-nature of the SWCNT is established, we will e-beam evaporate contacts onto the nanotube. Using DC conductivity, the ESR of the SWCNT can be detected by measuring the change in the resistance which occurs when spins absorb energy as the magnetic field sweeps through the Zeeman resonance. To improve the signal-to-noise ratio, we will modulate both the microwave perturbing field and the Zeeman splitting field at different frequencies and lock in to the difference frequency using a LIA. If a spin resonance can be seen, the hope is that measurements at high magnetic fields (above 10 T) and low thermal energies (below 10 K) will provide an extremely interesting and fertile phase space to investigate. We believe that

these series of steps will allow us to observe the ESR from metallic SWCNTs, paving the way for the direct observation of 1D metallic spin physics.

Chapter 4

Manipulation of Intra-Exciton Dynamics in Semiconductor Quantum Wells

4.1 Introduction

Dimensionally restricted semiconductors represent one of the most promising classes of materials for investigating optically excited electron-hole pair phenomena. Excitons, which are Coulombically bound electron-hole pairs with Bohr radii on the order of 10 nm, are formed in semiconductors if the binding energy is great enough to overcome thermal perturbations (see, e.g., Koch *et al.* [108]). Their simple electron-hole composition makes them behave like a hydrogen-like particles, as several experiments have demonstrated [109–116].

However, fundamentally, there are key differences between excitons and atoms. Despite the relatively high binding energies of 1D and 2D excitons, the intra-excitonic level energy spacings in low-dimensional structures are in the terahertz (THz) frequency regime (or meV energy range), as compared to atoms which have transitions in the visible spectrum. In addition, unlike atoms, excitons are a photon-created transient species, existing for only short durations (tens of picoseconds to nanoseconds) in a semiconductor. The similarities and differences between atoms and excitons, specifically with a focus on intra-excitonic dynamics, have been studied with increasing sophistication [117–121] with the advent of pulsed and tunable THz sources. Despite the heightened interest in excitonic phenomena, little experimental work [117, 119] on intra-excitonic *temporal* dynamics has been done.

In this chapter, we show that THz-created time-resolved photoluminescence (TRPL)

quenching in a quantum well produces a steep, but temporary, drop in emission from the 1s exciton energy with a concomitant rise in 2s excitonic emission. As the induced 2s emission vanishes over several hundred picoseconds, the PL from the 1s exciton state recovers and then becomes enhanced; the PL from the 1s state eventually returns to its unperturbed value after a few nanoseconds. We observed that the THz-induced 2s emission starts after the 1s quenching begins, and we show that this time lag depends on the strength of the THz electric field. These results are compared to a microscopic analysis of the system and are shown to agree. The control of PL using intense THz radiation demonstrates the ability to effectively "shelve" excitons into higher energy states for an extended time.

In addition to intra-excitonic scattering, we also study how the PL quenching depends on resonant and non-resonant tuning of the THz photon energy around the 1s-2p intra-excitonic transition. We show that as the pump-quench time delay is increased (i.e., the system becomes more excitonic), the fraction of excitons that are quenched becomes more significant. Furthermore, as the THz field strength is increased, the fraction of quenching excitons begins to saturate. Long THz wavelengths are shown to strongly suppress 1s emission regardless if the THz photon energy is resonant with the 1s-2p transition.

4.2 Background

4.2.1 Photoluminescence Quenching Induced by Far-Infrared Radiation

One method for studying intra-excitonic physics is THz-radiation-induced PL quenching. PL quenching has primarily been studied by resonantly exciting a bright, luminescing state to a dark one [114, 122, 123]; this energy-specific PL quenching is a sensitive method for studying low-energy resonances of free and bound carriers in solids, known as optically-detected resonance. Despite the utility of PL quenching spectroscopy, there exists a near-

absence of TRPL quenching studies. Indeed, the only infrared-radiation-induced TRPL quenching study that has been performed thus far examined resonant quenching via inter-subband transitions [124]. Temporal resolution is especially important for excitonic PL suppression, since there is an ambiguity as to the source of PL in semiconductors: it was theoretically shown [125], and then later experimentally observed [126–129], that 1s excitonic PL can occur even when the 1s exciton state is not yet populated. TRPL quenching, therefore, can be used not only to study PL suppression and recovery, but also to examine excitonic formation times and intra-excitonic temporal dynamics.

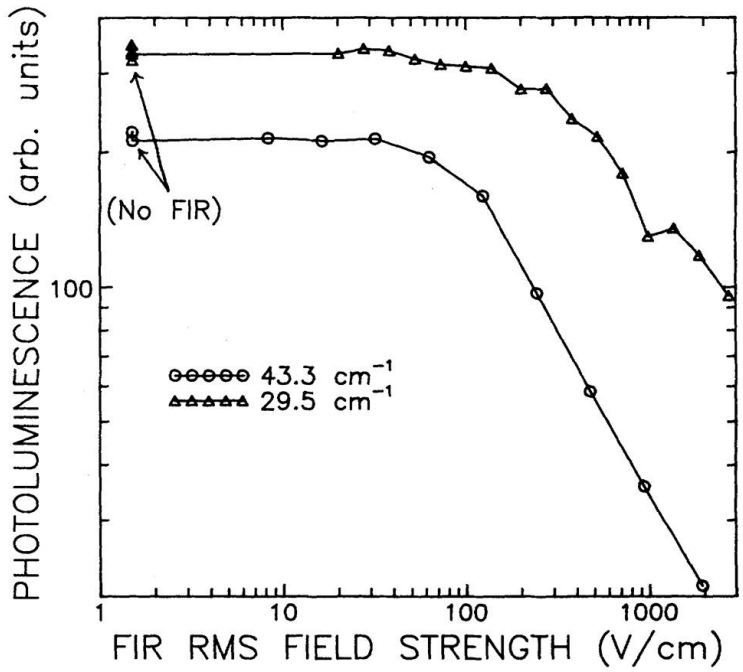

Figure 4.1 : PL intensity from optically excited $Al_{0.3}Ga_{0.7}As/GaAs$ quantum wells in the presence of far-infrared radiation. The intensity is plotted versus far-infrared field strength for 29.5 cm^{-1} (339 μm) and 43.3 cm^{-1} (231 μm). As the field strength of the far-infrared light is increased, the time-integrated PL intensity substantially decreases. Figure adapted from [130].

Previous investigations of far-infrared-radiation-induced PL quenching focused on how

the THz radiation field strength, E_{THz}, and wavelength, λ_{FEL}, altered the time-integrated PL spectrum. As Fig. 4.1 shows, the PL intensity substantially drops as the quenching radiation field strength increases. It was concluded in a follow-up paper [131] that the strong, non-resonant THz radiation heated free carriers (Drude-like absorption) which in turn heated/ionized excitons, thus quenching the PL and broadening the overall emission energy spectrum. This proposed multi-step quenching model relied on examining how the carrier temperature (extracted through the Boltzmann tail of the PL), T_C, scaled with the THz wavelength ($\propto \lambda_{\mathrm{FEL}}^2$) and field strength ($T_C^3 \propto E^2$). Later studies in this area were not able to achieve narrow-band THz, leading to ambiguous results, including the lack of PL conservation [132].

4.3 Experimental Methods

4.3.1 Experimental Layout

All of the experiments presented here in this chapter performed at the Helmhotz-Zentrum Rossendorf-Dresden, located outside Dresden, Germany. We used several free-electron laser (FEL) "shifts," each lasting 12 hours, to take TRPL measurements on a very well characterized set of quantum wells. By synchronizing the FEL pulses to the Ti:sapphire (Ti:Sa) excitation laser, the time delay between each pulse could be fixed, allowing for "pump-quench" spectroscopy to be performed.

Quantum Well Sample

The sample used in this experiment consisted of fifteen undoped quantum wells made up of 8-nm $In_{0.2}Ga_{0.8}As$ wells and 15-nm GaAs barriers grown by molecular beam epitaxy (provided by Dr. Glenn Solomon at NIST). Although a single quantum well could have been

used, the multiple quantum well (MQW) sample produced a larger signal. Magneto-optical absorption and PL measurements performed on this particular sample enabled us to know the $1s$ to $2p$ energetic splitting (10.6 meV or 117 μm) [133]. Due to strain in the sample, the light-hole exciton is well-separated from the heavy-hole exciton, which allows us to ignore valence-band complexities. We observed a PL emission at the $1s$ energy centered at 1.331 eV with linewidth of $\sim$7 meV. It should be noted here, that this linewidth is rather large compared to typical GaAs quantum wells. The addition of In into the GaAs structure creates alloy disorder and interface roughness in the lattice, which produces an inhomogeneous broadening of the PL linewidth. This effect has implications for how clearly we can separate the $1s$ and $2s$ emission behaviors.

Experimental Layout

A schematic of the experimental setup is given in Fig. 4.3. For all experimental results presented here, the lattice temperature of the sample was held at 5.0 K. A Ti:Sa laser with a 5 ps pulsewidth and a center wavelength of 850 nm (1.460 eV) was used to generate an electron-hole pair density of $\sim 1\times10^{11}$ pairs/cm^2 per quantum well. The pair density value is very close to the estimated Mott transition density, n_{C}, at which the exciton radii become comparable to the inter-excitonic spacing:

$$n_{\mathrm{C}}\pi a_{\mathrm{B}}^2 \sim 1 \tag{4.1}$$

for excitons in 2D. The $1s$ Bohr radius in our sample is $\sim$7 nm, giving an estimated $1s$ Mott density, n_{C}^{1s}, of $\sim 6\times10^{11}$ pairs/cm^2. However, this back-of-the-envelope calculation under estimates the Mott density by at least a factor of three. Therefore, n_{C}^{1s} is more correctly estimated downwards to be $\sim 1-2\times10^{11}$ pairs/cm^2. Moreover, the $2s$ Bohr radius is even larger, meaning that n_{C}^{2s} is $\approx 1-2\times10^{10}$ pairs/cm^2. These values of n_{C}^{X} strongly suggest

that excitonic behavior will be marginal at the pair densities used. However, since the THz radiation spot size is large (on the order of hundreds of microns) as compared to the Ti:Sa spot size (60 μm), one can expect that the THz field is nearly the same at all points of the Gaussian Ti:Sa spot. Further, at the edges of the Ti:Sa excitation area, the pair densities will be much lower. Therefore, we looked to see how densely pairs were created at the very periphery of the pump spot. At the excitation spot edge, where 5% of the total PL emanates, the pair densities were at $\sim 9 \times 10^9$ cm^2 per well.

The excitation photon energy was chosen so that it was above the 1s exciton center emission (1.331 eV), but below the band gap of GaAs (1.519 eV at 5.0 K), which ensured that electron-hole pairs were only created in the quantum wells. PL from impurity-bound excitons in GaAs complicates the spectra, as seen in Fig. 4.2. The excitation above the band gap of GaAs creates electron-hole pairs that are not in the InGaAs wells, which means that our pair density calculations become much more complicated. To avoid this source of confusion, the Ti:Sa was set at 1.460 eV.

The Ti:Sa laser had an incidence angle of 15° with respect to the growth direction of the MQWs with a measured spot size of 60 μm and a pulse energy of 380 pJ. To ensure consistency, the excitation laser was passed through a Glan-laser polarizer, such that the E-field was p-polarized for the entire experiment. The PL from the MQWs was collected in a back-scattered geometry and sent to a spectrometer attached to a streak camera. The streak camera had a measured temporal resolution, Δt_r, of 40 ps and a scan range of 2.1 ns. The temporal resolution of the streak camera, Δt_s, has three elements added in quadrature:

$$\Delta t_s = \left[(\Delta t_1)^2 + (\Delta t_2)^2 + (\Delta t_3)^2 \right]^{1/2}, \tag{4.2}$$

where Δt_1 is the time dispersion from the spatial spread (e.g., the grating of the monochromator), Δt_2 is the time dispersion caused by the spatial resolution and the deflector speed, and Δt_3 is the time dispersion caused by the deflection of the electric field. The observed

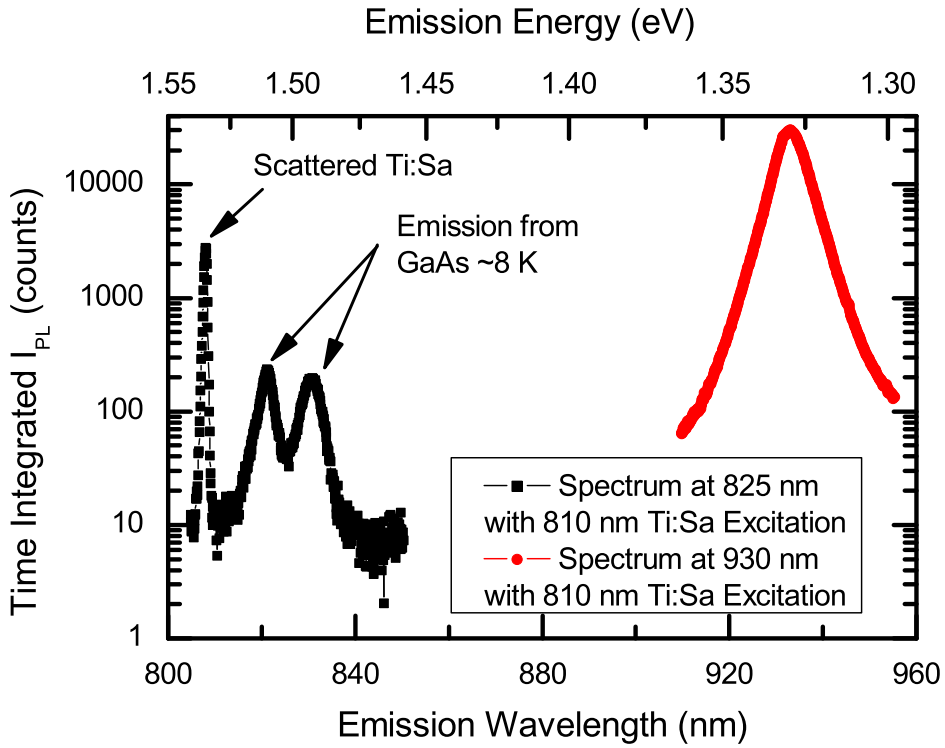

Figure 4.2 : Time-integrated emission spectrum for 810 nm Ti:Sa excitation. Two grating positions were used, so as to capture the high energy emission (black curve) and the low energy emission (red curve).

temporal resolution of a phenomenon, Δt_p, can be extracted as: $\Delta t_r = \left[(\Delta t_s)^2 + (\Delta t_p)^2\right]^{1/2}$. Since all of the elements of Eq. (4.2) are difficult to determine, the most straightforward way of determining Δt_r is to simply measure a streak camera image of a known pulsewidth (after severely attenuating the beam, so as not to damage the camera). The measurement of a 4.5 ps Ti:Sa beam with the exact experimental conditions used for the experiment is given in Fig. 4.4. As can be clearly seen, the 4.5 ps laser pulsewidth is severely broadened by the optics of the streak camera.

The sampling rate of the streak camera was roughly every 4 ps, and the energy resolution of the spectrometer attached to the streak camera was 130 μeV. The Ti:Sa repetition

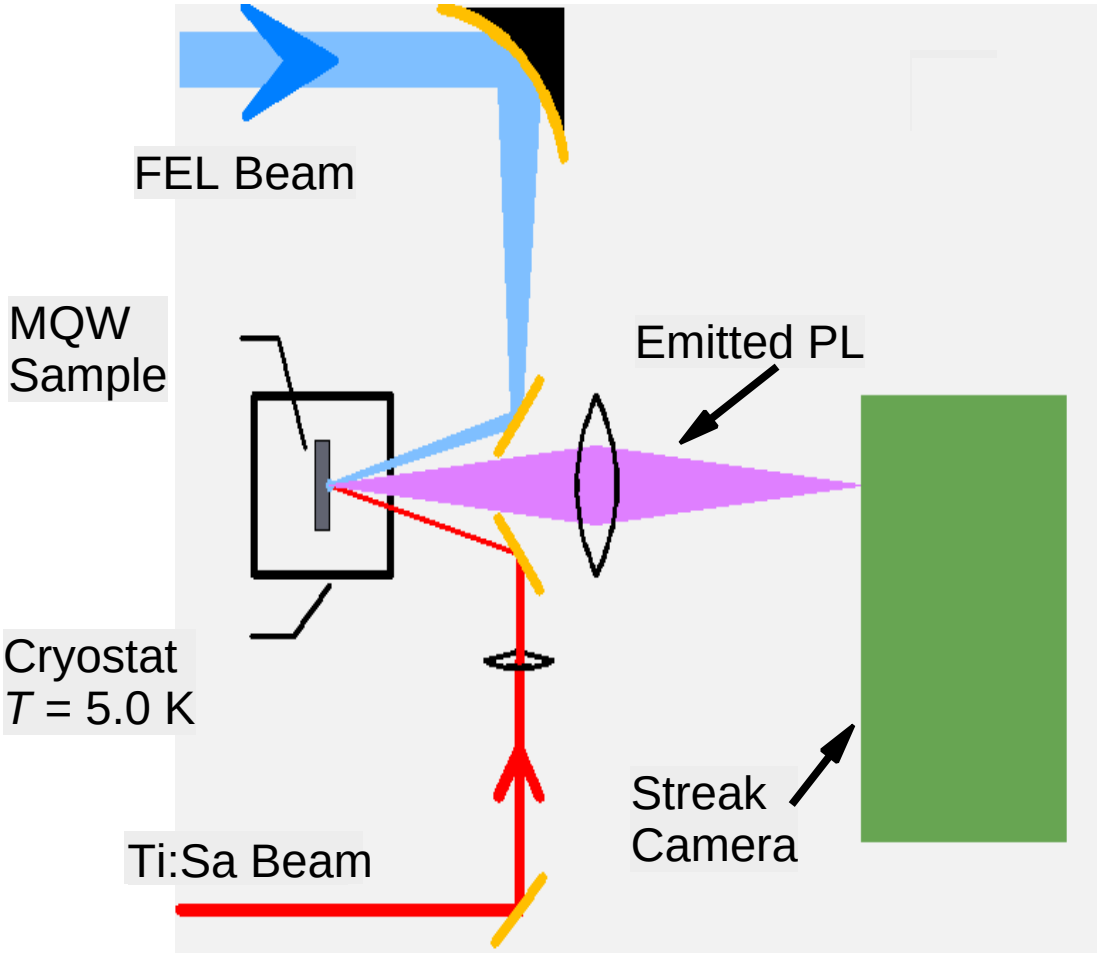

Figure 4.3 : Experimental setup for the collection of the TRPL data. Figure adapted from [134].

rate was electronically locked to the sixth harmonic of the FEL frequency so as to synchronize the two lasers. The Ti:Sa beam was passed through an acousto-optic modulator, which reduced the repetition rate from ∼78 MHz to 13 MHz, matching the repetition rate of the FEL. The temporal spacing between the Ti:Sa and FEL pulses was controlled using a mechanical delay line.

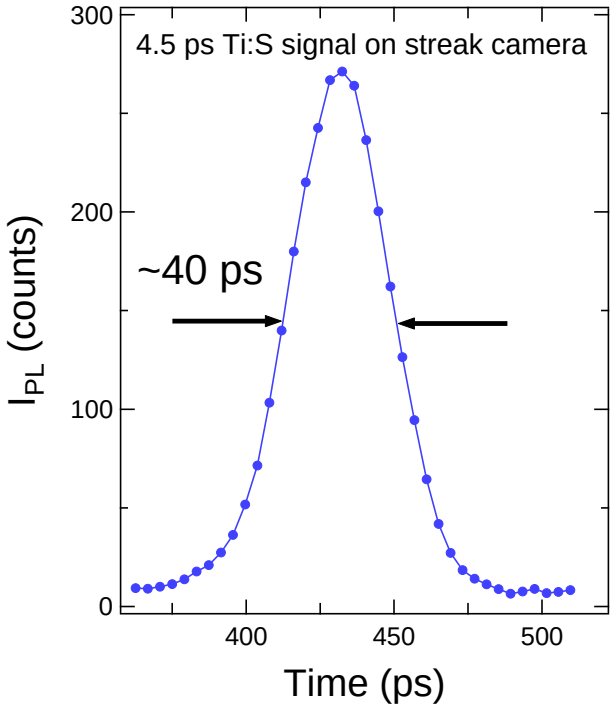

Figure 4.4 : Extracted pulsewidth from the streak camera of a 4.5 ps laser pulse.

4.3.2 Methodology

Four FEL wavelengths in the mid- and far-infrared regime were used: 32 μm (38.5 meV), 61 μm (20.2 meV), 118 μm (10.5 meV), and 200 μm (6.22 meV), corresponding to THz photon energies around the intra-excitonic 1s to 2p transition (117 μm or 10.6 meV). At each FEL wavelength, we measured the FEL spot size using a thermal camera at the sample position. THz photon energies and pulsewidths were estimated from spectrometer measurements, where we assumed a Fourier-transform limited pulse behavior for the latter quantity. Table 4.1 shows the measured FEL pulsewidth values for each wavelength used. For certain wavelength ranges, there is a substantial amount of difficulty in obtaining a stable FEL output. This fact is reflected in the $\lambda \approx 118$ μm values. As seen in the table, the pulsewidth for the 118.09 μm output (11.92 ps) differs from the 117.93 μm output (31.45 ps) by nearly

a factor of three. Ideally, the bandwidths day-to-day should be relatively close to one another, but due to the experience of the individual FEL operators and the stability of the equipment, wide fluctuations can be seen. Unfortunately, pulsewidth values significantly impact the physics of our experiment, since the peak electric field, E_p, depends on the pulsewidth, τ_p:

$$\begin{aligned} I_p &= \frac{P}{R_p A \tau_p} \\ E_p &= \left(\frac{2 I_p 377\Omega}{n}\right)^{1/2}, \end{aligned} \tag{4.3}$$

where I_p is the peak intensity, P is the average power, A is the spot size area, R_p is the repetition rate, 377 Ω is the impedance of free space, and n is the index of refraction. The issue of exactly how strong the transmitted THz field is will be discussed later on in this chapter. However, the $\lambda = 118.09$ μm (11.92 ps) FEL output was only used for the pump-quench time delay study at constant power; for all other results, the $\lambda = 117.93$ μm output was used for the "118 μm" case.

For each FEL wavelength, both time-integrated and time-resolved PL were collected. The time-integrated PL was collected with and without the presence of the FEL to test whether or not the PL intensity was conserved. Furthermore, the time-integrated PL was much more sensitive to changes in the emission spectral weight, since the emission energy was not partitioned across time. Therefore, the time-integrated PL served as more delicate probe of the FEL-induced spectral changes.

At four pump-quench time delays, we obtained TRPL as a function of FEL field strength. Roughly speaking, the four delays were: 40 ps, 140 ps, 350 ps, and 730 ps. These times were chosen to see how the formation of excitons affects the $1s$ emission quenching. It was tentatively expected that as the system changed from an electron-hole plasma (times very close the Ti:Sa excitation) to an excitonic one (later pump-quench times), we would see a larger, more prominent quenching effect. Slow exciton formation dynamics were first ob-

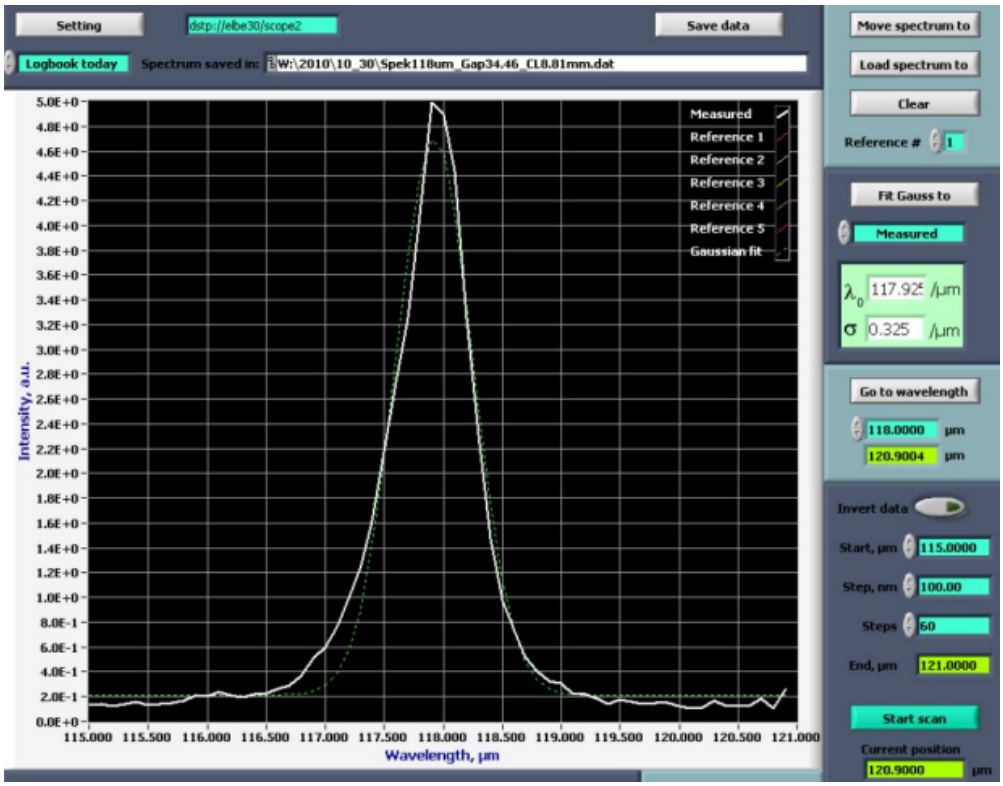

Figure 4.5 : Screen shot from the spectrometer showing the measured FEL bandwidth at 118 μm.

served by Kaindl *et al.* [117], who showed that for above resonant optical pumping, exciton formation took hundreds of picoseconds to complete (see Fig. 4.6). Therefore, we believed that at low pump-quench delay times, not only would the electron-hole plasma screen more of the far-infrared pulse, but there would also be luminescence electron-hole recombination at high momentum values.

In addition, we performed a sweep of the pump-quench time delay at a constant FEL power for all the wavelengths but 32 μm. By keeping the sweep at a constant power, we could investigate how the formation time affected the response of the system to the THz field. Because we were not performing multiple FEL powers, many more time points could be collected (eleven time positions), as compared to the systematic power dependence (four

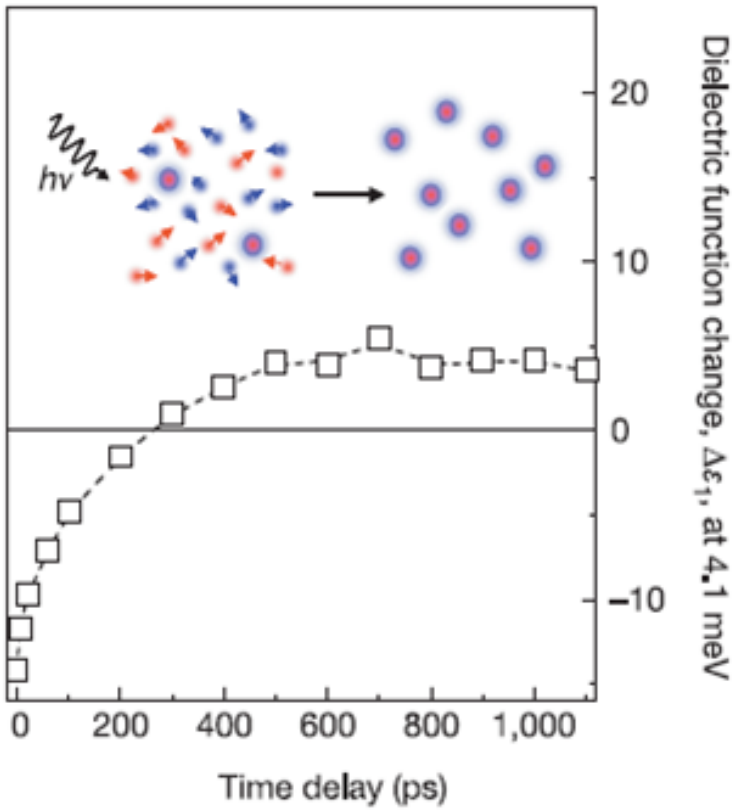

Figure 4.6 : Dielectric function change, $\Delta\varepsilon_1$ as a function of pump-probe delay time at an energy of 4.1 meV (300 μm, 1 THz). Figure adapted from [117].

power levels).

4.4 Results

4.4.1 Time-Integrated Photoluminescence

The first time-integrated PL experiment performed was a T-dependent study of the PL. As seen in Fig. 4.7, numerous temperatures were tested from 8 to 295 K. A clear trend in the PL emerges: as the temperature increases, the PL emission shifts to higher energies and the intensity becomes smaller. This behavior has been seen in numerous semiconductors, with

Table 4.1 : Measured FEL Parameters.

λ (μm)	**Bandwidth (μm)**	ν **(THz)**	**Photon Energy (eV)**	**Pulsewidth (ps)**
199.47	2.87	1.504	6.22	20.38
118.09	1.718	2.540	10.51	11.93
117.93	0.65	2.544	10.52	31.45
61.48	0.532	4.880	20.18	10.44
32.2	0.35	9.317	38.53	4.35

the temperature-dependence following a Varshni relation [135]:

$$E_g(T) = E_g(0) - \frac{\alpha T^2}{T+\beta}, \tag{4.4}$$

where $E_g(0)$ is the band gap at 0 K, α is constant, and β is a constant that is proportional to the Debye temperature. The band gap energy must be re-normalized for electron-phonon interactions, such that when T is above the Debye temperature, E_g goes linearly with T; when T is below the Debye temperature, E_g increases as T^2. Equation (4.4) also takes into account a smaller, yet still important contribution of the change in the lattice spacing due to the thermal expansion or contraction with T [136]

$$\left(\frac{\partial E_g}{\partial T}\right)_V = -3\alpha B \left(\frac{\partial E_g}{\partial p}\right)_T. \tag{4.5}$$

Here V is the volume, p is the pressure, α is the thermal expansion coefficient [different than the α given in Eq. (4.4)], and B is the bulk modulus. Thus, the change in the position of the lattice atoms has an effect on the band gap energy. We will use Fig. 4.7 to qualitatively explain how lattice heating from the THz radiation can cause overall PL suppression.

Specifically, for the cases when the THz wavelength is at 32 μm and 61 μm, we see a substantial red-shift in the PL emission, especially at high THz radiation intensities, that we attribute to lattice heating.

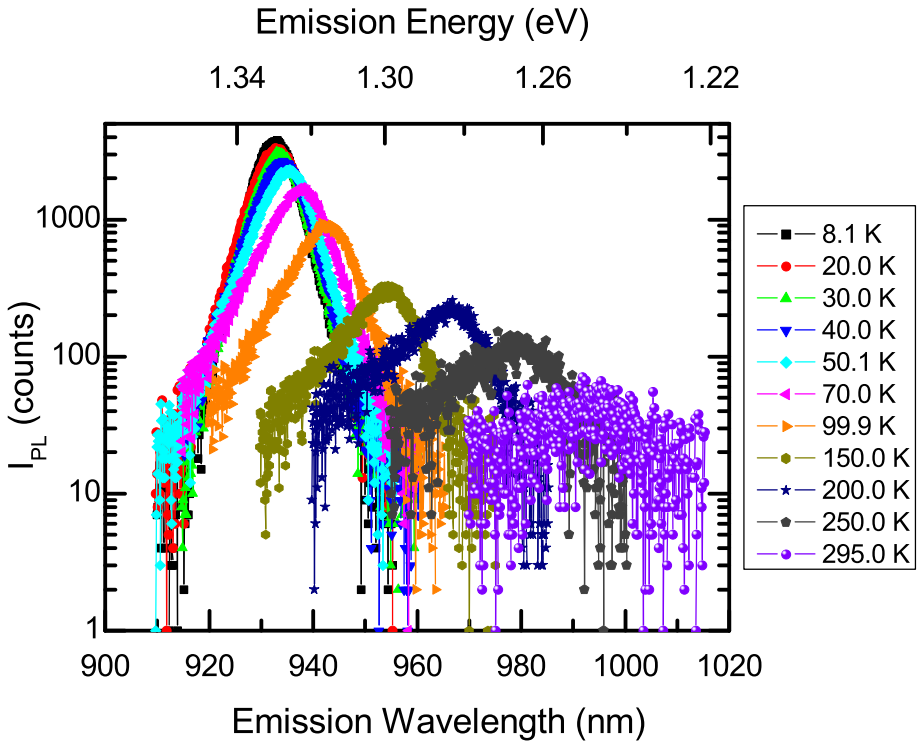

Figure 4.7 : Temperature dependence of time-integrated PL in the absence of THz radiation. As the lattice temperature of the quantum well increases, the PL intensity is reduced, and the center of the spectrum red-shifts. The movement of the spectra with temperature is well-described by the Varshni equation.

Figure 4.8 shows two examples of time-integrated PL taken during the experiment. Two types of time-integrated experiments were performed. The first is given in Fig. 4.8(a), which shows how the emission energy spectrum changes as a function of the pump-quench delay time. In this particular experiment, we are using a high field (measured power is 1.65 W or an estimated electric field of 4.7 kV/cm) that is resonant with the $1s$-$2p$ transition. At τ_{FEL} $\sim$14 ps, there is a clear heating of the carrier plasma, as indicated by the high

Boltzmann tail at energies above 1.34 eV. This PL tail quickly becomes minimized as the delay times are increased, as evidenced by the high-energy PL emission trend downwards in intensity towards the non-FEL trace. Interestingly, a shift in the peak position of the PL is not observed; if heating were occurring, we would see a change in the peak position, a fact that is clearly and explicitly demonstrated in Fig. 4.7.

The second time-integrated test that was performed was power-dependence. In Fig. 4.8(b), the effect of increasing the THz power is shown. A factor of ten increase in the FEL power (P_{FEL} = 610 mW or E_{FEL}= 3.7 kV/cm) at 61 μm significantly red-shifts and lowers the time-integrated PL, indicating that the lattice is being heated by the presence of the THz radiation. The high-energy Boltzmann tail is also elevated for the high power case, as compared to the emission spectrum without the THz radiation.

To get better insight into the effect of the THz radiation on the emission energy, we need to look at the differential response. Taking the intensity spectrum as a function of the emission energy, E, to be $I(E, P_{\mathrm{FEL}})$, we can define a differential emission, $\Delta I/I$ as:

$$\Delta I/I(E,P) = \left[I(E,P) - I(E,0)\right]/I(E,0), \tag{4.6}$$

where $\Delta I/I$ is defined for a given FEL power, P. Physically, $\Delta I/I$ is a measure of the THz-induced change in the luminescing species. Figure 4.9 shows $\Delta I/I$ for the curves presented in Fig. 4.8(a). The differential response shows a clear evolution of the positive enhancement of the high energy emission spectrum. In particular, if we look 10.5 meV above the center $1s$ emission energy, a noticeable positive "bump" exists for all time delays. Since the $2s$ and $2p$ states exist at this energy, we take this as tentative evidence that we are seeing THz-induced enhancement of the higher order excitonic states. However, since the $2p$ to vacuum state (positive parity) optical transition is forbidden due to parity conservation [137], we surmise that the THz-induced PL at this energy is from the $2s$ state.

PL emission above 10.5 meV is also seen in Fig. 4.9. At the lowest time delay (14 ps),

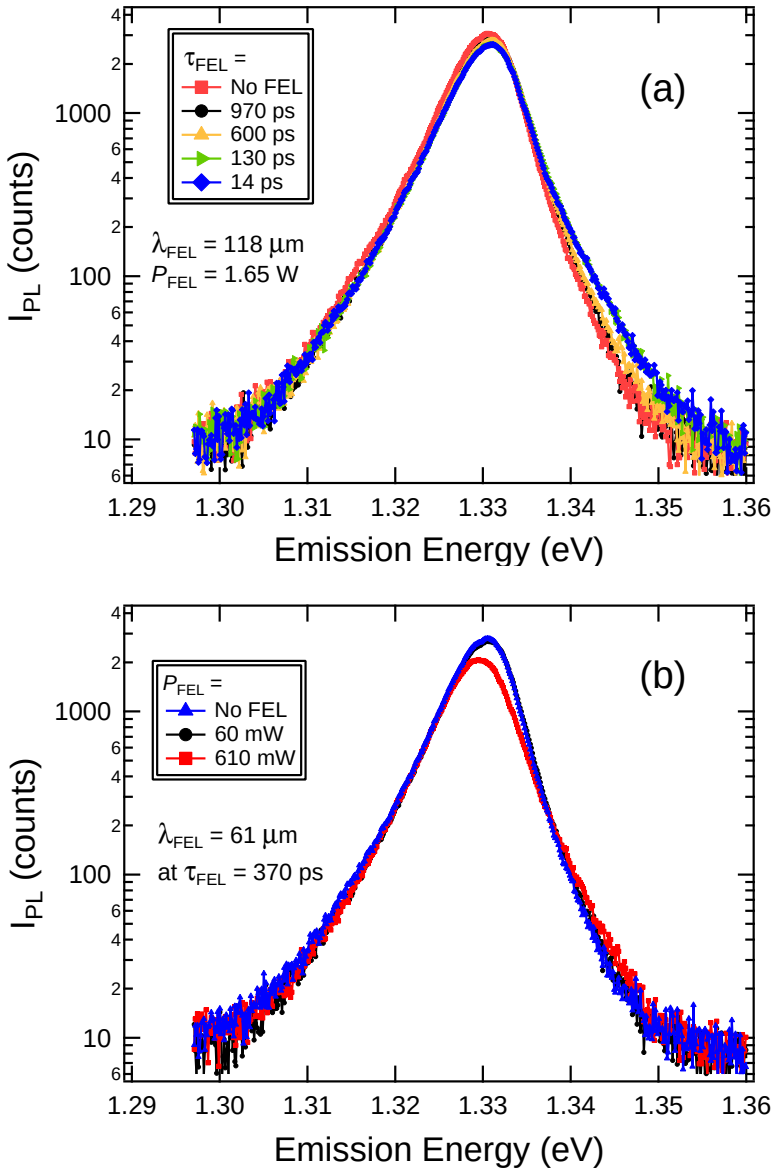

Figure 4.8 : (a) Time-integrated PL intensity versus emission energy as a function of various pump-quench time delays at $\lambda_{FEL} = 118$ μm and $E_{FEL} = 4.7$ kV/cm (1.65 W). The red curve indicates the emission profile without the presence of any THz. (b) Time-integrated PL intensity versus emission intensity for three THz field strengths at $\lambda_{FEL} = 61$ μm and $\tau_{FEL} = 370$ ps: no THz (blue diamonds, $P_{FEL} = 0$ mW), 1.2 kV/cm (black circles, $P_{FEL} = 60$ mW), and 3.7 kV/cm (red squares, $P_{FEL} = 610$ mW). A significant suppression of the total PL intensity, as well as a shift of the peak position to lower emission energies is seen when the THz power is increased from 60 mW to 610 mW.

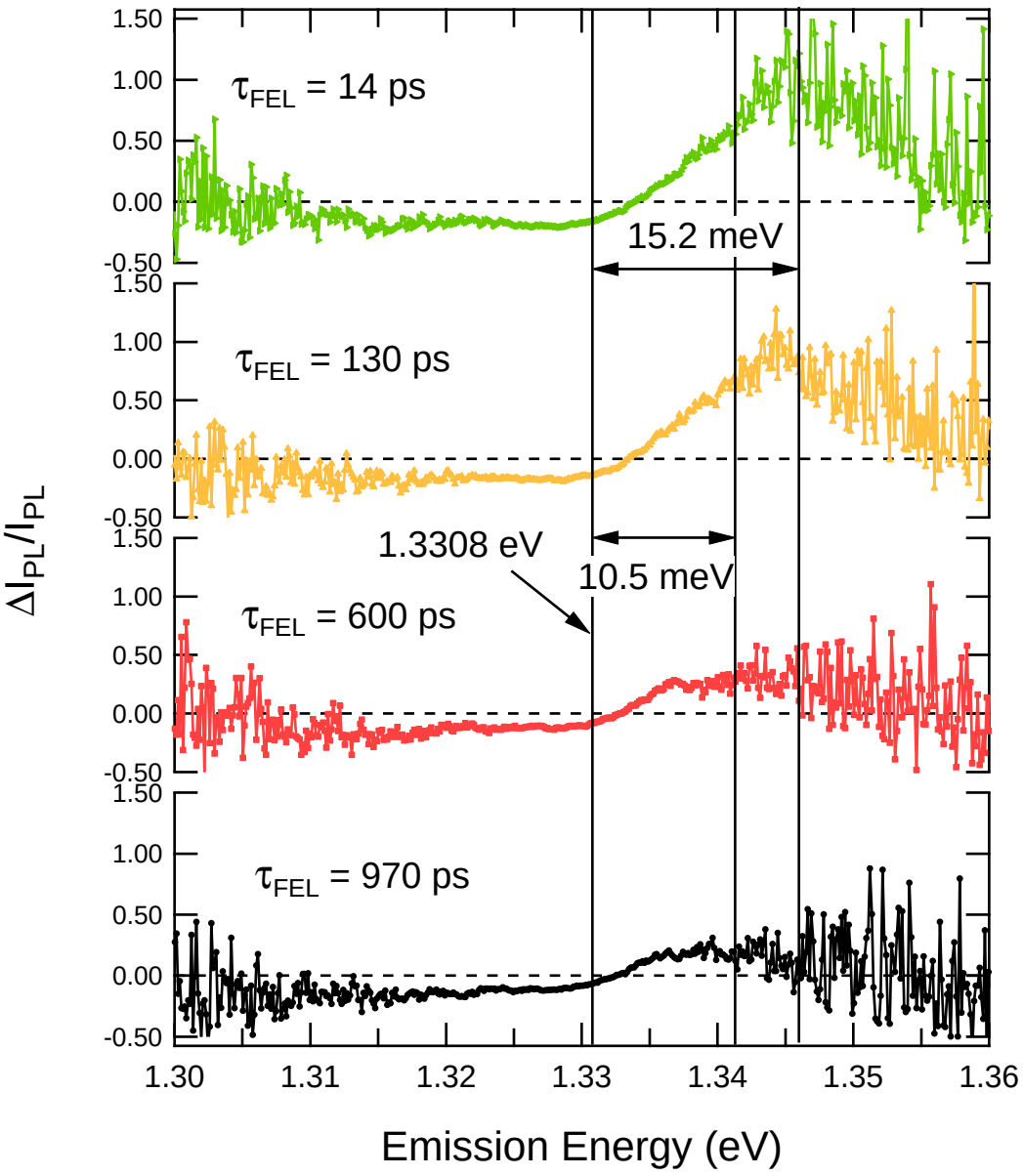

Figure 4.9 : Differential time-integrated PL for the data presented in Fig. 4.8(a). The center of the 1*s* emission is demarcated at 1.3308 eV, as well as the 2*s* emission energy, which is roughly 10.5 meV above the 1*s*. A large PL enhancement is seen at early pump-quench time delays at 15.2 meV above the 1*s* center emission; at larger values of τ_{FEL}, this THz-induced PL enhancement disappears.

we observe a large emission enhancement at 15.2 meV, which corresponds to an energy above the binding energy of the exciton. Given the small value of $I(E,0)$ at these energies, this increase may be small in absolute terms. Nevertheless, this high energy emission disappears as τ_{FEL} increases, suggesting that the enhancement at 15.2 meV is from heated carriers: band-to-band transitions can occur at finite momentum values, which occur because of the heating due to the THz radiation, if Δk is very close to zero. These finite momentum species luminescence at higher energies because they are not at the bottom (top) of the $1s$ exciton band (heavy-hole valence band).

4.4.2 Time-Resolved Photoluminescence Quenching

The evidence of THz-induced enhancement of the $2s$ emission shown by the time-integrated traces seen in Fig. 4.9 required further investigation. Using a streak camera, we used TRPL to examine the system before, during, and after the THz pulse. Specifically, we wanted to know at which point the $2s$ enhancement was occurring, how long it lasted, and what happened to the $1s$ emission. This sub-section details the results of our TRPL experiments at multiple THz wavelengths, field strengths, and pump-quench time delays.

Figure 4.10(a) shows a typical TRPL image created using a Ti:Sa excitation pulse after a dark spectrum has been subtracted. For this TRPL trace, we measured the PL with the FEL pulse delayed roughly 2 ns later in time (outside the streak camera range), which accounted for time-averaged lattice heating effects from absorption of the FEL; we considered this FEL-shifted TRPL trace to be a reference spectra. When the THz pulse is within the streak camera range, a prominent decrease in the TRPL can clearly be observed, as is seen in Fig. 4.10(b). As compared to the reference trace, this spectrum has PL that is both longer-lived and energetically-broadened. In this particular example, the THz quenching pulse has a peak field strength of $\sim$0.27 kV/cm and a THz photon energy of 10.5 meV, which

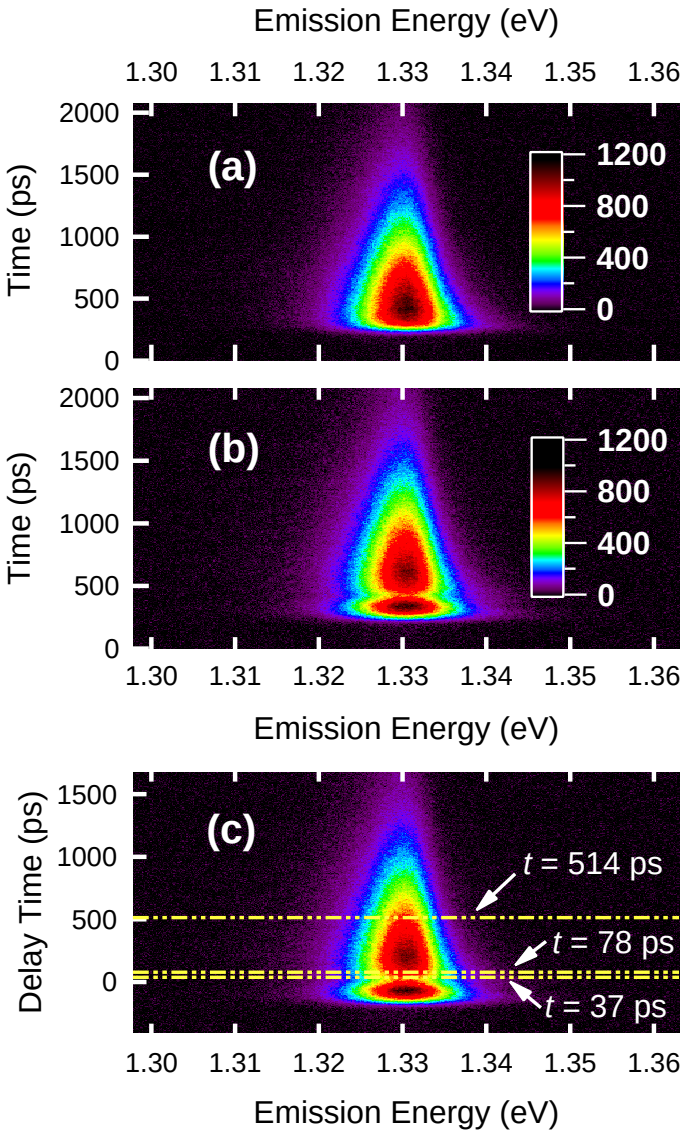

Figure 4.10 : TRPL contour maps of data taken when the 118 μm, 0.27 kV/cm THz pulse is at (a) τ_{FEL} $\sim$2 ns and (b) τ_{FEL}=130 ps. The time axis is given in absolute terms, instead of relative to the arrival of the THz pulse. (c) Subfigure (b) plotted with the relative pump-quench time delay as the y-axis. Horizontal cuts are taken at three times after the arrival of the THz pulse at t = 0 ps: 37, 78, and 514 ps. Figure adapted from [134].

is on-resonance with the 1s-2p intra-exciton transition energy. For all THz wavelengths examined, except for 32 μm, we observed a quench of the PL at the 1s exciton emission energy.

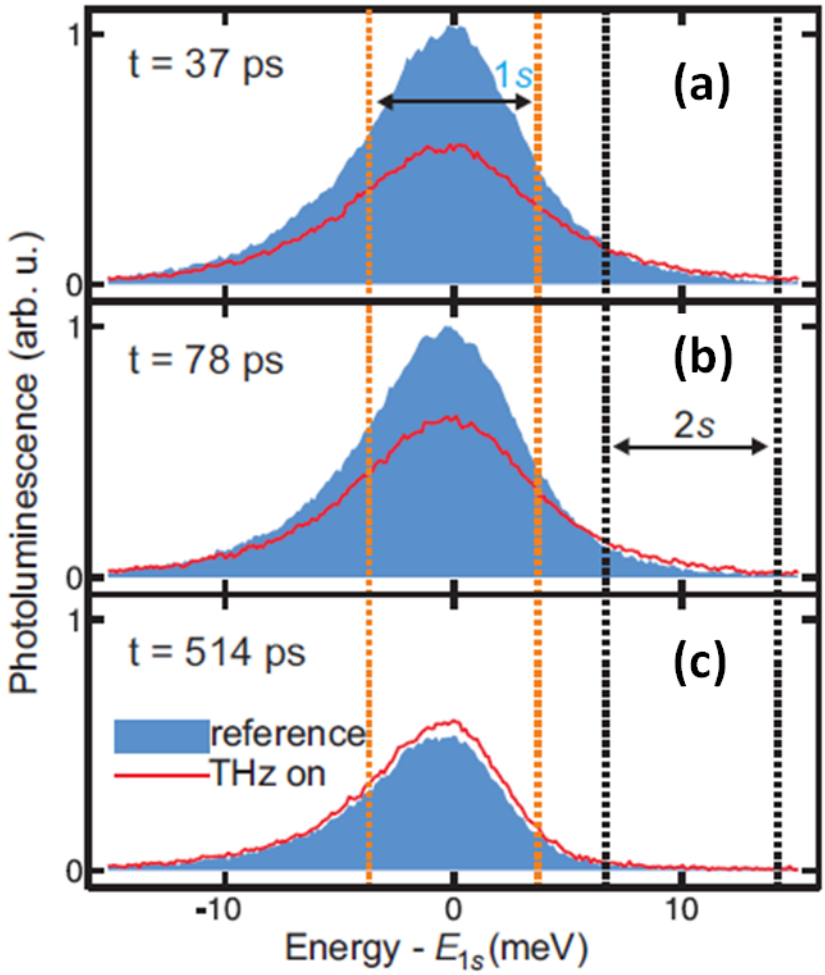

Figure 4.11 : Emission energy slices taken at 37, 78, and 514 ps after the THz pulse, as indicated in Fig. 4.10(c). The shaded blue curves represent the reference trace [Fig. 4.10(a)] and red lines represent when the THz pulse is at τ_{FEL} = 130 ps. In all cases, decrease in the 1s PL intensity is seen; in both (a) and (b), a very slight increase in the 2s emission intensity is observed, as well. Figure adapted from [134].

The absence of any PL quench for $\lambda_{FEL} = 32$ μm can be seen in Fig. 4.12. We attribute

this observation to the fact that there is very little coupling to the THz radiation at this wavelength. We observe THz-induced heating in several of the TRPL and time-integrated traces, a fact we ascribe to 32 μm being close to the transverse optical phonon mode. In addition to the intersubband and intra-excitonic transitions lying away from this photon energy, the Drude-like response is also much smaller than at the other, longer THz wavelengths examined. Given the lack of quenching and small set of data for the 32 μm case, we will concentrate on the other three THz wavelengths (61, 118, and 200 μm).

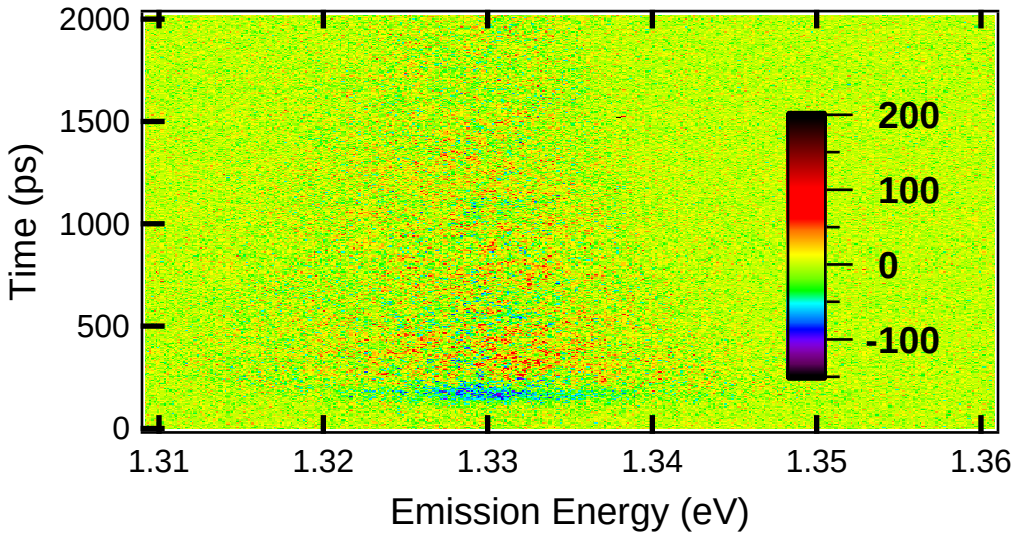

Figure 4.12 : Difference TRPL contour map with a 32 μm, $\sim$3.6 kV/cm THz pulse. No quench is observed for the 32 μm case. The blue at $\sim$200 ps is mostly likely due to the incomplete subtraction of the sample and reference traces. A rough estimate of the pump-quench delay time is 400 ps.

If we subtract the reference from the sample trace in Fig. 4.10 and divide by the reference [same procedure used in Eq. (4.6)], we obtain the difference in the TRPL created by the THz pulse [Fig. 4.13(a)]. The remarkable suppression of the PL emission from the 1s energy state is clearly shown in the difference TRPL map. At τ_{FEL} = 0 ps (beginning of FEL pulse), this PL begins to decrease, finally coming to its minimum at $\tau_{FEL} \approx$ 100 ps.

Interestingly, we see weak PL emission increase at higher emission energies near the maximum of the PL quench. In addition, a PL enhancement can be seen at the 1*s* excitonic emission energy after several hundreds of picoseconds.

For a better quantitative understanding of the difference TRPL data given in Fig. 4.13(a), we integrated across the 1*s* and 2*s* emission energies, as shown by the yellow and blue dotted lines, respectively. The 2*s* emission linewidth was assumed to be the same as the 1*s* linewidth ($\sim$7 meV). The results of the PL integration, which are presented in Fig. 4.13(b) and (c), show that as the luminescence from the 1*s* emissive state decreases, the 2*s* emission increases. After several hundred picoseconds, the 2*s* induced-emission trends to zero, while the 1*s* difference becomes positive. It takes nearly 2 ns for the 1*s* emission to recover back to its non-THz radiation influenced behavior.

We used the spectrometer without the streak camera (time-integrated PL) to show that the PL with and without THz was fully conserved when lattice heating effects are very small (e.g. with long wavelengths or low THz powers). This conservation is shown in Fig. 4.14 for $\lambda_{\mathrm{FEL}} = 200$ μm for a variety of delay times. For all delay times examined, we see that the ratio of the quenched integrated spectrum to the non-quenched integrated spectrum is within 0.03 of 1.00, similar to the low THz field data taken on GaAs by Liu *et al.* [132]. Therefore, we can conclude that the temporal decrease in PL at early delay times is compensated by the enhanced PL at later delay times. PL conservation also implies that no electron-hole pairs were heated or excited outside the quantum wells into the barriers.

In addition to investigating the appearance of THz-induced 2*s* luminescence, we also looked at how the 1*s* emission behaved using different THz wavelengths, THz field strengths, and pump-quench delay times. Figure 4.15 shows the results of changing τ_{FEL} while holding the THz field (0.92 kV/cm) and THz wavelength (61 μm) constant. Although difficult to see, the PL quench becomes larger as the pump-quench time delay is increased. This obser-

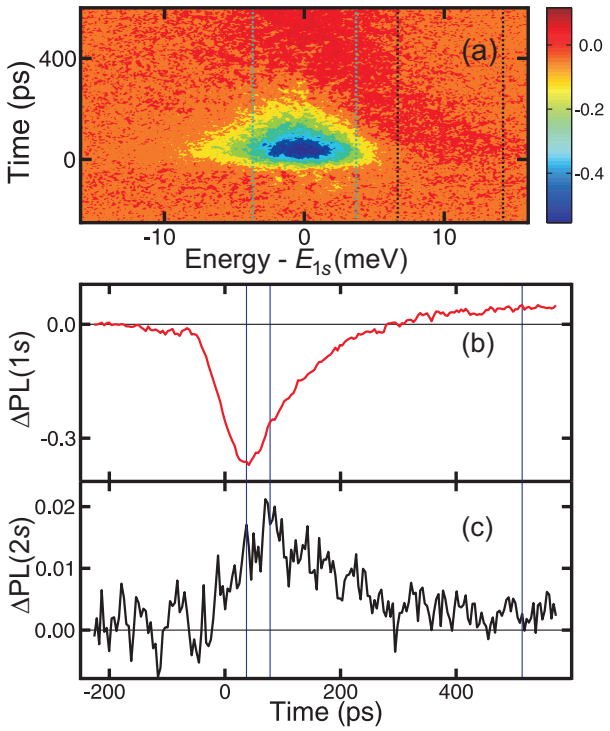

Figure 4.13 : (a) Differential TRPL contour map produced by a 118 μm, $\sim$0.27 kV/cm THz pulse at a pump-quench delay time of 130 ps. Blue dashed lines indicate the estimated 1s emission linewidth, while the black dashed lines represent the 2s emission linewidth. The results of the integration of the (b) 1s emission and (c) 2s emission obtained from (a) as a function of time delay. The PL quench occurs at the 1s energy, while emission enhancement is observed at the 2s energy. The vertical blue lines at 37, 78, and 514 ps show where the emission energy cuts presented in Figs. 4.10(c) and 4.11 are. Figure adapted from [134].

vation suggests that exciton formation dynamics play an important role in TRPL quenching: as the system becomes more excitonic, the ability of the THz field to temporarily suppress the 1s emission becomes larger.

To gain deeper insight, we can plot the differential $(\Delta I/I)$ for each delay time in Fig. 4.15. To correctly obtain the differential PL, we scaled the intensity and shifted the timing of the reference traces so that the PL intensity and Ti:Sa excitation time were the same as the sample traces. The scaling and horizontal shifting were necessary to account for the power fluctuations of the Ti:Sa and temporal drifting of the streak camera, respectively. We used a

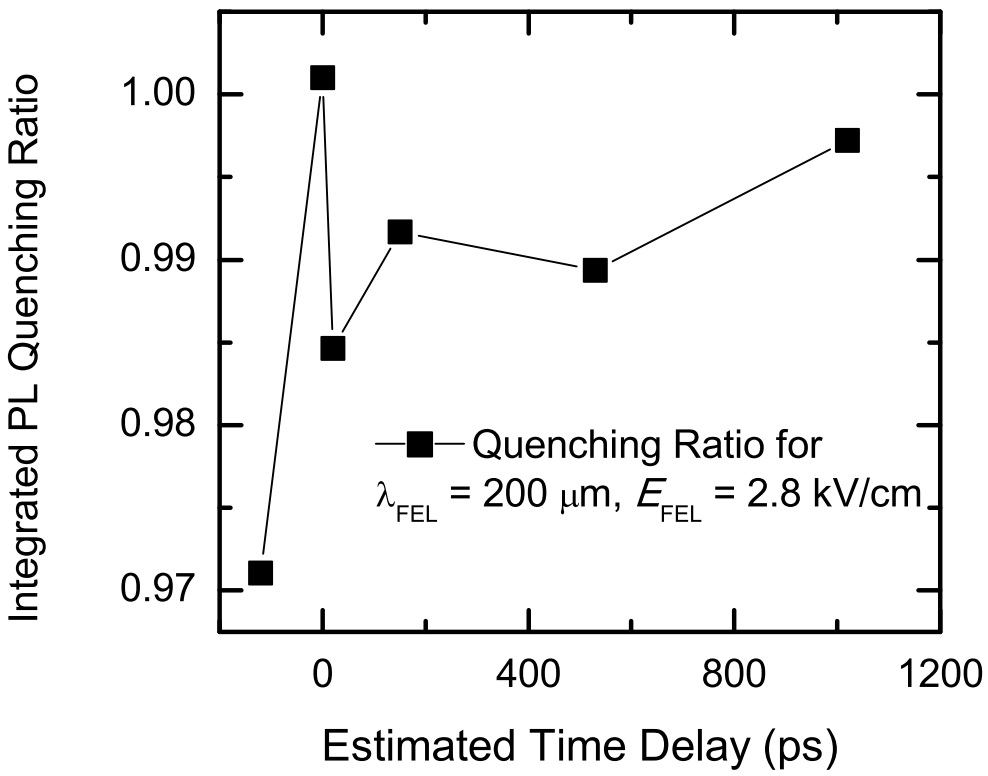

Figure 4.14 : PL quenching ratio versus time delay for 200 μm. A value of 1.00 indicates that all of the emission energy is fully conserved. As can be seen, regardless of the pump-quench time delay, the quenching ratio stays within 0.03 of 1.00.

quick minimization routine to do this scale and shift procedure for times before the entry of the THz pulse. Typical intensity deviations were less than 2% and rarely did the horizontal time shift above $\pm$8 ps (two temporal data points). This operation highlighted the physics (PL quench) and minimized the experimental artifacts.

Figure 4.16 shows the differential intensities resulting from the data presented in Fig. 4.15. The large noise in the first $\sim$200 ps of the curve is due to the very small intensity values of the reference trace before the Ti:Sa excitation pulse. As the time delay is changed from 370 ps to 980 ps, the magnitude of the quench becomes larger, although the change is rather small. More prominently, the post-pulse 1s dynamics changes substantially as the

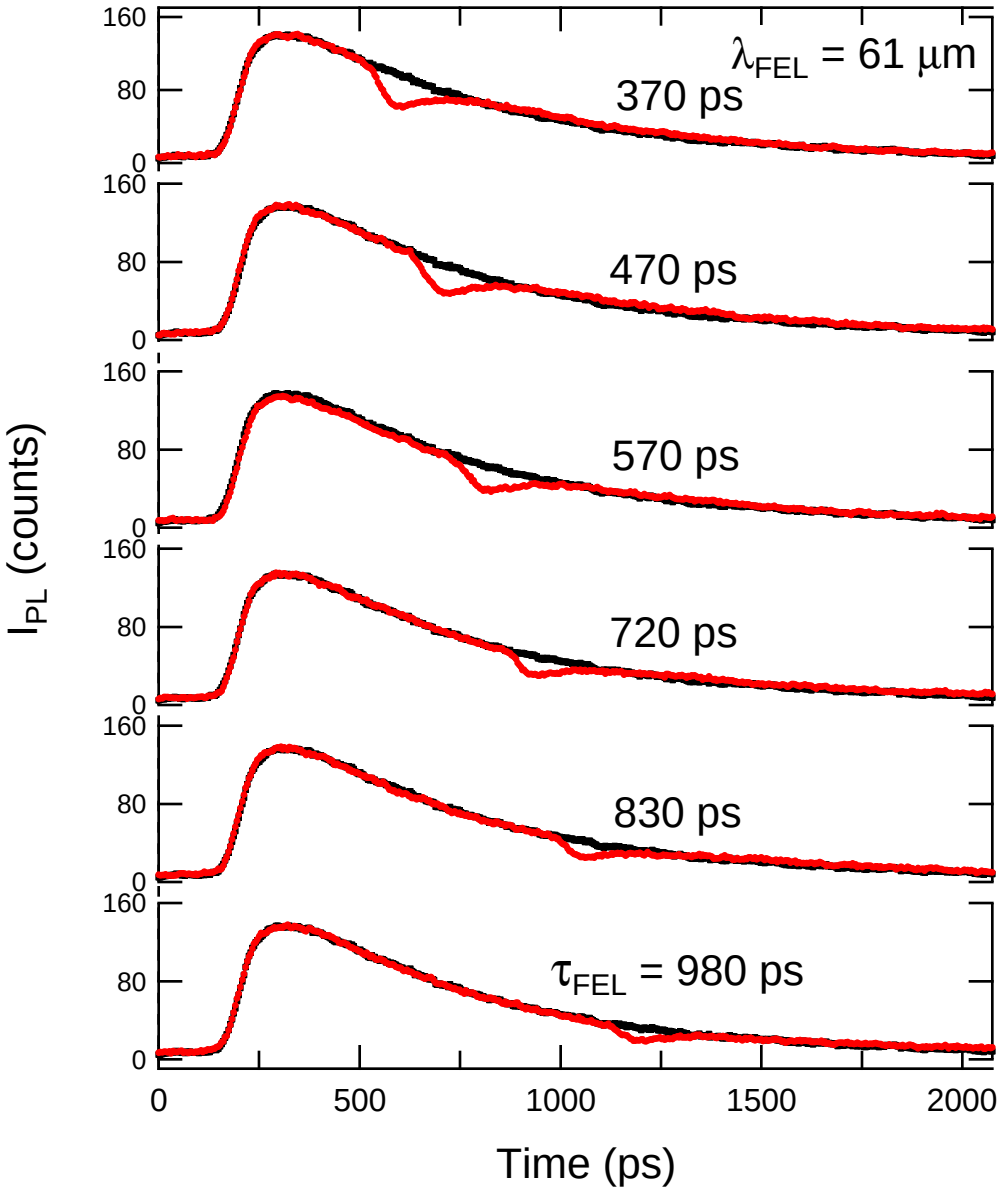

Figure 4.15 : 1*s* PL emission with the 61 μm THz pulse at different delay times. The red traces show the quenching behavior when the THz pulse is in the streak camera field of view, while the black traces result from when the THz pulse is delayed by over 2 ns from the Ti:Sa excitation. The x-axis is in absolute time, while the values of τ_{FEL} are given in relative time.

time delay increases. As τ_{FEL} becomes larger, both the magnitude and duration of the $1s$ enhancement increase. This observation may be due to the decrease of excitons and photogenerated free carriers at long time delays, which may increase the decay time of excited species down to the $1s$ level. We will see in the next section that this same trend is seen for all THz wavelengths investigated.

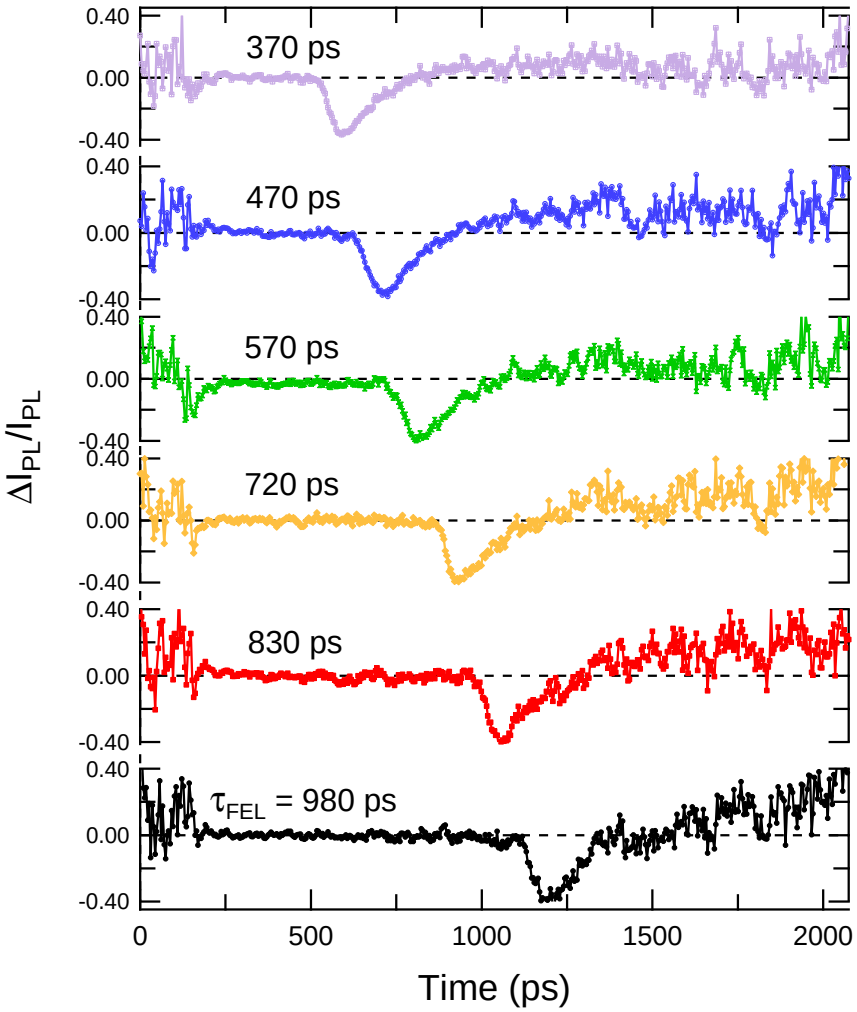

Figure 4.16 : Differential PL at $\lambda_{FEL} = 61$ μm and E_{FEL} = 0.92 kV/cm for the traces presented in Fig. 4.15. As the pump-quench time delay, τ_{FEL} is increased from 370 ps to 980 ps, the depth of the quench becomes larger.

4.5 Analysis

The surprising evidence of THz-induced 2s emission, which seems to violate conservation of angular momentum, raised numerous questions. The two main explanations for this observation were: (1) symmetry breaking of the 2p-2s transition or (2) high energy PL from THz radiation-heated electrons and holes. From the work done by Mackillo Kira and Stephan Koch [138, 139], we knew that the 2p-2s transition was at least possible. We worked with theorists from Philipps-Universität in Marburg, Germany (Lukas Schneebeli, Benni Breddermann, Mackillo Kira, and Stephan Koch) to create simulations based on the theoretical work done by Kira and Koch to see if our data could be correctly explained by their theory. At the same time, the issue of THz radiation heating was directly addressed by analyzing the electron-hole plasma temperature with and without the presence of the THz pulse to determine if heating was responsible for the higher energy emission. These results are presented in the first part of this section. The second part of this section looks at the TRPL quenching trends that were seen for various pump-quench time delays, THz field strengths, and THz wavelengths. By plotting the maximum differential PL quench depth versus these THz parameters, we sought to gain insight into the THz-induced PL quenching mechanism.

4.5.1 Intra-Excitonic Scattering

Photoluminescence from Terahertz Radiation-Induced Heating

In principle, a THz excitation can induce elevated levels of photoluminescence (PL) also by heating the carriers because that process may increase luminescence from the plasma with respect to the 1s resonance. To confirm that the enhanced 2s PL in the data cannot be attributed to such a heating, we analyzed the carrier-temperature change induced by the

THz excitation. As shown in Chatterjee *et al.* [128], the temperature of the carriers can be deduced from the high-energy tail of the PL, proportional to $\exp(-E/k_{\mathrm{B}}T)$.

Figure 4.17 illustrates this method of temperature analysis of the experimental data. It shows the same spectra as seen in Fig. 4.11(b) ($\lambda_{\mathrm{FEL}} = 118$ μm, τ_{FEL} = 130 ps) together with the resulting exponential temperature fits (red solid lines): panel (a) is the reference spectrum and (b) the "THz-on" spectrum. For the reference case, the PL tail decays exponentially starting roughly from 5 meV above the 1s resonance because the 2s resonance is weak. Since the THz radiation excitation induces elevated 2s PL, the "THz-on" case produces exponential decay that start at higher energy, roughly 10 meV above the 1s state, than for the reference. In both cases, the PL tail decays exponentially up to the experimental noise-floor level.

Interestingly, we find that the reference case yields T = 28.3 K while "THz-on" produces T = 27.6 K. Therefore, THz field excitation induces even a slight *cooling* of carriers related to reduced kinetic energy of the 2s state, compared with the 1s state. Hence, this analysis unambiguously shows that the THz pulse does not induce heating at the time when enhanced 2s PL is observed. Thus, the THz-induced 2s emission is not generated via heating.

Further insight into the heating of the carriers by a THz pulse can be obtained by computing the average photon energy E at the high-energy tail of the PL. The energy integration includes only the energy range around the 2s resonance as indicated by the vertical lines in Fig. 4.18. A definition of E can be defined as:

$$E(t) = \frac{\int_{2s} \mathrm{d}E\,(E - E_{1s})\,\mathrm{PL}(E,t)}{\int_{2s} \mathrm{d}E\,\mathrm{PL}(E,t)}. \tag{4.7}$$

If the THz radiation heats the system, this energy E must increase; if E decreases, then cooling is being observed. We compute the differential average energy $\Delta E = E(\mathrm{THz\ on}) -$

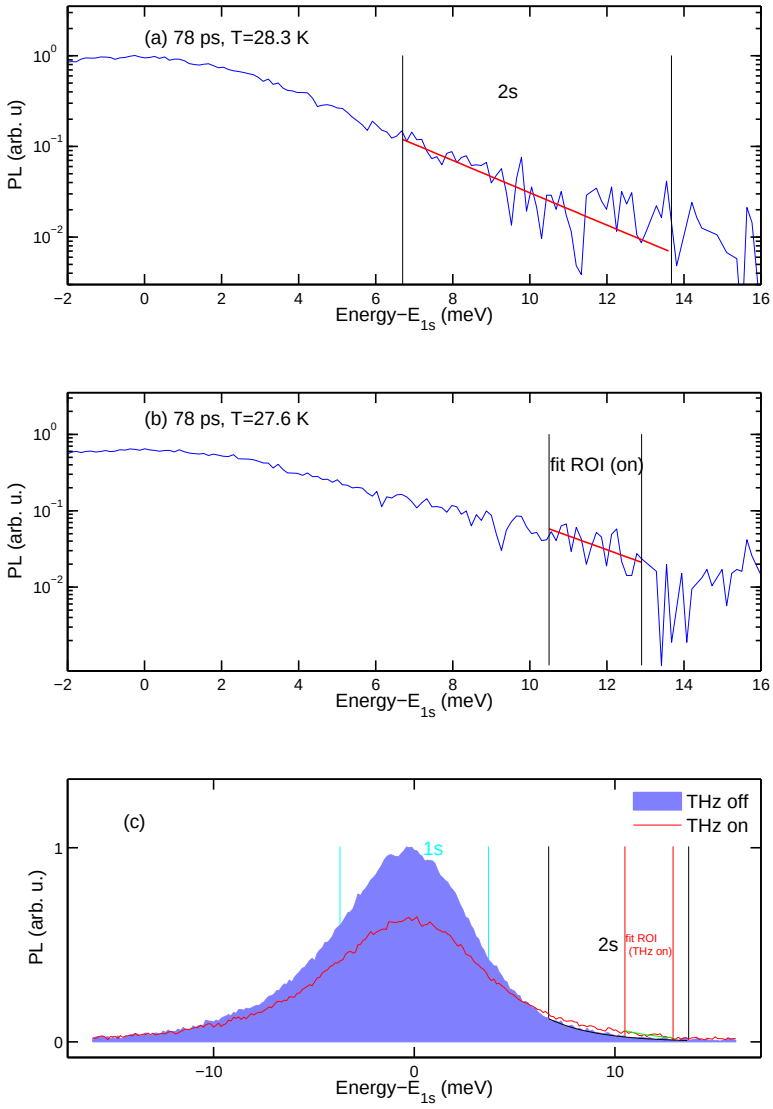

Figure 4.17 : (a) PL intensity spectral slice versus subtracted energy emission when the THz pulse is at ≈2 ns ("THz off"). The temperature of the electron-hole plasma from the Boltzmann tail is found to be T=28.3 K. (b) Same as in (a), except τ_{FEL}=78 ps. A plasma temperature of 27.6 K is found, which is very close to the temperature found in (a). The region of interest (ROI) is taken at energies above the 2s emission peak. (c) Spectral slices versus subtracted energy emission for $\tau_{FEL} \approx 2$ ns (shaded blue curve, "THz off") and $\tau_{FEL} = 78$ ps (red curve, "THz on"). The cyan lines indicate the energetic range of the 1s emission, the black lines show the 2s emission range, and the red lines delineate the ROI used in (b). Figure adapted from [134].

$E(\text{THz off})$ such that ΔE is positive when there is THz-induced heating and negative when the THz pulse cools the system.

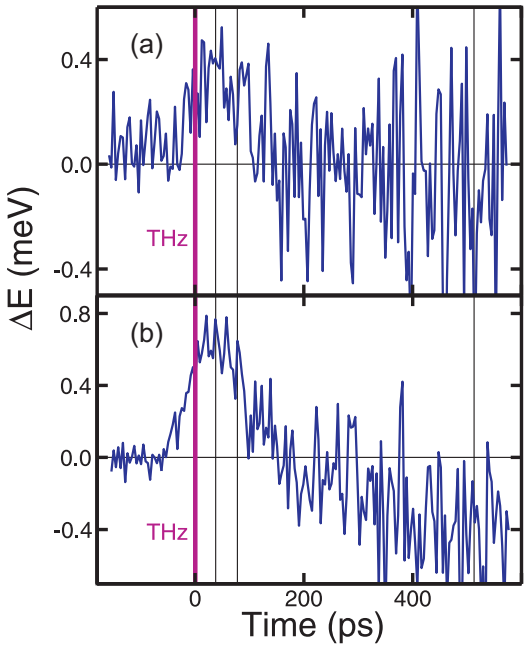

Figure 4.18 : Observed differential average energy as a function of time (a) 0.27 kV/cm (12 mW) and (b) 1.1 kV/cm (200 mW) THz power.

Figure 4.18 shows the differential average energy ΔE as function of time. In Fig. 4.18(a), we took the spectrum at $\lambda_{\text{FEL}} = 118\ \mu$m and $E_{\text{FEL}} = 0.27$ kV/cm (12 mW), while Fig. 4.18(b) uses $\lambda_{\text{FEL}} = 118\ \mu$m and $E_{\text{FEL}} = 1.1$ kV/cm (200 mW). For the low electric field case, we observe that the THz excitation induces heating only in a short time window around the center of the THz pulse. After that, between 100 and 500 ps, no THz-induced heating is observed, since ΔE oscillates around zero. The high electric field case shown in Fig. 4.18(b) shows the cooling trend even more clearly: after the THz pulse, we observe a cooling of the electron-hole plasma as compared to the "THz-off" case, as evidenced by $\Delta E < 0$. Since positive $2s$ excess [see Fig. 4.13] is observed in this time range, THz-induced heating can

be excluded as a source for enhanced $2s$ emission, in agreement with the Boltzmann tail analysis done in Fig. 4.17.

Coulomb-Induced Symmetry Breaking

To explain the emergence of the $2s$ PL increase, $1s$ shelving, and relaxation phenomena, we theoretically examine the effects of THz radiation on photogenerated electron-hole pairs [138]. Microscopic properties of excitons are defined by two-particle correlations $c_{\mathrm{X}}^{\mathbf{q},\mathbf{k}',\mathbf{k}} \equiv \Delta\langle e_{\mathbf{k}}^{\dagger} h_{\mathbf{k}-\mathbf{q}}^{\dagger} h_{\mathbf{k}'} e_{\mathbf{k}'+\mathbf{q}}\rangle$ between Fermionic electron $e^{\dagger}e$ and hole $h^{\dagger}h$ density operators [139]. The crystal momentum of each particle is given by $\hbar\mathbf{k}$. The corresponding electron (hole) distribution is denoted as $f_{\mathbf{k}}^{\mathrm{e}} = \langle e_{\mathbf{k}}^{\dagger} e_{\mathbf{k}}\rangle$ $\left(f_{\mathbf{k}}^{\mathrm{h}} = \langle h_{\mathbf{k}}^{\dagger} h_{\mathbf{k}}\rangle\right)$. The full many-body dynamics of c_{X} is given by [139]

$$\begin{aligned} \mathrm{i}\hbar\frac{\partial}{\partial t} c_{\mathrm{X}}^{\mathbf{q},\mathbf{k}',\mathbf{k}} &= E_{\mathbf{k},\mathbf{k}',\mathbf{q}}^{\mathrm{eh}} c_{\mathrm{X}}^{\mathbf{q},\mathbf{k}',\mathbf{k}} \\ &\quad + (1 - f_{\mathbf{k}}^{\mathrm{e}} - f_{\mathbf{k}-\mathbf{q}}^{\mathrm{h}}) \sum_{\mathbf{l}} V_{\mathbf{l}-\mathbf{k}} c_{\mathrm{X}}^{\mathbf{q},\mathbf{k}',\mathbf{l}} \\ &\quad - (1 - f_{\mathbf{k}'+\mathbf{q}}^{\mathrm{e}} - f_{\mathbf{k}'}^{\mathrm{h}}) \sum_{\mathbf{l}} V_{\mathbf{l}-\mathbf{k}'} c_{\mathrm{X}}^{\mathbf{q},\mathbf{l},\mathbf{k}} \\ &\quad + T^{\mathbf{q},\mathbf{k}',\mathbf{k}} - \mathbf{A}_{\mathrm{THz}}(t) \cdot \mathbf{j}_{\mathbf{k}'+\mathbf{q}-\mathbf{k}} c_{\mathrm{X}}^{\mathbf{q},\mathbf{k}',\mathbf{k}}, \end{aligned} \tag{4.8}$$

where $E_{\mathbf{k},\mathbf{k}',\mathbf{q}}^{\mathrm{eh}}$ contains the renormalized energy of an electron-hole pair, $V_{\mathbf{k}}$ is the Coulomb-matrix element, $T^{\mathbf{q},\mathbf{k}',\mathbf{k}}$ stems from three-particle scattering, $\mathbf{A}_{\mathrm{THz}}(t)$ is the vector potential of the THz pulse, and $\mathbf{j}_{\mathbf{k}} = -e\hbar\mathbf{k}/\mu$ is the current matrix element, where μ is the reduced mass of an electron-hole pair. Exciton distributions $\Delta N_{\mathbf{q}}^{\lambda,\lambda}$ follow from c_{X} using the transformation

$$\Delta N_{\mathbf{q}}^{\lambda,\nu} = \sum_{\mathbf{k},\mathbf{k}'} \phi_{\lambda}(\mathbf{k})\, \phi_{\nu}(\mathbf{k}') c_{\mathrm{X,CM}}^{\mathbf{q},\mathbf{k}',\mathbf{k}} \tag{4.9}$$

where $\phi_{\lambda}(\mathbf{k})$ defines the exciton wave function. It is straightforward to show that the THz field generates polarization $\Delta N_{\mathbf{q}}^{\lambda,\nu\neq\lambda}$ through dipole coupling $\mathbf{J}_{\lambda,\nu} = \sum_{\mathbf{k}} \phi_{\lambda}^{\star}(\mathbf{k}) \mathbf{j}_{\mathbf{k}} \phi_{\nu}(\mathbf{k})$.

Since $\mathbf{J}_{1s,2s}$ is dipole forbidden while $\mathbf{J}_{1s,2p}$ is dipole allowed, the THz field directly couples only $1s$ and $2p$ excitons whereas there is no coupling between the $1s$ and $2s$ states. However, the Coulomb-induced three-particle $T^{\mathbf{q},\mathbf{k}',\mathbf{k}}$ breaks this symmetry, producing significant scattering to the $2s$ state. The three-particle correlation term is created through Coulomb (V), photon (E), and phonon interactions (Q). Because our sample was held at 5 K, the phonon density is very low, so this term will not generate significant contributions to $T^{\mathbf{q},\mathbf{k}',\mathbf{k}}$. The general, explicit form of T is a function of three correlation states, which form triplet terms [139]

$$\begin{aligned}
T^{\mathbf{q}_\parallel,\mathbf{k}'_\parallel,\mathbf{k}_\parallel}_{\lambda,\nu;\nu',\lambda'} \equiv & \sum_{k_3,l} V_l \left[\Delta\langle \mathbf{k}_1^\dagger \mathbf{k}_2^\dagger \mathbf{k}_{3l}^\dagger \mathbf{k}_3 \mathbf{k}_{2'q} \mathbf{k}_{1'(q-l)}\rangle + \Delta\langle \mathbf{k}_1^\dagger \mathbf{k}_2^\dagger \mathbf{k}_{3l}^\dagger \mathbf{k}_3 \mathbf{k}_{2'(q+l)} \mathbf{k}_{1'q}\rangle\right] \\
& - \sum_{k_3,l} V_l \left[\Delta\langle \mathbf{k}_1^\dagger \mathbf{k}_{2l}^\dagger \mathbf{k}_3^\dagger \mathbf{k}_{3l} \mathbf{k}_{2'q} \mathbf{k}_{1'q}\rangle + \Delta\langle \mathbf{k}_{1l}^\dagger \mathbf{k}_2^\dagger \mathbf{k}_{3l}^\dagger \mathbf{k}_3 \mathbf{k}_{2'q} \mathbf{k}_{1'q}\rangle\right] \\
& - \sum_{l} \left[\Delta\langle E^{\bar{\lambda}'}_{l_\parallel} \mathbf{k}_1^\dagger \mathbf{k}_2^\dagger \mathbf{k}_{2'q} \bar{\mathbf{k}}_{1'(q+l)}\rangle + \Delta\langle E^{\bar{\nu}'}_{-l_\parallel} \mathbf{k}_1^\dagger \mathbf{k}_2^\dagger \bar{\mathbf{k}}_{2'(q+l)} \mathbf{k}_{1'q}\rangle\right] \\
& + \sum_{l} \left[\Delta\langle E^{\nu}_{l_\parallel} \mathbf{k}_1^\dagger \bar{\mathbf{k}}_{2l}^\dagger \mathbf{k}_{2'q} \mathbf{k}_{1'q}\rangle + \Delta\langle E^{\lambda}_{-l_\parallel} \bar{\mathbf{k}}_{1l}^\dagger \mathbf{k}_2^\dagger \mathbf{k}_{2'q} \mathbf{k}_{1'q}\rangle\right] \\
& + \sum_{l} \left[\Delta\langle Q^{\lambda'}_{l_\parallel} \mathbf{k}_1^\dagger \mathbf{k}_2^\dagger \mathbf{k}_{2'q} \mathbf{k}_{1'(q+l)}\rangle + \Delta\langle Q^{\nu'}_{-l_\parallel} \mathbf{k}_1^\dagger \mathbf{k}_2^\dagger \mathbf{k}_{2'(q+l)} \mathbf{k}_{1'q}\rangle\right] \\
& - \sum_{l} \left[\Delta\langle Q^{\nu}_{l_\parallel} \mathbf{k}_1^\dagger \mathbf{k}_{2l}^\dagger \mathbf{k}_{2'q} \mathbf{k}_{1'q}\rangle + \Delta\langle Q^{\lambda}_{-l_\parallel} \mathbf{k}_{1l}^\dagger \mathbf{k}_2^\dagger \mathbf{k}_{2'q} \mathbf{k}_{1'q}\rangle\right]. \qquad (4.10)
\end{aligned}$$

Here, k is a correlation annihilation and $k^\dagger$ is a correlation creation; the specific definitions of these terms can be found in [139]. The three-particle correlation terms create microscopic scattering from one two-particle correlation state to another, provided that it is mediated by the some external potential (e.g., photons).

It is interesting to note that one must fully include the fundamental diffusive nature of $T^{\mathbf{q},\mathbf{k}',\mathbf{k}}$, i.e. $\sum_{\mathbf{k},\mathbf{k}',\mathbf{q}} T^{\mathbf{q},\mathbf{k}',\mathbf{k}} = 0$ [139], to explain the $2p$ to $2s$ many-body scattering. By diffusive, we mean that scattering does not create nor destroy the macroscopic total electron-hole correlation, but re-distributes them in k space in a microscopic sense [139]: a correlation

at a momentum, k, is scattered to a new momentum, k', where $k' = k + q$. It is important to mention that a simple dephasing approximation, that is replacing $T_{\mathrm{X}}^{\mathbf{q},\mathbf{k}',\mathbf{k}}$ by $-i\gamma c_{\mathrm{X}}$ in Eq. (4.8), does not produce the symmetry breaking needed to explain the THz-field-induced $1s$-to-$2s$ transition: when correlations are not macroscopically conserved, symmetry breaking is not generated.

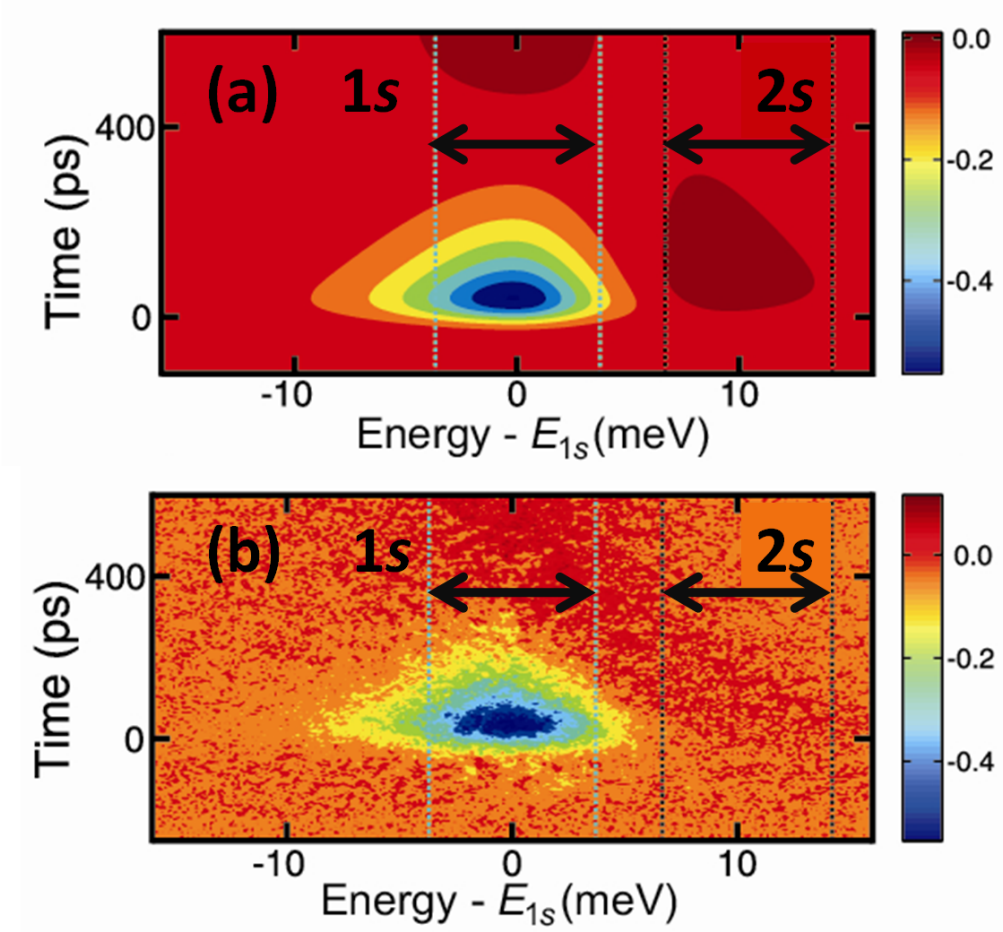

Figure 4.19 : (a) Theoretical and (b) experimental differential contour map. (a) is created using inputs that correspond to the experimental parameters used to generate (b). The emission quench, $1s$ recovery, and induced $2s$ emission seen in (b) are all reproduced in (a). Figure adapted from [134].

We solve Eq. (4.8) for the THz excitation used to generate the data in Figs. 4.10 and 4.13

and fully include the diffusive Coulomb scattering. Figure 4.19(a) shows the computed results for the same conditions as in Fig. 4.19(b); we find quantitative agreement between the experimental and theoretical results. In particular, positive 2*s* signal and 1*s* quenching are both observed clearly, as well as a time delay between the 1*s* quench and the enhanced 2*s* response [Figs. 4.13(b) and 4.13(c)]. Furthermore, the 1*s* shelving is also observed theoretically [Fig. 4.20(a)].

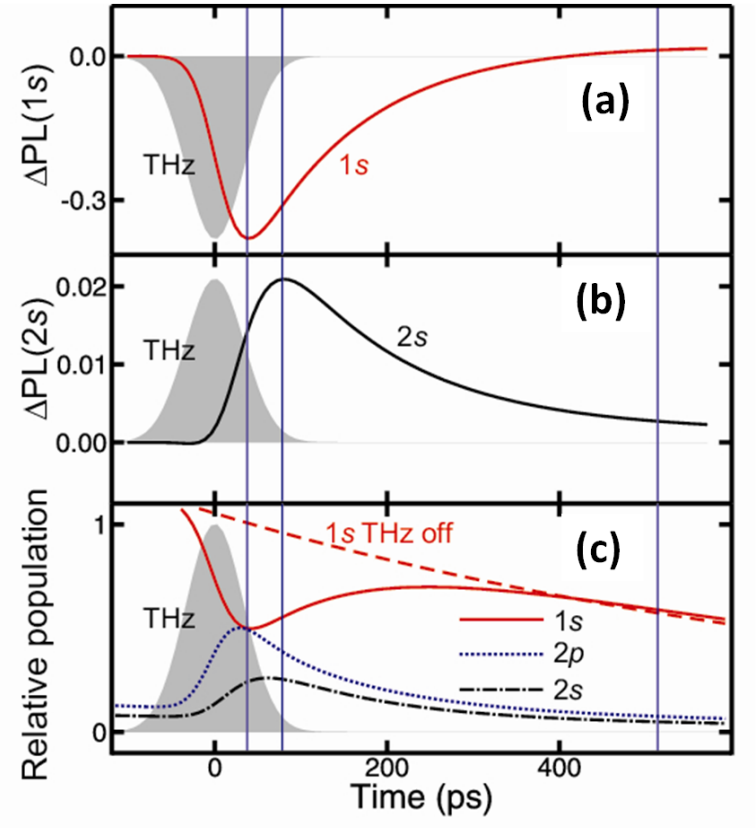

Figure 4.20 : Simulated differential (a) 1*s* (red line) and (b) 2*s* (black line) PL emission induced by the presence of a resonant THz pulse (shaded gray). The 1*s* quench, recovery, and enhancement, which are seen in experiment, are all expected from theory. (c) The exciton populations of the 1*s* (red line), 2*s* (black dashed line), and 2*p* (blue dashed line) state as a function of delay time. The THz (shaded gray) creates a marked change in the population of the 1*s* state, as evidenced by the trace with no-THz (red dashed line). Figure adapted from [134].

To clarify how the THz field influences, or manipulates, intra-exciton dynamics, we also plot the $1s$, $2s$, and $2p$ exciton populations in Fig. 4.20(c) as a function of delay time. We find that the THz excitation induces transitions $1s \rightarrow 2p \rightarrow 2s$ in that order. When we switch off the diffusive $T^{\mathbf{q},\mathbf{k}',\mathbf{k}}$ scattering, no $2s$ population emerges, which verifies that the enhanced $2s$ PL indeed arises from the Coulomb-induced symmetry breaking. In particular, the diffusive scattering induces significant scattering between the $2p$ and $2s$ populations, which explains the temporal delay between the $1s$ quench and $2s$ buildup. We find that both experimentally and theoretically the relative change in the $1s$ and $2s$ signals is 40% and 2%, respectively, which is very similar to experimental observations [see Fig. 4.13(b)]. Additionally, when the THz field strength is increased, we observe in both theory and experiment that the $1s$ and $2s$ signals saturate to roughly 58% and 2.3%, respectively, and the time delay between the $1s$ quench and $2s$ enhancement becomes as long as 100 ps for a THz electric field of 1.6 kV/cm (405 mW).

4.5.2 Photoluminescence Quenching

Figure 4.16 showed small differences in the quenching response that emerged when the pump-quench delay time was changed by nearly a factor of three. Data collected over orders of magnitude in both time delay and THz field strength reveal much more about the quenching dynamics. If we take the maximum depth of the differential quench for each THz wavelength and plot it versus the transmitted electric field for a set of pump-quench delay times, we obtain Fig. 4.21. This figure shows that as the electric field is increased, regardless of τ_{FEL}, we observe that the differential quench saturates. This behavior is prominently seen in Fig. 4.21(a) for $\lambda_{\mathrm{FEL}} = 118$ μm (green trace) whereby the quench does not exceed 0.85 regardless of the electric field strength. Some of the saturation behavior is due to lattice heating. In particular, when $\lambda_{\mathrm{FEL}} = 61$ μm, the differential quench not only ceases to

become larger at increased electric fields, but it also decreases [see, e.g., Fig. 4.21(a)–(c)]. Interestingly, it appears as though when the THz wavelength is at 200 μm, the differential quench maximum does not saturate as readily, as with shorter wavelengths. Given that we could not access higher 200 μm fields, this observation cannot be fully confirmed. It is entirely possible that the saturation trend for 118 μm, just as with 61 μm, is due mostly to lattice heating. If 200 μm does not heat as effectively as the other two THz wavelengths, then PL quenching saturation will not be observed. It is not clear if this process is the only thing limiting our ability to quench the 1s emission.

Figure 4.22 shows the same data in Fig. 4.21 grouped not by τ_{FEL} but by λ_{FEL}. We can clearly see in Fig. 4.22(a) that very little saturation is actually occurring for $\lambda_{\mathrm{FEL}} = 200\,\mu$m. As noted, for the shorter THz wavelengths, quench saturation is seen, possibly due to lattice heating: as the system temperature increases, the PL intensity drops, as seen in Fig 4.7. However, it was not immediately apparent in Fig. 4.21 that at short pump-quench delay times, that the differential quench does not level off. Indeed, looking at Fig. 4.22(c), the 61 μm curve for τ_{FEL} = 58 ps shows a markedly different behavior at fields above 1 kV/cm than it does at larger values of τ_{FEL}.

To account for this dependence on the pump-quench time delay, we turn to how the actual THz field strengths were calculated. Using values obtained from Palik [140], we found the indices of refraction for GaAs and InAs for the relevant THz wavelengths at 5 K. These values, in conjunction with the average power, pulsewidth, and spot size, could be inserted into the Fresnel equations to determine the electric field strength in the wells. Not included in this calculation was electron-hole screening due to the Ti:Sa-photogenerated carriers. The rather high carrier densities that we utilized could be substantially altering the strength of the effective electric field in the Ti:Sa excitation area (see, e.g., Fig. 4.6). Just after the Ti:Sa excitation pulse (low values of τ_{FEL}), the effective electric field in the

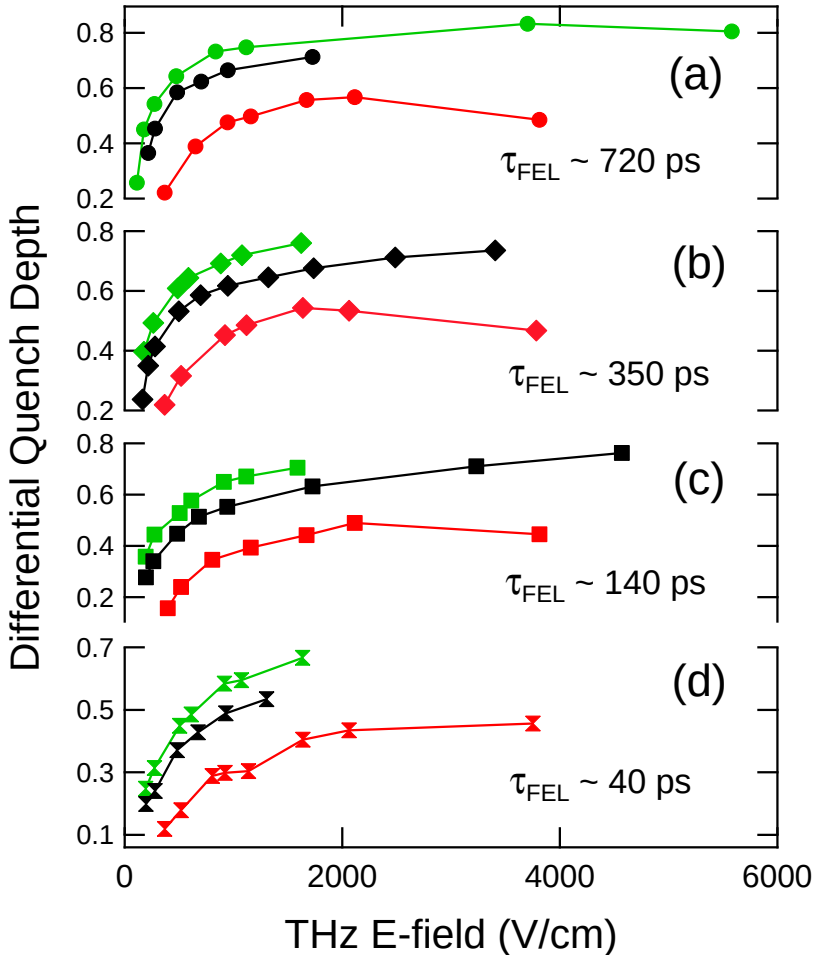

Figure 4.21 : Maximum differential quench depth versus electric field for THz wavelengths of 200 μm (black), 118 μm (green), and 61 μm (red). The pump-quench delay time is different in each subfigure: τ_{FEL} = (a) 720 ps (b) 350 ps (c) 140 ps (d) 40 ps.

quantum wells could be much lower than what we are reporting due to high amount of screening due to the metallic-like electron-hole plasma. As τ_{FEL} increases, the system becomes more insulating (excitonic), which allows for a greater penetration of the electric field.

Looking at Fig. 4.22 again, we can see that each of the curves corresponding to small values of τ_{FEL} are shifted to the right of the larger pump-quench time delay curves, which

fits well with our qualitative understanding: the lack of electric field penetration at short pump-quench time delays effectively over-estimates the THz field in the wells, which corresponds to a rightward shift of the PL quenching curve. Since we lack evidence of the change in the index of refraction at $\lambda_{Ti:Sa}$ = 850 nm, we can only speculate on how well these curves collapse onto one another. A 850 nm pump-THz probe experiment would be able to give us some quantitative estimate about this change.

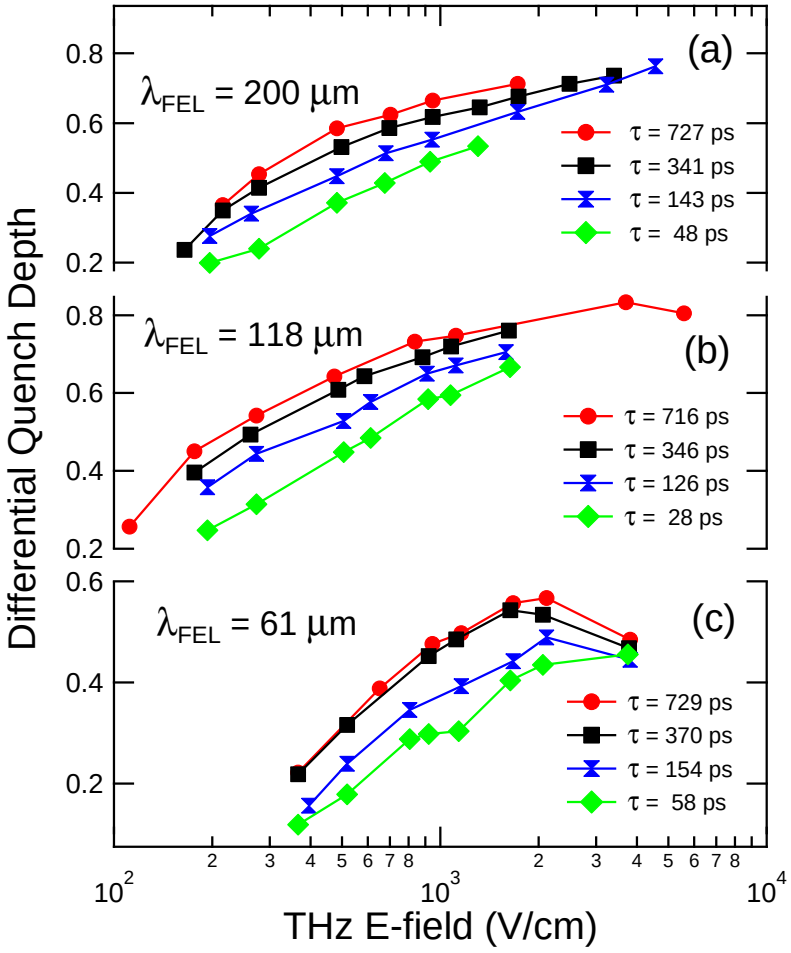

Figure 4.22 : Maximum differential PL quenching data versus electric field grouped by THz wavelength for each pump-quench time delay investigated: (a) 200 μm, (b) 118 μm, and (c) 61 μm.

One other interesting aspect of the data in Figs. 4.21 and 4.22 is that the differential quench becomes larger as the THz wavelength is increased. It is clear, for instance, that there is a substantial difference in Fig. 4.22(b) and (c): at 1 kV/cm, 61 μm THz radiation yields a maximum differential quench of $\sim$0.4, while 118 μm creates a $\sim$0.6 differential quench. Indeed, as seen in Fig. 4.21, the resonant wavelength (118 μm) produces a larger differential quench at a given field strength regardless of the time delay. If we assume that our basic quenching mechanism is a transfer of the bright excitons to some dark level, it makes sense that when the transition probability to the $2p$ state (dark) is maximized (i.e., on-resonance), that the differential quench is largest. If we take a constant THz wavelength at a fixed field strength and simply change the pump-quench delay time, we should see a difference in the quenching behavior if we believe the argument that effective THz field in the quantum wells changes as the system goes from the electron-hole plasma-like state to the excitonic state.

To test this hypothesis, we performed a sweep of the pump-quench delay time while holding the THz field constant; the data are presented in Fig. 4.23. To account for differences in the THz electric field, we normalized the maximum differential quench by the field strength and plotted this quantity up versus pump-quench time delay. The results are surprising: despite being off-resonance, the 200 μm THz wavelength seems to quench the system more effectively than the on-resonance 118 μm wavelength. This observation strongly suggests that the non-resonant quenching mechanism is very important. Further, we can also surmise from Fig. 4.23 that the quenching efficacy generally becomes stronger as the THz wavelength increases. A similar trend was seen in the early time-integrated far-infrared studies of quenching [130, 131].

However, the THz characteristics at 118 μm used to take the data for Fig. 4.23 were different than used for Figs. 4.21 and 4.22. As indicated in Table 4.1, the pulsewidth

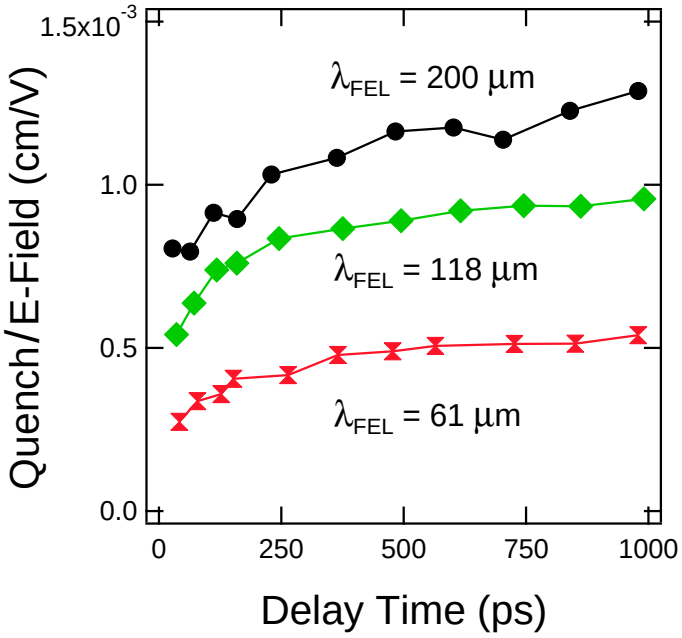

Figure 4.23 : Differential quench normalized by E-field for all THz wavelength investigated as a function of pump-quench delay time.

changed by nearly a factor of three from 31.45 ps (used for Figs. 4.21 and 4.22) to 11.93 ps (Fig. 4.23). Looking at the data shown in Fig. 4.21, it would appear that if we normalized that data to the applied electric field, the 118 μm data would be *higher* than the 200 μm points. As such, it is unclear whether or not the ordering of the far-infrared normalized quench curves seen in Fig. 4.23 is correct. Nevertheless, it is still interesting that the on-resonant and off-resonant PL quenching responses to far-infrared radiation are very similar. Moreover, if we could go fully off-resonance (that is, no coupling to a real state), it would be fascinating to see how the quenching would be affected in that case.

Figure 4.23 confirms the general trend that quenching becomes stronger as the system moves to a more excitonic state. Not only does the electric field penetrate the sample more effectively as τ_{FEL} increases, but the system also simply has a greater percentage of excitons than it does at early times. We feel confident that the differential PL trend with

pump-quench delay time is robust, and that it reflects the exciton formation dynamics of the system. Changing the Ti:Sa excitation fluence and performing the same τ_{FEL} sweep would confirm how dependent the rise seen in Fig. 4.23 is on formation dynamics. Indeed, as the carrier density decreases, we would expect that the slope of the normalized quench versus τ_{FEL} curve to become steeper (faster exciton formation). Executing a 850 nm pump-THz probe experiment, which would most likely couple the THz radiation with the $1s$-$2p$ transition (much in the same manner as Kaindl *et al.* [117]), would also provide a powerful insight into the exciton (both dark and bright) formation process.

4.6 Conclusion

In conclusion, we have shown experimentally and theoretically that intense THz radiation can be used to efficiently excite excitons into higher energy states. TRPL measurements of optically pumped quantum wells show that, after a resonantly tuned THz pulse is introduced, enhanced $2s$ exciton emission is observed. We theoretically show that this observation is due to diffusive Coulomb scattering between the $2p$ and $2s$ exciton states. These results not only highlight pronounced differences between excitons and atoms but also open up new possibilities to manipulate exciton populations using THz pulses [134].

TRPL quenching was studied as a function of THz wavelength, THz field strength, and pump-quench delay time. As the THz wavelength was increased, the population of quenched excitons ($\Delta I/I$) also increased, but there remains some ambiguity as to whether or not the $\lambda_{FEL} = 118$ μm or 200 μm THz wavelength created a larger quench. For all THz wavelengths, a saturation behavior of the quenched exciton fraction was observed as the THz field became larger. For the 61 μm THz wavelength, heating was a problem at higher fluences, making inferences about saturation behavior difficult. A clear pump-quench time delay trend was seen for all the THz wavelengths: when the system was more

plasma-like (electron-hole plasma), the quenching was less prominent; at longer pump-quench delay times, the system was more excitonic (insulator) and the quench became larger. Using a smaller linewidth sample and more THz quenching wavelengths, we believe that the distinction between the resonant and non-resonant quenching mechanisms could be observed utilizing a similar set of tests as these. The strong set of data that we have presented here provides a road map for future TRPL quenching experiments.

Chapter 5

Mid-Infrared Light Induced Non-Perturbative Band Structure Changes in Semiconductors

Matter placed in an intense laser field can sometimes exhibit highly non-perturbative effects that have fascinated researchers for many years. For example, when intense AC electric fields resonantly couple to states in atomic systems, they produce "dressed" states, leading to the emergence of Rabi oscillations, AC Stark effect, Autler-Townes splitting, gain without inversion [141], and electromagnetically-induced transparency [142]. On the other hand, if the frequency of these fields is tuned so that it is far from resonance, researchers have observed striking behaviors, such as above-threshold ionization and high-harmonic generation, where both photon-like and field-like aspects of light play a role.

When intense fields couple to condensed matter systems, semiconductors in particular, a physically rich alternatives to simple atomic systems is created: because of the semiconductor periodic lattice potential, there exists a complex and interesting interplay between the spatially periodic potential of the lattice and the temporally-periodic potential of the intense laser field. If the frequency of the laser field, Ω, is in the mid-infrared range (10–100 THz), photogenerated carriers will not be created in semiconductors; instead, the intense laser field will coherently modify the band structure, leading to effects such as dynamic localization [143] and induced-transparencies [144]. Furthermore, when spatial confinement is considered, interesting quantum mechanical dynamics are predicted to occur, such as coherent destruction of tunneling [145], collapse of minibands [146], and quantum chaos [147]. However, because of the scarcity of high intensity mid-infrared

sources, most of these exotic physical phenomena in solids have not been observed [144].

Recently, a new class of effects has been theoretically predicted for low energy, highly intense electric fields in solids. Using Floquet theory, several researchers have predicted the temporary formation of band gaps at $E = \pm\hbar\Omega/2$ in single layer graphene [148–150], as well as photo-induced topological insulators [151] and quantum spin Hall insulators [152] using intense, circularly-polarized fields. The light-induced, coherent transition from a metal to an insulator is not only dependent on the intensity of the applied field, but also on the polarization of the light: only when the light is circularly polarized does a band gap open in graphene and a topological phase appears in a semiconductor quantum well; linearly polarized light modifies the density of states, but does not induce a temporary phase change.

In this chapter, we propose to use intense, circularly polarized light to create topological changes and to probe the induced changes using low energy THz radiation. To observe this effect, we built a mid-infrared pump, THz probe spectroscopic system that can be easily converted into a variety of other pump-probe configurations. Using intense mid-infrared light from an optical parametric amplifier (OPA) that is tunable from 0.5–20 μm and THz radiation produced by pumping from a chirped-pulse amplifier, we hope to coherently probe the response of graphene and semiconductor quantum wells to high-field pulses. In addition to presenting the major theoretical expectations, we also show data on the OPA pump, CPA laser, and THz detection system. We find that $\sim$2 THz can be generated from our CPA-pumped ZnTe crystal, which is large enough to probe the low energy spectral changes predicted by Calvo *et al.* for graphene [150].

5.1 Induced Band Gaps in Graphene

As an example of theoretically predicted, coherent band structure changes induced by circularly-polarized mid-infrared laser fields, we describe here the case of gap opening in graphene [148–150]. Graphene is a monolayer of graphite created by two inter-weaving triangular sub-lattices of sp^2-bonded carbon atoms [153, 154]. From the calculations by Peierls [155] and Landau [156], it was believed that a purely two-dimensional structure would not be thermodynamically stable enough to exist. Graphene was therefore consigned to a theoretical toy model, starting with Wallace's calculations of the band structure in 1947 [153]. Interest in graphene was re-kindled when carbon nanotubes were identified in 1991 by Iijima [157]. In particular, the band structure of armchair SWCNTs closely follows that of graphene for certain points in the Brillion zone.

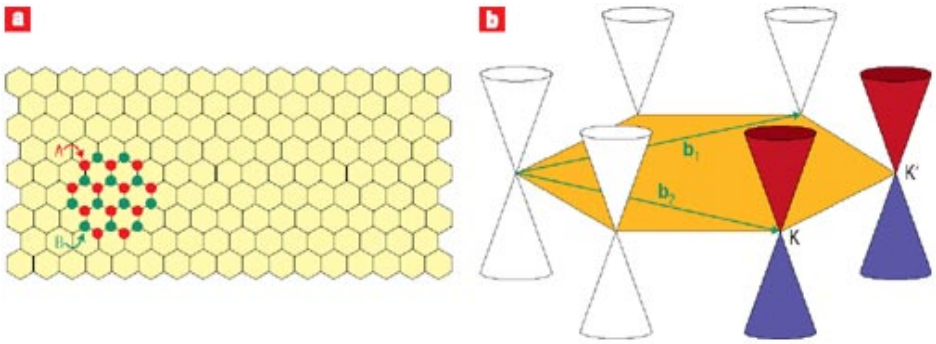

Figure 5.1 : (a) Real space layout of graphene. Red dots show the 'A' sub-lattice, while the green dots indicate the 'B' sub-lattice. (b) At every K and K' point in k-space, the energy versus momentum relationship is linear. This dispersion relation can be seen by the stacked cones drawn at each carbon atom. Figure adapted from [158].

In 2004, however, the discovery that graphene existed independently of graphite created a new paradigm of investigation into atomically thin 2D materials [159]. Graphene has a number of physically and technologically interesting behaviors that make it an outstanding candidate for scientific study. For instance, the carrier mobility can reach upwards of 10^5

cm ^{2}-V^{-1}-s^{-1} at low T and on the order of 10^4 cm ^{2}-V^{-1}-s^{-1} even at room temperature. The observation of the the Quantum Hall Effect in 2005 showed not only the high carrier mobility of graphene, but also highlighted the zero mass nature of Dirac fermions near the Dirac point and electron-hole degeneracy, both effects leading to the observation of the half-integer quantum Hall effect and a non-zero Berry's phase [160]. Optically, the band structure of graphene gives rise to a "universal absorbance" of $\sim$2.3% per layer across a fairly wide range of frequencies. Indeed, as Heinz and co-workers found, the absorption of graphene remained relatively flat at $(1 \pm 0.1) \times \pi\alpha$ from 0.5 to 1.2 eV, where the fine structure constant, α, is equal to $e^2/\hbar c$ = 2.293% [161, 162].

One of the most startling properties of graphene is that fermionic carriers travel at relativistic speeds [163]. The mass of these "Dirac fermions" is zero, which forces the use of the Dirac equations. The reduced speed of light in graphene is a Fermi velocity, $v_{\mathrm{F}} \approx 10^6$ m/s. The Hamiltonian, $\hat{H}$, of these relativistic quasiparticles can be written as [154]:

$$\hat{H} = \hbar v_{\mathrm{F}} \begin{pmatrix} 0 & k_x - ik_y \\ k_x + ik_y & 0 \end{pmatrix} = \hbar v_{\mathrm{F}} \boldsymbol{\sigma} \cdot \mathbf{k}, \tag{5.1}$$

where k_i is the quasiparticle momentum in a given direction and σ is the Pauli matrix. In the presence of an AC electric field, described by a magnetic vector potential A, the Hamiltonian is modified to [150]

$$\hat{H} = v_{\mathrm{F}} \boldsymbol{\sigma} \left[\mathbf{p} - e \cdot \mathbf{A}(t) \right]. \tag{5.2}$$

$\mathbf{A}(t)$ is at a frequency of Ω such that $\mathbf{A}(t) = \mathrm{Re}\{\mathbf{A}_0 \exp(-i\Omega t)\}$, where $\mathbf{A}_0 = A_0 (1, \exp[i\varphi])$ incorporates the intensity (A_0) and polarization (φ). Calvo *et al.* solved Eq. (5.2) using Floquet theory, which brings the solution of the problem into the space created by the direct produce of the Hilbert space and the time-space ($2\pi/\Omega$, where Ω is the AC field angular frequency). Floquet states are temporal analogs of Bloch states. In the latter case, spatial

periodicity creates momentum conservation such that:

$$\psi(\mathrm{r}+\mathrm{R}) = \exp(i\mathrm{k}\cdot\mathrm{R})\,\psi(\mathrm{r}), \tag{5.3}$$

where $\psi(\mathrm{r})$ is a solution to the Schrödinger equation, r is a vector to some point on the crystal, and R is a Bravais lattice vector [80]. Floquet states, on the other hand, are derived from the temporal periodicity of the optical field. In a similar manner to the Bloch construction, their solutions can be stated as [151, 152]:

$$\phi(p,t) = \exp(i\Omega T)\phi(p,t+T), \tag{5.4}$$

where p is momentum, $T = 2\pi/\Omega$, and ϕ is a solution to the time-dependent Schrödinger equation. The application of the AC field at Ω shifts the Floquet quasi-energies by $n\Omega$, where n is an integer, and the phase of the wavefunction, ψ [152]

$$\begin{aligned} E_\alpha(p) &= \frac{\Omega}{2} + \alpha\lambda \\ \phi_\alpha(p,t) &= \frac{1}{\sqrt{2\lambda}} \begin{pmatrix} \sqrt{\lambda + \alpha(v_\mathrm{F}p - \Omega/2)} \\ \alpha\exp(i\Omega t)\sqrt{\lambda - \alpha(v_\mathrm{F}p - \Omega/2)} \end{pmatrix} \end{aligned} \tag{5.5}$$

Here, $\alpha = \pm 1$, $\lambda = \sqrt{g^2 + (v_\mathrm{F}p - \Omega/2)^2}$, and g is the size of the gap at $p = \Omega/2v_\mathrm{F}$. In the mid-infrared range (5–10 μm) and at elevated peak intensities (between 10 and 150 mW/μm^2), the band structure of graphene is radically changed from the unperturbed situation: large, dynamical alterations are seen in the DOS with large peaks and valleys forming. As the polarization of the mid-infrared light is changed from linear to circular, dynamical band gaps open up around $E = \pm\hbar\Omega/2$ and $E = 0$ [150–152, 164].

Figure 5.2 shows the calculated changes in the band structure of graphene at two fluences as compared to the unperturbed band structure. When the mid-infrared field is linearly polarized, a gap is not opened at E = 0, but rather, the DOS rises from E = 0 with

a larger slope than the unperturbed case. Interestingly, strong peaks in the DOS form at energies away from the $E = 0$. At values around $\hbar\Omega/2$ (70 meV for Fig. 5.2), the DOS of states goes abruptly to zero, indicative of one-photon processes [152]. The differences between the low fluence case (solid black line) and the high fluence one (red dashed line) show that the value of A_0 strongly alters the observed effects: not only are the changes in the DOS peak positions different, but also the shape of the DOS spectrum differs.

As the polarization goes from linear to circular, a significant gap opens up around both $E = 0$ and $\pm\hbar\Omega/2$. These two "desert" regions of the DOS spectrum become wider as the fluence increases. Oka and Aoki [148] find that gaps open up at all integer values of $\pm\hbar\Omega/2$. However, it is theorized that the largest effects are seen at $\pm\hbar\Omega/2$ where p is resonant. In the circularly polarized case around these energy values, an increase of a factor of ten in fluence from 32 to 130 mW/μm^2 produces an order of magnitude increase in the band gap. From Calvo and co-workers' paper, we can write down an analytical expression for the induced gap, Δ_k [150]:

$$\Delta_p \simeq eA_0 v_{\mathrm{F}} \sqrt{1 - \cos(\varphi)\sin(2\alpha)}, \tag{5.6}$$

where $\alpha = \tan^{-1}(k_y/k_x)$. From this equation, we see that $\Delta \propto A_0$, showing that the induced band gap is proportional to the fluence. The polarization dependence is slightly weaker than the intensity dependence, but it is notably interesting that in the linear case, no optically-induced band gaps are possible, whereas in the circularly polarized case, they can be observed once $eA_0 v_{\mathrm{F}}$ is larger than $k_{\mathrm{B}}T$.

The change in the DOS caused by the intense mid-infrared field can be probed using typical conductance-type measurement, since the conductance, G, is proportional to the DOS. Since the induced DOS alterations are only present during the intense field, the observed change in the conductivity will be reduced by a factor of $\frac{\tau_p}{T}$, where $T = 1/R_p$ is the spacing between pulses and τ_p is the pulsewidth. To achieve the high pulse intensities

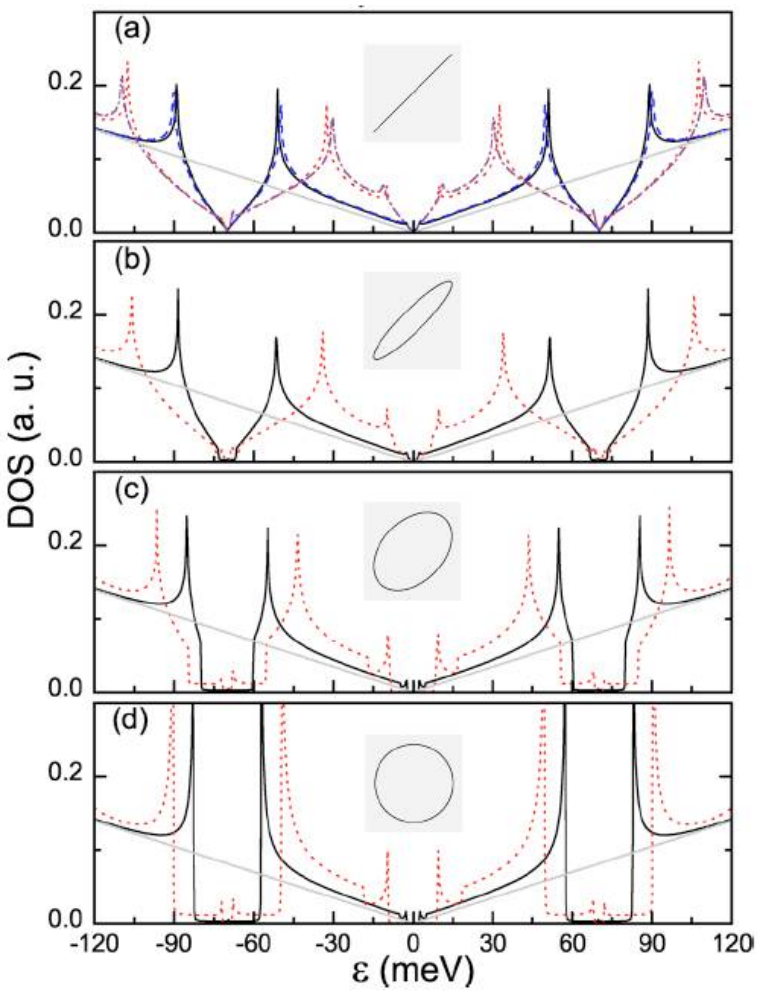

Figure 5.2 : DOS for a single layer of graphene under different fluence and polarization conditions. For all cases considered, the frequency of the pump laser (Ω) is set to 140 meV, with the electric field applied perpendicularly to the monolayer. The black solid line is when the pump intensity is 32 mW/μm^2; for the red dashed line, $I = 130\ mW/\mu$m^2. The gray line is the unperturbed graphene DOS. (a) DOS of states when the pump laser is linearly polarized ($\varphi = 0$). For this case only, the results (black and red lines) are compared with a tight-binding calculation with 5×10^4 channels (I = 32 mW/μm^2 blue dashed line, I = 130 mW/μm^2 purple dashed line). The DOS of states is plotted for three other polarization conditions: (b) $\varphi = 0.125\pi$ (c) $\varphi = 0.375\pi$ and (d) $\varphi = \pi/2$ (circular). Figure adapted from [150].

necessary to produce the changes in the DOS, though, τ_p must be small: a typical figure of merit for femtosecond OPA would be on the order of 10^{-13} seconds. T is on the order of 10^{-3} seconds for an amplified laser and 10^{-7} seconds for an oscillator. In either case, the reduction of the induced DOS (or conductance) would be several orders of magnitude.

To avoid this loss of dynamic range, we plan to use pulsed THz radiation to coherently probe the induced conductivity change in graphene. Since the pulses of the THz radiation and those of the mid-infrared pump can be exactly synchronized, no loss in the signal will be seen. Our system currently has a bandwidth of 1.5–2 THz (or 6–8 meV) covering some of the most interesting DOS changes around the Dirac point (see Fig. 5.2).

A key consideration of choosing the pump frequency is the dephasing time of the Fermions, τ. This coherence time is set by how pure or "clean" the sample is, since lattice disorder and impurities will decrease τ. For this experiment, $\Omega\tau \gg 1$, which basically says that with the time span of one wavelength, the electron (hole) must have the same phase. We can actually see the necessity of this condition by considering that the Floquet condition, given in Eq. (5.4), must be stable over a time $1/\Omega$. Since $\tau \approx 10^{-12}$ s, that means $\Omega > 10^{12}$ rad/s, which excludes the far-infrared frequency range. Thus, we chose the mid-infrared regime as the appropriate frequency region to pump the sample.

Not only does the frequency need to be correct, but as evidenced by Fig. 5.2, high intensities must also be utilized. If we take our pump spot size at the sample to be 1 cm in diameter, and if we examine Fig. 5.4 at 9 μm, we see that a peak intensity of 30 mW/μm^2 is readily achievable (in this calculation, we used a pulsewidth of 400 fs, which is standard for our system). It is unclear, however, if peak intensities approaching 100 mW/μm^2 can be accessed without substantially reducing the spot size. Fortunately, the high signal-to-noise ratios of coherent THz detection allows any change in the band structure to be readily observed, so even peak intensities on the order of 10 mW/μm^2 should still pro-

duce detectable conductance changes. Given these experimental parameters, it seems that the main hindrance to observing this effect will be whether or not a sufficiently pure (and large) single-layer graphene sample can be obtained.

5.2 Terahertz Generation and Detection

Traditional time-domain THz spectroscopy (TDTS) is a two-beam pump-probe setup whereby the pump generates THz and the probe measures it. THz was first generated in $LiTaO_3$ using femtosecond long laser pulses to create a far-infrared conical shock wave [165, 166]. This propagating single-cycle wave could be coherently detected by using a second femtosecond laser pulse irradiating a gap between two electrodes (see Fig. 5.3). The illumination of the gap created carriers, which under a bias field (in this case, the generated THz) would accelerate the photo-generated carriers to one electrode or the other. Since the positive and negative electric field values give different signals, this technique produces a transcription of the THz electric field, unlike a typical detector which only measures intensity ($\propto E^2$).

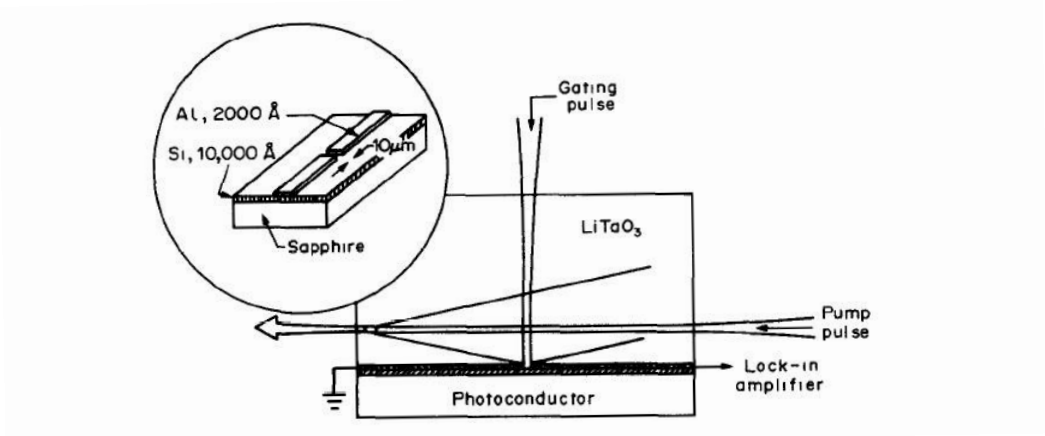

Figure 5.3 : First demonstration of coherent THz creation and detection (adapted from [166]).

In the years since the first THz experiments, several other methods have been used to generate and detect coherent THz waves. Importantly, unlike the early work done using non-linear crystals and transmission line propagation, the ability to create THz waves that freely propagate in air was a major advancement [167, 168]. One of the most widely used techniques for free space THz generation is using difference frequency generation (DFG). In a DFG process, the non-linear polarization, P_{NL}, is created by the mixing of two different fields, $E(\omega_1)$ and $E(\omega_2)$, where ω_{i} is the angular frequency of the field. The wave equation is given by [169]:

$$\begin{aligned} \left(\nabla\times\nabla-\omega\varepsilon(\omega)/c^2\right)E(\omega) &= \tfrac{4\pi\omega^2}{c^2}P_{\mathrm{NL}}(\omega), \\ P_{\mathrm{NL}}(\omega) &\cong \chi^{(2)}E(\omega_1)E^*(\omega_2), \end{aligned} \tag{5.7}$$

where $\omega=\omega_1-\omega_2$ and $\chi^{(2)}$ is the second-order tensor describing the susceptibility. Far-infared radiation from a DFG process was experimentally first observed by Zernike and Berman [170] and theoretically developed by Shen [171] (for a good review of the early history of DFG-created far-infrared radiation, see [169]).

For the broadband THz generation used in our setup, the frequency components, ω_1 and ω_2, come from the Fourier components making up an ultrafast laser pulse. A non-linear crystal without inversion symmetry, such as ZnTe, but also GaP, DAST [172, 173] and GaSe [174], is then used for the DFG process. The large temporal photon densities in the pulse itself are enough to produce a photogenerated polarization at the difference frequency that is equal to the second-order time derivative [175]:

$$E_{\mathrm{THz}}(t)=\frac{\partial^2}{\partial t^2}\left[\chi^{(2)}E_{\mathrm{opt}}(\omega_1)E_{\mathrm{opt}}(\omega_2)\right], \tag{5.8}$$

where E_{THz} is the THz field and E_{opt} is the optical excitation field. This process, often termed optical rectification when $\omega=\omega_1-\omega_2\approx 0$, was first demonstrated by Bass *et al.* [176].

Although coherent generation of far-infrared fields was done several decades ago, years of research were necessary to obtain coherent detection of THz fields. One of the most widely used techniques for the THz radiation detection is electro-optic (EO) sampling. This method uses the Pockels effect in the THz regime to effectively "map" out the field. In the Pockels effect, the birefringence of a solid is proportionally changed by an applied electric field that is slowly varying as compared to the transmitted light [177]. The basic idea is that the THz wave that one is trying to detect is the applied electric field. When an optical probe beam passes through a non-centrosymmetric crystal with a low group velocity mismatch (GVM), such as ZnTe, its polarization is changed by the slowly-varying, coincident THz field. The magnitude and direction of the induced polarization change is proportional to the THz field. If the optical probe beam has pulsewidth very much shorter than the THz pulsewidth, then one can sample the polarization change (THz field) by sweeping the optical probe-THz pulse time delay.

A more quantitative approach to EO sampling can help provide more insight into this process. Taking $\langle 100 \rangle$-cut ZnTe as our EO sampling crystal, we can define the induced polarization change, Γ, as [178]:

$$\Gamma = \frac{\pi d n^3 \gamma_{41}}{\lambda_{\text{gate}}} E_{\text{THz}}, \tag{5.9}$$

where d is the thickness of the ZnTe crystal, n is the refractive index for ZnTe at the optical probe frequency, γ_{41} is the EO coefficiency, E_{THz} is the THz field, and λ is the wavelength of the optical probe. For our experiment, d = 1 mm, n = 2.85, γ_{41} = 3.9 pm/V, and $\lambda = 775$ nm. However, what we are actually measuring is not Γ, but $\Delta I = I_y - I_x \simeq I_0 \Gamma$ where I_i is the intensity of transmitted beam in the i^{th} direction and I_0 is the incident intensity. We can

find I_i from using ABCD rotational matrices [178]:

$$\begin{cases} I_x = I_0 \cos^2 \frac{\Gamma_0+\Gamma}{2} \\ I_y = I_0 \sin^2 \frac{\Gamma_0+\Gamma}{2}, \end{cases} \tag{5.10}$$

where Γ_0 is the static phase of the unperturbed system. Typically, Γ_0 is set such that $\Delta I \approx 0$ when no THz field is present. In most cases, $\Gamma \ll 1$, so we get $I_x \simeq \frac{I_0}{2}(1-\Gamma)$ and $I_y \simeq \frac{I_0}{2}(1+\Gamma)$, giving $\Delta I \simeq I_0\Gamma$, as mentioned previously.

Since the optical pulse must sample the THz electric field at a given temporal location, it is important that the speed at which both pulses travel through the crystal is as close as possible. The GVM between the two pulses causes the sampling to smear out the THz wave, since the optical pulse will effectively probe different parts of the THz wave. ZnTe, which we use in the system, has been commonly selected for EO sampling because of its moderately large EO coefficient (γ_{41} = 3.9 pm/V) and its very small GVM between optical and THz frequencies [178].

5.3 Mid-Infrared Pump-Terahertz Probe System

In the experimental setup that we have built, we utilized 1 mm thick $\langle 100 \rangle$-cut ZnTe for both the optical rectification (THz generation) and the EO sampling (THz detection). Of the $\approx$1 W of power generated from the chirped-pulse amplifier (CPA) laser, only 100 mW actually reaches the ZnTe emitter crystal, since 85% of the beam is redirected to the optical parametric amplifier (OPA). Since the gate beam is only needed for detection, we use two pellicle beam splitters to direct the gate beam onto the ZnTe detector crystal. Because of the very small reflection of the pellicle beamsplitters, only $\approx$0.2% of the 100 mW sent to the THz system actually ends up on the detector crystal. To increase the SNR, we use a 5" lens in the gate line just before the detector crystal to focus the gate beam onto the ZnTe

surface.

As mentioned above, the majority of the CPA laser emission ends up going to the OPA. Our OPA is a five-pass system: three passes through the β-barium borate (BBO) non-linear crystal are used to create a "seed beam" at a given wavelength, while the other two passes through the BBO are used to amplify the seed. These amplifying passes distinguish the OPA from its cousin, the optical parametric oscillator (OPO). The signal and idler beams generated by the OPA are a result of the conservation of energy: ≈1.55 eV photons are down converted into two photons of lesser energy. These two beams are the output of any OPA or OPO. However, given the high pulse energies of the signal and idler beams (in our system, a typical measured value is ∼100 uJ), the signal and idler can be sent into yet another non-linear crystal to be either up or down-converted. Since the signal and idler can be tuned from 850 nm to 2800 nm, a variety of second harmonic frequencies ($\omega_2 = 2\omega_1$), sum frequencies ($\omega_3 = \omega_1 + \omega_2$), and difference frequencies ($\omega_3 = \omega_1 - \omega_2$) can be generated, depending on the exterior non-linear crystal used. All told, with our current set of crystals, we are able to create pulsed amplified light from 500 nm to 20 μm. Figure 5.4 shows the measured pulse energy for a variety of set wavelengths from our OPA after being sent through difference frequency generation (DFG) crystals 1 and 2. Special care was taken to use two long pass wavelength filters (constructed from Ge) to avoid measuring stray signal and idler light.

The full system is depicted in Fig. 5.5, with the different beam lines being color-coded so that they are easier to trace by eye. The THz wave generation and detection beam paths constitute their own sub-system: TDTS can be performed on various samples without the pump beam. However, the TDTS setup has two distinct inherent disadvantages. First, it has only a small amount of pulse energy (≈100 uJ) to generate THz fields, and second, the entire system is comparatively far from the CPA, which creates some Poynting vector

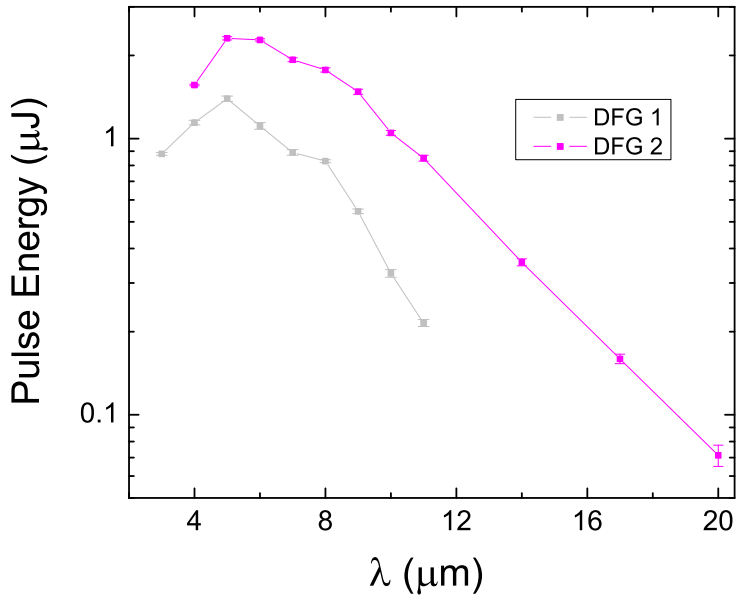

Figure 5.4 : Measured pulse energies across set output wavelength from the OPA using difference frequency generation (DFG) crystals 1 and 2.

instabilities. These two problems are a result of diverting most of the CPA laser emission to the OPA. Indeed, the OPA not only needs high pump powers to generate an output, but the five passes through the BBO inside the OPA create an extra 100" of path length.

Intensity Autocorrelation

The intensity autocorrelation is a $g^{(2)}(\tau)$ measurement that looks at the coherence of the photons in the beam at a given location across a delay time, τ. To begin any discussion of $g^{(2)}(\tau)$, we must first start with the first-order coherence function, $g^{(1)}(x_1,x_2)$ [179],

$$g^{(1)}(x_1,x_2) = \frac{\langle E^*(x_1)E(x_2)\rangle}{\sqrt{\langle|E(x_1)|^2\rangle\langle|E(x_2)|^2\rangle}}. \tag{5.11}$$

If the absolute value of the expectation quantity between the two locations and/or times, x_1 and x_2, is 0, then we say it is incoherent. A value of 1 signifies full first-order coherence, while between 0 and 1 indicates partial coherence. $g^{(1)}(x_1,x_2)$ provides a determination of

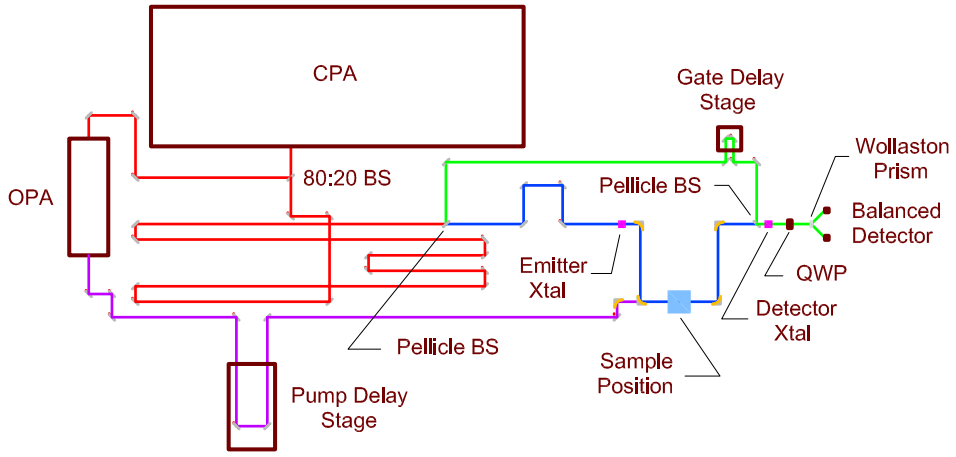

Figure 5.5 : Schematic of the OPA pump-THz probe system. The CPA beam (red) pumps the OPA line (purple), creates THz radiation at the emitter crystal (blue), and acts at the THz gate (green).

the correlations between fields at a given location, but it is often much easier for experimentalists to measure intensities (E^2) rather than electric fields. The second-order coherence function, $g^{(2)}(\tau)$, can be defined as [180]:

$$g^{(2)}(\tau) = \frac{\langle I(t)I(t+\tau)\rangle}{\langle I(t)\rangle^2}, \tag{5.12}$$

where I is the intensity of the field. The most common way to measure $g^{(2)}(\tau)$ is to split two beams apart, one going to a detector (or non-linear crystal) and the other going to a mechanical delay unit before being directed to the same detector. Here, we would take x_i to be a time (since positional overlap is assumed), with a time delay being defined as $\tau = x_1 - x_2$. By scanning the delay unit, one can vary τ between the two beams (or pulses) to obtain $g^{(2)}(\tau)$. In the case of pulsed lasers, the very high peak pulse intensities create very strong second-harmonic generation (SHG) in BBO. When both beams are overlapped in space and time with one another, the pulse intensity is twice as strong, resulting in a SHG beam that is four times that of the self-generated SHG beam.

Figure 5.6(a) shows an intensity autocorrelation (roughly equivalent to $g^{(2)}(\tau)$) plotted

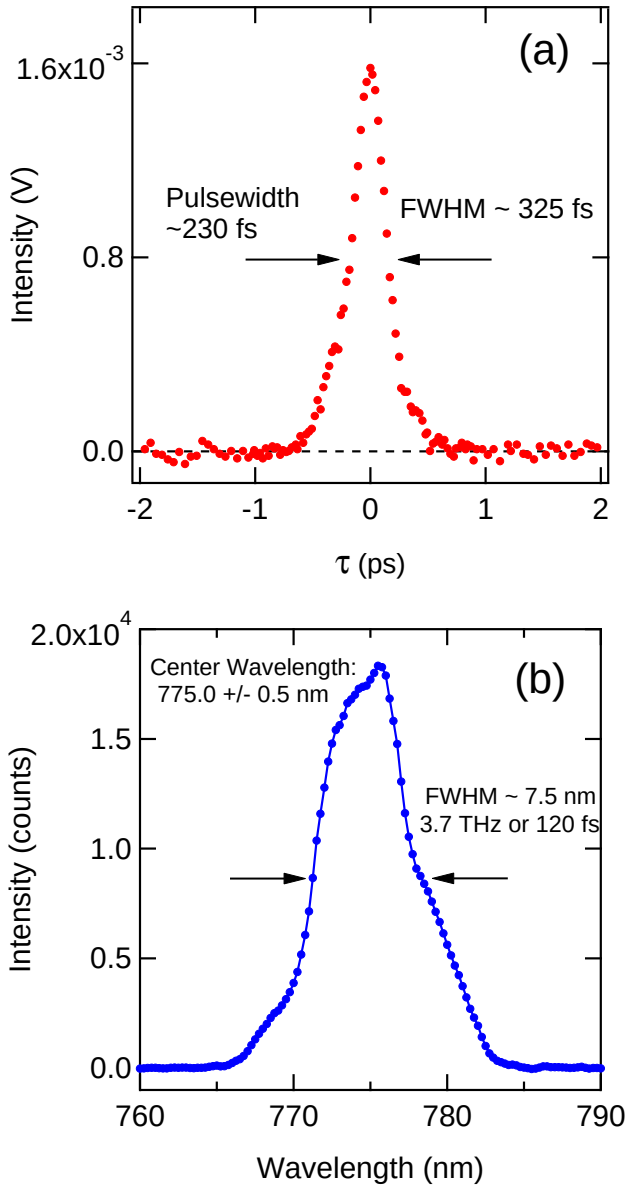

Figure 5.6 : (a) Intensity autocorrelation of CPA beam. The baseline of the trace has been subtracted for clarity. (b) Wavelength power spectrum of CPA beam. The Fourier transform limited bandwidth from the power spectrum gives a narrower pulsewidth than the intensity autocorrelation, suggesting that the CPA pulse is chirped.

versus τ. Since we assume that the shape of the pulse is Gaussian, the measured full-width at half maximum (FWHM) of the trace must be divided by $\sqrt{(2)}$. As is seen in the figure, the measured pulsewidth is $\sim$230 fs or 1.92 THz. However, intensity autocorrelations are not terribly accurate, since they do not reconstruct the pulse (phase information is missing). Typically, we take the pulsewidths from an intensity autocorrelation to be 10–20% accurate. As a secondary measure of the pulsewidth, we can examine the intensity spectrum across wavelength, $I(\lambda)$. In the Fourier transform limit, $\Delta\nu\Delta t \geq 0.441$ for a Gaussian-shaped pulse, where $\Delta\nu$ is a measure of the frequency spread and Δt is the pulsewidth. Using the measured FWHM of $I(\lambda)$ (7.5 nm), we find that Δt is 120 fs or 3.7 THz. This value is substantially different from the one obtained using $g^{(2)}(\tau)$. Since the calculation of $I(\lambda)$ assumed no-chirp or any other contributions to the beam quality, we can take 120 fs as an ideal limit and 230 fs as a slight over-estimate. Therefore, we can estimate that the CPA pump beam will produce a difference frequency generated THz field with a maximum bandwidth of 2–2.5 THz.

5.3.1 Terahertz Field

The gate delay maps out the THz field using the Pockels effect in ZnTe, as previously mentioned. The THz field-induced change in the polarization of the gate beam is discriminated using a Wollaston prism, and the *s* and *p* components that are separated are fed to a balanced detector. When no THz field is present, we adjust the quarter wave plate so as to zero the output of the balanced detector, which can be measured using an oscilloscope. The field-induced polarization change is read by a lock-in amplifier (LIA). A typical trace is given in Fig. 5.7. The oscillations present after the main pulse indicate that we are observing some water vapor absorption, despite the fact that we are continuously purging the THz radiation travel area with N_2. A fast-Fourier transform (with a zero padding of 2^{13})

shows that the THz field spans from 0.1 GHz to 2 THz, which is roughly in accordance with our naïve expectations.

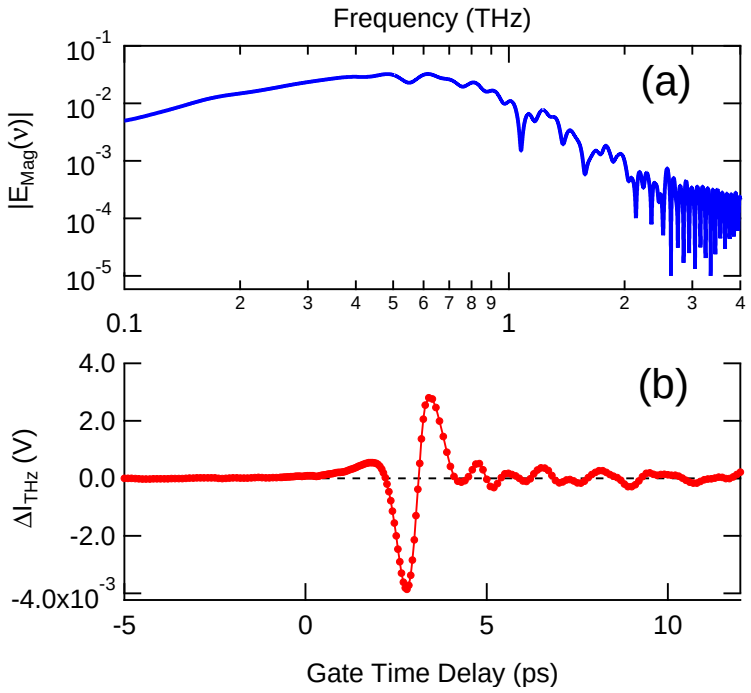

Figure 5.7 : (a) Electric field magnitude as a function of frequency produced from taking an FFT of the measured THz field. The generated bandwidth can be roughly estimated to be from 100 GHz to 2 THz. (b) Measured THz field in an N_2-purged environment using a lock-in amplifier and a balanced detector.

To obtain pump-probe overlap, we used intrinsic GaAs as a testing platform. Intrinsic GaAs has the advantage of being transparent to THz radiation, because it has a minimized free-carrier (Drude) absorption due to its lack of carriers. When free carriers are present, Drude-like absorption increases as λ^2, causing substances with free-carriers to be increasingly opaque in the far-infrared region. Intrinsic GaAs can become transiently populated with free carriers when photons with energies above the band gap of GaAs are incident on the sample. These photogenerated electron-hole pairs cause GaAs to appear "metal-like" during and just after the optical pulse. The optically-created electron-hole population

causes the THz pulse to be absorbed, resulting in a sudden drop of the THz transmittance (or, equivalently, change in the conductivity). This sudden THz transmittance suppression allows one to obtain the pump-probe delay time at which the pump pulse and probe pulse are temporally and spatially overlapped.

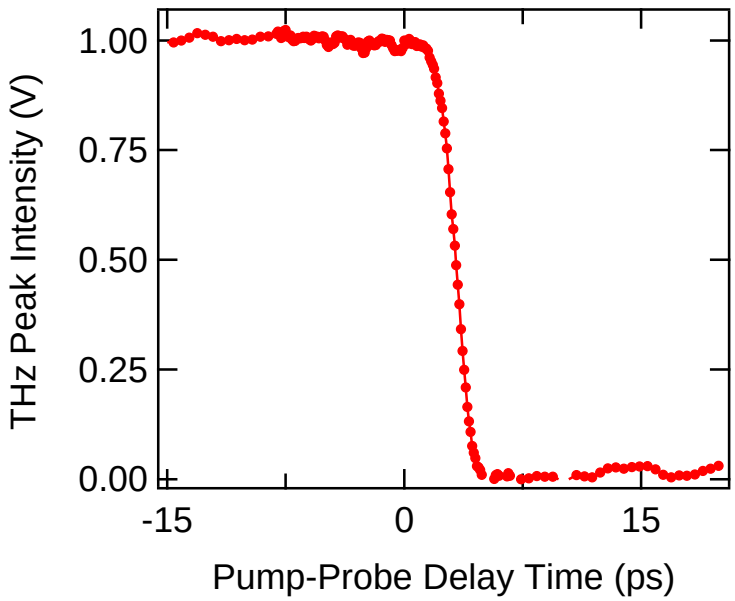

Figure 5.8 : Peak intensity of the transmitted THz field through intrinsic GaAs as a function of pump-probe time delay. The optical pump ($\lambda_{pump} = 775$ nm) produced photogenerated carriers causing the transmittance of the GaAs to fall to nearly zero, as reflected in the sudden drop of the peak field at $\tau \approx 0$ ps.

In Fig. 5.8, we trace the peak intensity of the THz field as a function of the pump-probe delay time. At $\tau_{pump-probe} \approx 0$ ps, the optical pulse begins to completely quench the transmitted THz field, indicating that we are scanning pump-probe pulse overlap. The drop of the THz transmittance is a convolution of the THz pulse (on the order of ps) with the response time of the induced photogenerated carriers (equivalent to 200 fs, which is the duration of the CPA pulse). This convolution accounts for the picosecond-long drop in the THz transmittance seen in Fig. 5.8. Because the photogenerated carrier population

relaxes on the order of nanosecond, had we scanned further in time, we would have seen the THz transmittance recover back to its nominal value as carriers cooled off from optical and acoustic phonon emission and radiative recombination.

5.4 Conclusions and Future Steps

Three major steps are left in the completion of the multi-frequency THz system: one is to modify the purging box apparatus to allow for the inclusion of the pump beam, the second is to convert the detection system to a boxcar integrator, and the third is to perform mid-infrared pump-THz probe spectroscopy on intrinsic Si at low T. The latter is basically a test run for the case of graphene, since Si is a well-characterized material. The first system improvement, the modification of the purge box, is highly necessary given that THz radiation propagation in air shows significant absorption. This effect hinders our experimental observations and interpretation, so creating a water-free environment is very important.

The second material improvement to the overall system is to convert the detection from a LIA to a boxcar integrator. The boxcar integrator takes in pulsed inputs (such as from the balanced detector) and integrates only over the pulse duration. Since every laser pulse is being counted, a two-fold advantage is achieved: a SNR improvement of $\sqrt{N}$ is observed, where N is the number pulses, and pulse-to-pulse fluctuations can be normalized. The normalization of the pulse intensity fluctuations is important, since the observed effect hinges on high peak intensities. Changes in these intensities pulse-to-pulse effectively smear out the induced-DOS alterations that we hope to observe. By measuring not just to the balanced detector signal but also the mid-infrared pump intensity (using a HgCdTe detector) and the THz pump beam (the optical line at the ZnTe emitter), we believe that the pulse-to-pulse fluctuations of both the OPA and CPA can be taken into account.

As mentioned before, this system is highly adaptable. For many projects using the mid-

infrared line, the THz conductivity system, or some combination of both, can be conceived. Moreover, taking out the ZnTe crystal and installing sapphire can convert the system from a THz probe to a whitelight probe, further enhancing the experimental range of this apparatus. The design, implementation, and tentative results presented in this chapter show the development of this multi-frequency THz system.

Chapter 6

Conclusions

In this thesis, we presented three completed projects on low-energy processes in reduced dimensional semiconductors. In the first project, we designed, built, and tested a variable temperature conductivity setup in a 6 T magnet for the study of temperature-dependent magnetoresistance (MR) in an ensemble of single-wall carbon nanotubes (SWCNTs). We performed a slow temperature-dependent resistance scan from 1.3 K to 350 K on the sample in both a non-annealed and annealed condition. For both annealing conditions, we observed a 3D variable-range hopping (VRH) behavior below $\approx$100 K. Further, we extended the temperature range for the annealed sample down to 0.3 K; the 3D VRH behavior continued to be observed down to that temperature. We observed that the characteristic hopping temperature, T_0, rose from 30.9 K to 131 K upon annealing, suggesting that either the density of states at the Fermi energy or the localization length of the electrons (or both) is being decreased by the removal of adsorbates.

We performed MR scans out to 6 T for numerous temperatures between 1.4 K and 250 K for both the non-annealed and annealed sample conditions. For the annealed sample condition, we measured an extremely detailed set of temperature-dependent scans between 20 K and 2 K out to 8 T using a ^{3}He system. We observed a remarkable change in the MR from 25 K to 1.4 K: at temperatures above 25 K, the MR is positive, an effect we have been able to fit using a spin-dependent VRH model; below 25 K, the MR is quadratically negative with field, dropping to -0.04 at 6 K and 8 T, a signature of weak localization. However, as the temperature is further decreased, the MR curve becomes strongly positive

at high fields. Indeed, the MR at 1.4 K rises to 0.16 at 6 T, showing both a sign change in the MR and an order of magnitude increase.

In the second project, we measured the temperature-dependent electron spin resonance (ESR) in SWCNTs both before and after thermal annealing. We found that as the temperature was raised from 3 K to 300 K, the ESR linewidth became motionally narrowed, meaning that the ESR linewidth was narrowed as the temperature was increased. Using a generic motional narrowing formula from Anderson [81,82] and a hopping wavefunction from Wilson [83], the temperature-dependent spin-spin relaxation times could be well-fit [27]. The same motionally-narrowed linewidth behavior is also observed in doped semiconductors at certain doping concentrations, suggesting that bulk SWCNT ESR is related to ESR-active defects. Our observation that the spin susceptibility in SWCNT rises by a factor of four when the sample is annealed and that this effect is due to the presence of molecular oxygen, further suggests that defects are the cause of the ESR signal [27].

The third project utilized intense, narrow-band, far-infrared radiation to interrupt photoluminescence (PL) emission from the $1s$ exciton state in quantum wells. When the terahertz (THz) photon energy was resonant with the $1s$-$2p$ intra-excitonic transition, induced $2s$ luminescence was observed, despite the lack of angular momentum conservation between the excited $2p$ state and the $2s$ state. However, by theoretically considering higher order exciton terms, we found that scattering from the $2p$ to the $2s$ state is allowed, a prediction made several years ago by Kira and Koch [138]. Our work on intra-excitonic scattering due to Coulombic symmetry breaking is the first experimental verification of this theory, and it provides a major distinction between atoms and excitons [134]. Furthermore, we found that the time-resolved $1s$ emission, which was transiently stopped by the THz field, returns after several hundreds of picoseconds, as the exciton population moves from the excited $2p$ state back down to the luminescing $1s$ level. This convincingly shows that we

can store energy using the internal structure of excitons ("excitonic shelving"). The depth and prominence of the 1s PL quench and the recovery of the luminescence both depend on the wavelength of the THz radiation and its field strength.

Lastly, we proposed to study transient, high-field-induced band gap opening in graphene using a mid-infrared pump, THz probe spectroscopy setup. Since this project has only recently begun to take shape, we showed only technical results from the construction of the setup, such as an autocorrelation of the Ti:Sa pump beam, THz wave traces, and schematics of the system.

Bibliography

[1] R. Egger, A. Bachtold, M. S. Fuhrer, M. Bockrath, D. H. Cobden, and P. L. McEuen, "Luttinger liquid behavior in metallic carbon nanotubes," *Lecture Notes in Physics: Interacting Electrons in Nanostructures*, vol. 579, pp. 125–146, 2001.

[2] G. T. Noe, J.-H. Kim, J. Lee, Y. Wang, A. K. Wójcik, S. A. McGill, D. H. Reitze, A. A. Belyanin, and J. Kono, "Giant superfluorescent bursts from a semiconductor magneto-plasma," *Nat. Phys.*, vol. 8, pp. 219–224, 2012.

[3] T. Bartel, P. Gaal, K. Reimann, M. Woerner, and T. Elsaesser, "Generation of single-cycle THz transients with high electric-field amplitudes," *Opt. Lett.*, vol. 30, pp. 2805–2807, 2005.

[4] X. Xie, J. Dai, and X.-C. Zhang, "Coherent control of THz wave generation in ambient air," *Phys. Rev. Lett.*, vol. 96, p. 075005, 2006.

[5] X. Xie, J. Xu, J. Dai, and X.-C. Zhang, "Enhancement of terahertz wave generation from laser induced plasma," *Appl. Phys. Lett.*, vol. 90, p. 141104, 2007.

[6] K.-Y. Kim, J. H. Glownia, A. J. Taylor, and G. Rodriguez, "Terahertz emission from ultrafast ionizing air in symmetry-broken laser fields," *Opt. Exp.*, vol. 15, pp. 4577–4584, 2007.

[7] J. Hebling, K.-L. Yeh, M. C. Hoffmann, and K. A. Nelson, "High-power THz generation, THz nonlinear optics, and THz nonlinear spectroscopy," *IEEE J. Selected*

Topics in Quantum Electronics, vol. 14, p. 345, 2008.

[8] A. Sell, A. Leitenstorfer, and R. Huber, "Phase-locked generation and field-resolved detection of widely tunable terahertz pulses with amplitudes exceeding 100 MV/cm," *Optics Lett.*, vol. 33, p. 2767, 2008.

[9] M. Nagai, M. Jewariya, Y. Ichikawa, H. Ohtake, T. Sugiura, Y. Uehara, and K. Tanaka, "Broadband and high power terahertz pulse generation beyond excitation bandwidth limitation via $\chi^{(2)}$ cascaded processes in $LiNbO_3$," *Opt. Express*, vol. 17, pp. 11543–11549, 2009.

[10] J.-C. Charlier, X. Blase, and S. Roche, "Electronic and transport properties of nanotubes," *Rev. Mod. Phys.*, vol. 79, pp. 677–732, 2007.

[11] P. Avouris, "Carbon nanotube electronics," *Chem. Phys.*, vol. 281, pp. 429–445, 2002.

[12] J.-Y. Park, S. Rosenblatt, Y. Yaish, V. Sazonova, H. Üstünel, S. Braig, T. A. Arias, P. W. Brouwer, and P. L. McEuen, "Electron-phonon scattering in metallic single-walled carbon nanotubes," *Nano Lett.*, vol. 4, pp. 517–520, 2004.

[13] Z. Yao, C. L. Kane, and C. Dekker, "High-field electrical transport in single-wall carbon nanotubes," *Phys. Rev. Lett.*, vol. 84, pp. 2941–2944, 2000.

[14] P. G. Collins, K. Bradley, M. Ishigami, and A. Zettl, "Extreme oxygen sensitivity of electronic properties of carbon nanotubes," *Science*, vol. 287, pp. 1801–1804, 2000.

[15] A. Goldoni, R. Larciprete, L. Petaccia, and S. Lizzit, "Single-wall carbon nanotube interaction with gases: Sample contaminants and environmental monitoring," *J. Am. Chem. Soc.*, vol. 125, pp. 11329–11333, 2003.

[16] X. Cui, M. Freitag, R. Martel, L. Brus, and P. Avouris, "Controlling energy-level alignments at carbon nanotube/Au contacts," *Nano Lett.*, vol. 3, pp. 783–787, 2003.

[17] G. Baumgartner, M. Carrard, L. Zuppiroli, W. Bacsa, W. A. de Heer, and L. Forró, "Hall effect and magnetoresistance of carbon nanotube films," *Phys. Rev. B*, vol. 55, pp. 6704–6707, 1997.

[18] G. T. Kim, E. S. Choi, D. C. Kim, D. S. Suh, Y. W. Park, K. Liu, G. Duesberg, and S. Roth, "Magnetoresistance of an entangled single-wall carbon-nanotube network," *Phys. Rev. B*, vol. 58, pp. 16064–16069, 1998.

[19] J. Z. Cai, L. Lu, W. J. Kong, H. W. Zhu, C. Zhang, B. Q. Wei, D. H. Wu, and F. Liu, "Pressure-induced transition in magnetoresistance of single-walled carbon nanotubes," *Phys. Rev. Lett.*, vol. 97, p. 026402, 2006.

[20] K. Yanagi, Y. Miyata, and H. Kataura, "Optical and conductive characteristics of metallic single-wall carbon nanotubes with three basic colors; cyan, magenta, and yellow," *Appl. Phys. Exp.*, vol. 1, p. 034003, 2008.

[21] N. Mott, *Conduction in Non-Crystalline Materials*. New York, NY USA: Oxford University Press, 2nd ed., 1993.

[22] B. I. Shklovskii and A. L. Efros, *Electronic Properties of Doped Semiconductors*, vol. 45 of *Solid-State Sciences*. Berlin: Springer-Verlag, 1979.

[23] A. Miller and E. Abrahams, "Impurity conduction at low concentrations," *Phys. Rev.*, vol. 120, pp. 745–755, 1960.

[24] H. Kamimura and H. Aoki, *The Physics of Interacting Electrons in Disordered Systems*. New York, NY USA: Clarendon Press, 1989.

[25] P. Nikolaev, O. Gorelik, R. Allada, E. Sosa, S. Arepalli, and L. Yowell, "Soft-bake purification of single-walled carbon nanotubes produced by pulsed laser vaporization," *J. Phys. Chem. C*, vol. 111, pp. 17678–17683, 2007.

[26] W. D. Rice, R. T. Weber, S. Nanot, P. Nikolaev, S. Arepalli, A.-L. Tsai, and J. Kono, "Motional narrowing of electron spin resonance in single-walled carbon nanotubes," *arXiv*, vol. 1105.5095v2, 2011.

[27] W. D. Rice, R. T. Weber, A. D. Leonard, J. M. Tour, P. Nikolaev, S. Arepalli, V. Burka, A.-L. Tsai, and J. Kono, "Enhancement of the electron spin resonance of single-walled carbon nanotubes by oxygen removal," *ACS Nano*, vol. 6, pp. 2165–2173, 2012.

[28] W. Yi, L. Lu, Z. Dian-lin, Z. W. Pan, and S. S. Xie, "Linear specific heat of carbon nanotubes," *Phys. Rev. B*, vol. 59, p. R9015, 1999.

[29] M. Jaiswal, W. Wang, K. A. S. Fernando, Y.-P. Sun, and R. Menon, "Magnetotransport in transparent single-wall carbon nanotube networks," *Phys. Rev. B*, vol. 76, p. 113401, 2007.

[30] J. Vavro, J. M. Kikkawa, and J. E. Fischer, "Metal-insulator transition in doped single-wall carbon nanotubes," *Phys. Rev. B*, vol. 71, p. 155410, 2005.

[31] A. Kurobe and H. Kamimura, "Correlation effects on variable range hopping conduction and the magnetoresistance," *J. Phys. Soc. Japan*, vol. 51, pp. 1904–1913, 1982.

[32] A. Frydman and Z. Ovadyahu, "Spin and quantum interference effects in hopping conductivity," *Sol. State Comm.*, vol. 94, pp. 745–749, 1995.

[33] Q. Si, "Spin conductivity and spin-charge separation in the high-T_c cuprates," *Phys. Rev. Lett.*, vol. 78, pp. 1767–1770, 1997.

[34] Q. Si, "Spin injection into a Luttinger liquid," *Phys. Rev. Lett.*, vol. 81, pp. 3191–3194, 1998.

[35] L. Balents and R. Egger, "Spin transport in interacting quantum wires and carbon nanotubes," *Phys. Rev. Lett.*, vol. 85, pp. 3464–3467, 2000.

[36] L. Balents and R. Egger, "Spin-dependent transport in a Luttinger liquid," *Phys. Rev. B*, vol. 64, p. 035310, 2001.

[37] A. A. Kiselev and K. W. Kim, "Progressive suppression of spin relaxation in two-dimensional channels of finite width," *Phys. Rev. B*, vol. 61, pp. 13115–13120, 2000.

[38] S. Rabello and Q. Si, "Spectral functions in a magnetic field as a probe of spin-charge separation in a Luttinger liquid," *Europhys. Lett.*, vol. 60, p. 882, 2002.

[39] A. D. Martino, R. Egger, K. Hallberg, and C. A. Balseiro, "Spin-orbit coupling and electron spin resonance theory for carbon nanotubes," *Phys. Rev. Lett.*, vol. 88, p. 206402, 2002.

[40] B. Dóra, M. Gulácsi, J. Koltai, V. Zólyomi, J. Kürti, and F. Simon, "Electron spin resonance signal of Luttinger liquids and single-wall carbon nanotubes," *Phys. Rev. Lett.*, vol. 101, p. 106408, 2008.

[41] D. P. DiVincenzo, "Quantum computation," *Science*, vol. 270, p. 255, 1995.

[42] S. A. Wolf, D. D. Awschalom, R. A. Buhrman, J. M. Daughton, S. von Molnar, M. L. Roukes, A. Y. Chtchelkanova, and D. M. Treger, "Spintronics: A spin-based electronics vision for the future," *Science*, vol. 294, pp. 1488–1495, 2001.

[43] T. Giamarchi, *Quantum Physics in One Dimension*. Oxford: Oxford University Press, 2004.

[44] T. Ando, "Spin-orbit interaction in carbon nanotubes," *J. Phys. Soc. of Japan*, vol. 69, pp. 1757–1763, 2000.

[45] M. Kosaka, T. W. Ebbesen, H. Hiura, and K. Tanigaki, "Electron spin resonance of carbon nanotubes," *Chem. Phys. Lett.*, vol. 225, pp. 161–164, 1994.

[46] M. Kosaka, T. W. Ebbesen, H. Hiura, and K. Tanigaki, "Annealing effect on carbon nanotubes," *Chem. Phys. Lett.*, vol. 233, pp. 47–51, 1995.

[47] P. Petit, E. Jouguelet, J. E. Fischer, A. G. Rinzler, and R. E. Smalley, "Electron spin resonance and microwave resistivity of single-wall carbon nanotubes," *Phys. Rev. B*, vol. 56, pp. 9275–9278, 1997.

[48] A. S. Claye, N. M. Nemes, A. Jánossy, and J. E. Fischer, "Structure and electronic properties of potassium-doped single-wall carbon nanotubes," *Phys. Rev. B*, vol. 62, pp. R4845–R4848, 2000.

[49] J.-P. Salvetat, T. Fehér, C. L'Huillier, F. Beuneu, and L. Forró, "Anomalous electron spin resonance behavior of single-wall carbon nanotubes," *Phys. Rev. B*, vol. 72, p. 075440, 2005.

[50] B. Náfrádi, N. M. Nemes, T. Fehér, L. Forró, Y. Kim, J. E. Fischer, D. E. Luzzi, F. Simon, and H. Kuzmany, "Electron spin resonance of single-walled carbon nanotubes and related structures," *phys. stat. sol. (b)*, vol. 243, pp. 3106–3110, 2006.

[51] V. Likodimos, S. Glenis, N. Guskos, and C. L. Lin, "Antiferromagnetic behavior in single-wall carbon nanotubes," *Phys. Rev. B*, vol. 76, p. 075420, 2007.

[52] B. Corzilius, K.-P. Dinse, K. Hata, M. Haluška, V. Skákalová, and S. Roth, "SWNT probed by multi-frequency EPR and nonresonant microwave absorption," *phys. stat. sol. (b)*, vol. 245, pp. 2251–2254, 2008.

[53] N. Ferrer-Anglada, A. A. Monge, and S. Roth, "Electron spin resonance on single-walled carbon nanotubes obtained from different sources," *phys. stat. sol. (b)*, vol. 247, pp. 2823–2826, 2010.

[54] S. Musso, S. Porro, M. Rovere, A. Tagliaferro, E. Laurenti, M. Mann, K. B. K. Teo, and W. I. Milne, "Low temperature electron spin resonance investigation on SWNTs after hydrogen treatment," *Dia. Rel. Mater.*, vol. 15, pp. 1085–1089, 2006.

[55] J. Kombarakkaran and T. Pietraß, "Electron spin resonance studies of hydrogen adsorption on single-walled carbon nanotubes," *Chem. Phys. Lett.*, vol. 452, pp. 152–155, 2008.

[56] R. C. Pastor, J. A. Weil, T. H. Brown, and J. Turkevich, "Narrow electron spin resonance in charred dextrose," *Phys. Rev.*, vol. 102, pp. 918–919, 1956.

[57] G. M. Arnold, "A survey of ESR in heat treated carbon blacks," *Carbon*, vol. 5, pp. 33–42, 1957.

[58] L. S. Singer and I. C. Lewis, "Applications of ESR to carbonaceous materials," *Appl. Spect.*, vol. 36, pp. 52–57, 1982.

[59] S. L. di Vittorio, A. Nakayama, T. Enoki, M. S. Dresselhaus, M. Endo, and N. Shindo, "ESR study of activated carbon fibers: Preliminary results," *J. Mater. Res.*, vol. 8, pp. 2282–2287, 1993.

[60] V. A. Atsarkin, V. V. Demidov, G. A. Vasneva, F. S. Dzheparov, P. J. Ceroke, B. M. Odintsov, and R. B. Clarkson, "Mechanism of oxygen response in carbon-based sensors," *J. Mag. Res.*, vol. 149, pp. 85–89, 2001.

[61] H. J. von Bardeleben, J. L. Cantin, K. Zellama, and A. Zeinert, "Spins and microstructures of amorphous carbon," *Dia. and Rel. Mat.*, vol. 12, pp. 124–129, 2003.

[62] S. S. Rao, A. Stesmans, K. Keunen, D. V. Kosynkin, A. Higginbotham, and J. M. Tour, "Unzipped graphene nanoribbons as sensitive O_2 sensors: Electron spin resonance probing and dissociation kinetics," *Appl. Phys. Lett.*, vol. 98, p. 083116, 2011.

[63] K. Shen, D. L. Tierney, and T. Pietraß, "Electron spin resonance of carbon nanotubes under hydrogen adsorption," *Phys. Rev. B*, vol. 68, p. 165418, 2003.

[64] C. F. M. Clewett, J. Kombarakkaran, and T. Pietraß, "ESR studies of gas adsorption on carbon nanotubes," *phys. stat. sol. (b)*, vol. 243, pp. 3242–3245, 2006.

[65] A. A. Konchits, S. P. Kolesnik, V. S. Yefanov, F. V. Motsnyi, E. Tamburri, and M.-L. Terranova, "ESR study of hydrogen sorption/desorption kinetics in poly(ortho-anisidine) and POA/SWNTs composite films," *Carbon Nanomaterials in Clean Energy Hydrogen Systems*, pp. 241–250, 2008.

[66] N. Bloembergen, E. M. Purcell, and R. V. Pound, "Relaxation effects in nuclear magnetic resonance absorption," *Phys. Rev.*, vol. 73, pp. 679–712, 1948.

[67] R. Kubo and K. Tomita, "A general theory of magnetic resonance absorption," *J. Phys. Soc. Japan*, vol. 9, pp. 888–919, 1954.

[68] F. J. Dyson, "Electron spin resonance absorption in metals. II. Theory of electron diffusion and the skin effect," *Phys. Rev.*, vol. 98, pp. 349–359, 1955.

[69] C. Fantini, A. Jorio, M. Souza, M. S. Strano, M. S. Dresselhaus, and M. A. Pimenta, "Optical transition energies for carbon nanotubes from resonant raman spectroscopy: Environment and temperature effects," *Phys. Rev. Lett.*, vol. 93, p. 147406, 2004.

[70] J. Maultzsch, H. Telg, S. Reich, and C. Thomsen, "Radial breathing mode of single-walled carbon nanotubes: Optical transition energies and chiral-index assignment," *Phys. Rev. B*, vol. 72, p. 205438, 2005.

[71] S. Arepalli, W. A. Holmes, P. Nikolaev, V. G. Hadjiev, and C. D. Scott, "A parametric study of single-wall carbon nanotube growth by laser ablation," *J. Nanosci. Nanotechnol.*, vol. 4, pp. 762–773, 2004.

[72] G. Feher and A. F. Kip, "Electron spin resonance absorption in metals. I. Experimental," *Phys. Rev.*, vol. 98, pp. 337–348, 1955.

[73] N. F. Ramsey, "A molecular beam resonance method with separated oscillating fields," *Phys. Rev.*, vol. 78, pp. 685–699, 1950.

[74] V. Sitaram, A. Sharma, S. V. Bhat, K. Mizoguchi, and R. Menon, "Electron spin resonance studies in the doped polyaniline PANI-AMPSA: Evidence for local ordering from linewidth features," *Phys. Rev. B*, vol. 72, p. 035209, 2005.

[75] F. Beuneu, C. l'Huillier, J.-P. Salvetat, J.-M. Bonard, and L. Forró, "Modification of multiwall carbon nanotubes by electron irradiation: An ESR study," *Phys. Rev. B*, vol. 59, no. 8, pp. 5945–5949, 1999.

[76] F. Demichelis, C. D. Martino, A. Tagliaferro, and M. Fanciulli, "Temperature dependence analysis of the electron paramagnetic resonance signal and electrical conductivity in a-c and a-c:h," *Diam Relat. Mater.*, vol. 3, pp. 844–848, 1994.

[77] G. Wagoner, "Spin resonance of charge carriers in graphite," *Phys. Rev.*, vol. 118, pp. 647–653, 1960.

[78] A. Siegman, *Lasers*. Sausalito, CA USA: University Science Books, 1986.

[79] C. Kittel, *Introduction to Solid State Physics*. John Wiley & Sons, Inc., 7^{th} ed., 1996.

[80] N. Ashcroft and D. Mermin, *Solid State Physics*. Philadelphia, PA USA: Holt, Rinehart, and Winstom, 1976.

[81] P. W. Anderson and P. R. Weiss, "Exchange narrowing in paramagnetic resonance," *Rev. Mod. Phys.*, vol. 25, pp. 269–276, 1953.

[82] P. W. Anderson, "A mathematical model for the narrowing of spectral lines by exchange or motion," *J. Phys. Soc. Japan*, vol. 9, pp. 316–339, 1954.

[83] D. K. Wilson, "Electron spin resonance experiments on shallow donors in germanium," *Phys. Rev.*, vol. 134, pp. A265–A286, 1964.

[84] K. Morigaki and T. Mitsuma, "Electron spin resonance and relaxation effects on donors in stressed Ge," *J. Phys. Soc. Japan*, vol. 20, pp. 62–76, 1965.

[85] G. Feher, "Electron spin resonance experiments on donors in silicon. I. Electronic structure of donors by the electron nuclear double resonance technique," *Phys. Rev.*, vol. 114, pp. 1219–1244, 1959.

[86] S. Maekawa and N. Kinoshita, "Electron spin resonance in phosphorus doped silicon at low temperatures," *J. Phys. Soc. Japan*, vol. 20, pp. 1447–1457, 1965.

[87] Y. Ochiai and E. Matsuura, "ESR in heavily doped *n*-type silicon near a metal-nonmetal transition," *phys. stat. sol. (a)*, vol. 38, pp. 243–252, 1976.

[88] M. Nechtschein, F. Devreux, F. Genoud, M. Guglielmi, and K. Holczer, "Magnetic-resonance studies in undoped trans-polyacetylene $(ch)x$. ii," *Phys. Rev. B*, vol. 27, no. 1, pp. 61–78, 1983.

[89] K. Mizoguchi, S. Masubuchi, K. Kume, K. Akagi, and H. Shirakawa, "Analysis of the ESR linewidth in pristine trans-polyacetylene," *Phys. Rev. B*, vol. 51, pp. 8864–8873, 1995.

[90] C. Gómez-Navarro, P. J. D. Pablo, J. Gómez-Herrero, B. Biel, F. J. Garcia-Vidal, A. Rubio, and F. Flores, "Spin resonance of charge carriers in graphite," *Nat. Mat.*, vol. 4, pp. 534–539, 2005.

[91] K. Matsubara, T. Tsuzuku, and K. Sugihara, "Electron spin resonance in graphite," *Phys. Rev. B*, vol. 44, pp. 11845–11851, 1991.

[92] P. M. Platzman and P. A. Wolff, *Waves and Interactions in Solid State Plasmas*. Solid State Physics, Suppl. 13, New York, NY USA: Academic Press, 1973.

[93] H. Ulbricht, G. Moos, and T. Hertel, "Physisorption of molecular oxygen on single-wall carbon nanotube bundles and graphite," *Phys. Rev. B*, vol. 66, p. 075404, 2002.

[94] R. Larciprete, S. Gardonio, L. Petaccia, and S. Lizzit, "Atomic oxygen functionalization of double walled carbon nanotubes," *Carbon*, vol. 47, pp. 2579–2589, 2009.

[95] P. Giannozzi, R. Car, and G. Scoles, "Oxygen adsorption on graphite and nanotubes," *J. Chem. Phys.*, vol. 118, pp. 1003–1006, 2003.

[96] S. Dag, O. Gülseren, and S. Ciraci, "A comparative study of O_2 adsorbed carbon nanotubes," *Chem. Phys. Lett.*, vol. 380, pp. 1–5, 2003.

[97] S. Dag, O. Gülseren, T. Yildirim, and S. Ciraci, "Oxygenation of carbon nanotubes: Atomic structure, energetics, and electronic structure," *Phys. Rev. B*, vol. 67, p. 165424, 2003.

[98] G. L. Millhauser, W. R. Fiori, and S. M. Miick, "Electron spin labels," *Methods Enzymology*, vol. 246, pp. 589–610, 1995.

[99] N. J. Malmberg, D. R. V. Buskirk, and J. J. Falke, "Membrane-docking loops of the cPLA2 C2 domain: Detailed structural analysis of the protein-membrane interface via site-directed spin-labeling," *Biochemistry*, vol. 42, pp. 13227–13240, 2003.

[100] R. Ahmad and P. Kuppusamy, "Theory, instrumentation, and applications of electron paramagnetic resonance oximetry," *Chem. Rev.*, vol. 110, pp. 3212–3236, 2010.

[101] E. Houzé and M. Nechtschein, "ESR in conducting polymers: Oxygen-induced contribution to the linewidth," *Phys. Rev. B*, vol. 53, no. 21, pp. 14309–14318, 1996.

[102] M. Grujicica, G. Caoa, and R. Singh, "The effect of topological defects and oxygen adsorption on the electronic transport properties of single-walled carbon-nanotubes," *Appl. Surf. Sci.*, vol. 211, pp. 166–183, 2003.

[103] T. Savage, S. Bhattacharya, B. Sadanadan, J. Gaillard, T. M. Tritt, Y.-P. Sun, Y. Wu, S. Nayak, R. Car, N. Marzari, P. M. Ajayan, and A. M. Rao, "Photoinduced oxidation of carbon nanotubes," *J. Phys.: Cond. Matt.*, vol. 15, pp. 5915–5921, 2003.

[104] S.-H. Jhi, S. G. Louie, and M. L. Cohen, "Electronic properties of oxidized carbon nanotubes," *Phys. Rev. Lett.*, vol. 85, pp. 1710–1713, 2000.

[105] A. M. Portis, "Electronic structure of f centers: Saturation of the electron spin resonance," *Phys. Rev.*, vol. 91, p. 1071, 1953.

[106] R. T. Weber, S. S. Eaton, and G. R. Eaton, "Workship on Selecting an EPR Resonator: 28th International EPR Symposium," July 2005.

[107] B. M. Khabibullin and E. Kharakhash'yan, "Conduction-electron paramagnetic resonance in metals," *Sov. Phys.-Usp.*, vol. 16, pp. 806–818, 1973.

[108] S. W. Koch, M. Kira, G. Khitrova, and H. M. Gibbs, "Semiconductor excitons in new light," *Nat. Mat.*, vol. 5, pp. 523–531, 2006.

[109] E. M. Gershenzon, G. N. Gol'tsman, and N. G. Ptitsina, "Investigation of free excitons in Ge and their condensation at submillimeter wavelengths," *Zh. Eksp. Teor. Fiz.*, vol. 70, p. 224, 1976.

[110] T. Timusk, H. Navarro, N. O. Lipari, and M. Altarelli, "Far-infrared absorption by excitons in silicon," *Solid State Comm.*, vol. 25, pp. 217–219, 1978.

[111] D. Labrie, M. L. W. Thewalt, I. J. Booth, and G. Kirczenow, "Detailed ground- and excited-state spectroscopy of indirect free excitons," *Phys. Rev. Lett.*, vol. 61, p. 1882, 1988.

[112] C. C. Hodge, C. C. Phillips, M. S. Skolnick, G. W. Smith, C. R. Whitehouse, P. Dawson, and C. T. Foxon, "Induced absorption spectroscopic determination of exciton binding energies in type-II GaAs/AlAs superlattices," *Phys. Rev. B*, vol. 41, p. 12319, 1990.

[113] R. H. M. Groeneveld and D. Grischkowsky, "Picosecond time-resolved far-infrared experiments on carriers and excitons in GaAs-AlGaAs multiple quantum wells," *J. Opt. Soc. Am. B*, vol. 11, p. 2502, 1994.

[114] J. Černe, J. Kono, M. S. Sherwin, M. Sundaram, A. C. Gossard, and G. E. W. Bauer, "Terahertz dynamics of excitons in GaAs/AlGaAs quantum wells," *Phys. Rev. Lett.*, vol. 77, pp. 1131–1134, Aug 1996.

[115] M. S. Salib, H. A. Nickel, G. S. Herold, A. Petrou, B. D. McCombe, R. Chen, K. K. Bajaj, and W. Schaff, "Observation of internal transitions of confined excitons in GaAs/AlGaAs quantum wells," *Phys. Rev. Lett.*, vol. 77, p. 1135, 1996.

[116] J. Kono, M. Y. Su, T. Inoshita, T. Noda, M. S. Sherwin, S. J. Allen, Jr., and H. Sakaki, "Resonant terahertz optical sideband generation from confined magnetoexcitons," *Phys. Rev. Lett.*, vol. 79, pp. 1758–1761, 1997.

[117] R. A. Kaindl, M. A. Carnahan, D. Hägele, R. Lövenich, and D. S. Chemla, "Ultrafast terahertz probes of transient conducting and insulating phases in an electron-hole gas," *Nature*, vol. 423, pp. 734–738, 2003.

[118] M. Kubouchi, K. Yoshioka, R. Shimano, A. Mysyrowicz, and M. Kuwata-Gonokami, "Study of orthoexciton-to-paraexciton conversion in Cu_2O by excitonic lyman spectroscopy," *Phys. Rev. Lett.*, vol. 94, p. 016403, 2005.

[119] R. Huber, B. A. Schmid, Y. R. Shen, D. S. Chemla, and R. A. Kaindl, "Stimulated terahertz emission from intraexcitonic transitions in Cu_2O," *Phys. Rev. Lett.*, vol. 96, p. 017402, 2006.

[120] S. Leinß, T. Kampfrath, K. v.Volkmann, M. Wolf, J. T. Steiner, M. Kira, S. W. Koch, A. Leitenstorfer, and R. Huber, "Terahertz coherent control of optically dark paraexcitons in Cu_2O," *Phys. Rev. Lett.*, vol. 101, p. 246401, 2008.

[121] M. Wagner, H. Schneider, D. Stehr, S. Winnerl, A. M. Andrews, S. Schartner, G. Strasser, and M. Helm, "Observation of the intraexciton Autler-Townes effect in

GaAs/AlGaAs semiconductor quantum wells," *Phys. Rev. Lett.*, vol. 105, p. 167401, 2010.

[122] J. Lee, T. H. Myers, N. C. Giles, B. E. Dean, and C. J. Johnson, "Optical quenching of bound excitons in CdTe and $Cd_{1-x}Zn_xTe$ alloys: A technique to measure copper concentration," *J. Appl. Phys.*, vol. 76, pp. 537–541, 1994.

[123] J. Kono, S. T. Lee, M. S. Salib, G. S. Herold, A. Petrou, and B. D. McCombe, "Optically detected far-infrared resonances in doped GaAs quantum wells," *Phys. Rev. B*, vol. 52, pp. R8654–R8657, 1995.

[124] S. Zybell, H. Schneider, S. Winnerl, M. Wagner, K. Köhler, and M. Helm, "Photoluminescence dynamics in GaAs/AlGaAs quantum wells under pulsed intersubband excitation," *Appl. Phys. Lett.*, vol. 99, p. 041103, 2011.

[125] M. Kira, F. Jahnke, and S. W. Koch, "Microscopic theory of excitonic signatures in semiconductor photoluminescence," *Phys. Rev. Lett.*, vol. 81, pp. 3263–3266, 1998.

[126] J. H. M. Oestreich, D. Hagele and W. W. Ruhle, "Excitons, or no excitons, that is the question," *phys. stat. sol. (a)*, vol. 178, pp. 27–32, 2000.

[127] J. Szczytko, L. Kappei, J. Berney, F. Morier-Genoud, M. T. Portella-Oberli, and B. Deveaud, "Determination of the exciton formation in quantum wells from time-resolved interband luminescence," *Phys. Rev. Lett.*, vol. 93, p. 137401, 2004.

[128] S. Chatterjee, C. Ell, S. Mosor, G. Khitrova, H. M. Gibbs, W. Hoyer, M. Kira, S. W. Koch, J. P. Prineas, and H. Stolz, "Excitonic photoluminescence in semiconductor quantum wells: Plasma versus excitons," *Phys. Rev. Lett.*, vol. 92, p. 067402, 2004.

[129] I. Galbraith, R. Chari, S. Pellegrini, P. J. Phillips, C. J. Dent, A. F. G. van der Meer, D. G. Clarke, A. K. Kar, G. S. Buller, C. R. Pidgeon, B. N. Murdin, J. Allam, and G. Strasser, "Excitonic signatures in the photoluminescence and terahertz absorption of a GaAs/$Al_xGa_{1-x}As$ multiple quantum well," *Phys. Rev. B*, vol. 71, p. 073302, 2005.

[130] S. M. Quinlan, A. Nikroo, M. S. Sherwin, M. Sundaram, and A. C. Gossard, "Photoluminescence from $Al_xGa_{1-x}As$/GaAs quantum wells quenched by intense far-infrared radiation," *Phys. Rev. B*, vol. 45, pp. 9428–9431, 1992.

[131] J. Černe, A. G. Markelz, M. S. Sherwin, S. J. Allen, M. Sundaram, A. C. Gossard, P. C. van Son, and D. Bimberg, "Quenching of excitonic quantum-well photoluminescence by intense far-infrared radiation: Free-carrier heating," *Phys. Rev. B*, vol. 51, pp. 5253–5262, 1995.

[132] J. Liu, G. Kaur, and X.-C. Zhang, "Photoluminescence quenching dynamics in cadmium telluride and gallium arsenide induced by ultrashort terahertz pulse," *Appl. Phys. Lett.*, vol. 97, p. 111103, 2010.

[133] J. Lee, G. T. Noe, Y. Wang, C. J. Stanton, G. S. Solomon, A. A. Belyanin, D. H. Reitze, and J. Kono, "Robust, stable single-exciton emission from an ultrahigh-density magneto-plasma," *arXiv*, vol. 1009.3067, 2011.

[134] W. D. Rice, S. Zybell, S. Winnerl, H. Schneider, M. Helm, L. Schneebeli, B. Breddermann, M. Kira, S. W.Koch, and J. Kono, "Terahertz-radiation-induced exciton shelving and intra-excitonic scattering," *arXiv*, vol. 1203.3994v1, 2012.

[135] Y. P. Varshni, "Temperature dependence of the energy gap in semiconductors," *Physica*, vol. 34, pp. 149–154, 1967.

[136] S. Adachi, *Optical Properties of Crystalline and Amorphous Semiconductors: Materials and Fundamental Principles*. Norwell, MA USA: Kluwer Academic Publishers, 1999.

[137] N. Peyghambarian, S. W. Koch, and A. Mysyrowicz, *Introduction to Semiconductor Optics*. Prentice Hall, 1st ed., 1993.

[138] M. Kira and S. W. Koch, "Exciton-population inversion and terahertz gain in semiconductors excited to resonance," *Phys. Rev. Lett.*, vol. 93, p. 076402, 2004.

[139] M. Kira and S. W. Koch, "Many-body correlations and excitonic effects in semiconductor spectroscopy," *Prog. Quantum Electron.*, vol. 30, p. 155, 2006.

[140] E. D. Palik, ed., *Handbook of Optical Constants of Solids*. Orlando, FL: Academic Press, Inc., 1985.

[141] J. Mompart and R. Corbalan, "Lasing without inversion," *J. Opt. B*, vol. 2, pp. R7–R24, 2000.

[142] K.-J. Boller, A. Imamoğlu, and S. E. Harris, "Observation of electromagnetically induced transparency," *Phys. Rev. Lett.*, vol. 66, pp. 2954–2956, 1991.

[143] D. H. Dunlap and V. M. Kenkre, "Dynamic localization of a charged particle moving under the influence of an electric field," *Phys. Rev. B*, vol. 34, pp. 3625–3633, 1986.

[144] A. Srivastava, R. Srivastava, J. Wang, and J. Kono, "Laser-induced above-band-gap transparency in GaAs," *Phys. Rev. Lett.*, vol. 93, p. 157401, 2004.

[145] F. Grossmann, T. Dittrich, P. Jung, and P. Hänggi, "Coherent destruction of tunneling," *Phys. Rev. Lett.*, vol. 67, pp. 516–519, 1991.

[146] M. Holthaus, "Collapse of minibands in far-infrared irradiated superlattices," *Phys. Rev. Lett.*, vol. 69, pp. 351–354, 1992.

[147] M. Holthaus, "Strongly driven semiconductor quantum wells: New testing ground for "quantum chaos"?," *Prog. Theor. Phys. Suppl.*, vol. 116, pp. 417–423, 1994.

[148] T. Oka and H. Aoki, "Photovoltaic Hall effect in graphene," *Phys. Rev. B*, vol. 79, p. 081406, 2009.

[149] J. Inoue and A. Tanaka, "Photoinduced transition between conventional and topological insulators in two-dimensional electronic systems," *Phys. Rev. Lett.*, vol. 105, p. 017401, 2010.

[150] H. L. Calvo, H. M. Pastawski, S. Roche, and L. E. F. Foa Torres, "Tuning laser-induced band gaps in graphene," *Appl. Phys. Lett.*, vol. 98, p. 232103, 2011.

[151] N. H. Lindner, G. Refael, and V. Galitski, "Floquet topological insulator in semiconductor quantum wells," *Nat. Phys.*, vol. 7, pp. 490–495, 2011.

[152] B. Dóra, J. Cayssol, F. Simon, and R. Moessner, "Optically engineering the topological properties of a spin Hall insulator," *Phys. Rev. Lett.*, vol. 108, p. 056602, 2012.

[153] P. R. Wallace, "The band theory of graphite," *Phys. Rev.*, vol. 71, pp. 622–634, 1947.

[154] A. K. Geim and K. S. Novoselov, "The rise of graphene," *Nature*, vol. 6, pp. 183–191, 2007.

[155] R. E. Peierls, "Quelques proprietes typiques des corpses solides," *Ann. I. H. Poincare*, vol. 5, pp. 177–222, 1935.

[156] L. D. Landau, "Zur theorie der phasenumwandlungen II," *Phys. Z. Sowjetunion*, vol. 11, pp. 26–35, 1937.

[157] S. Iijima, "Helical microtubules of graphitic carbon," *Nature*, vol. 354, pp. 56–58, 1991.

[158] M. Freitag, "Graphene: Nanoelectronics goes flat out," *Nat. Nano.*, vol. 3, pp. 455–457, 2008.

[159] K. S. Novoselov, A. K. Geim, S. V. Morozov, D. Jiang, Y. Zhang, S. V. Dubonos, I. V. Grigorieva, and A. A. Firsov, "Electric field effect in atomically thin carbon films," *Science*, vol. 306, pp. 666–669, 2004.

[160] Y. Zhang, Y.-W. Tan, H. L. Stormer, and P. Kim, "Experimental observation of the quantum Hall effect and Berry's phase in graphene," *Nature*, vol. 438, pp. 201–204, 2005.

[161] R. R. Nair, P. Blake, A. N. Grigorenko, K. S. Novoselov, T. J. Booth, T. Stauber, N. M. R. Peres, and A. K. Geim, "Fine structure constant defines visual transparency of graphene," *Science*, vol. 320, p. 1308, 2008.

[162] K. F. Mak, M. Y. Sfeir, Y. Wu, C. H. Lui, J. A. Misewich, and T. F. Heinz, "Measurement of the optical conductivity of graphene," *Phys. Rev. Lett.*, vol. 101, p. 196405, 2008.

[163] K. S. Novoselov, A. K. Geim, S. V. Morozov, D. Jiang, M. I. Katsnelson, I. V. Grigorieva, S. V. Dubonos, and A. A. Firsov, "Two-dimensional gas of massless Dirac fermions in graphene," *Nature*, vol. 438, pp. 197–200, 2005.

[164] S. V. Syzranov, M. V. Fistul, and K. B. Efetov, "Effect of radiation on transport in graphene," *Phys. Rev. B*, vol. 78, p. 045407, 2008.

[165] K. P. Cheung and D. H. Auston, "Excitation of coherent phonon polaritons with femtosecond optical pulses," *Phys. Rev. Lett.*, vol. 55, pp. 2152–2155, 1985.

[166] K. P. Cheung and D. H. Auston, "A novel technique for measuring far-infrared absorption and dispersion," *Infrared Phys.*, vol. 26, pp. 23–27, 1986.

[167] P. R. Smith, D. H. Auston, and M. C. Nuss, "Subpicosecond photoconducting dipole antennas," *J. Quant. Electron.*, vol. 24, pp. 255–260, 1988.

[168] C. Fattinger and D. Grischkowsky, "Terahertz beams," *Appl. Phys. Lett.*, vol. 54, p. 490, 1989.

[169] Y.-R. Shen, "Far-infrared generation by optical mixing," *Prog. Quantum Electron.*, vol. 4, pp. 207–232, 1976.

[170] F. Zernike and P. R. Berman, "Generation of far infrared as a difference frequency," *Phys. Rev. Lett.*, vol. 15, pp. 999–1001, 1965.

[171] J. R. Morris and Y. R. Shen, "Theory of far-infrared generation by optical mixing," *Phys. Rev. A*, vol. 15, pp. 1143–1156, 1977.

[172] X.-C. Zhang, X. F. Ma, Y. Jin, T.-M. Lu, E. P. Boden, P. D. Phelps, K. R. Stewart, and C. P. Yakymyshyn, "Terahertz optical rectification from a nonlinear organic crystal," *Appl. Phys. Lett.*, vol. 61, p. 3080, 1992.

[173] T. J. Carrig, G. Rodriguez, T. S. Clement, A. J. Taylor, and K. R. Stewart, "Scaling of terahertz radiation via optical rectification in electrooptic crystals," *Appl. Phys. Lett.*, vol. 66, p. 121, 1995.

[174] R. Huber, A. Brodschelm, F. Tauser, and A. Leitenstorfer, "Generation and field-resolved detection of femtosecond electromagnetic pulses tunable up to 41 THz," *Appl. Phys. Lett.*, vol. 76, p. 3191, 2000.

[175] A. Nahata, H. Cao, and T. F. Heinz, "Deeper into the infrared," *IEEE Circuits and Devices*, vol. 2, pp. 32–39, 2002.

[176] M. Bass, P. A. Franken, J. F. Ward, and G. Weinreich, "Optical rectification," *Phys. Rev. Lett.*, vol. 9, pp. 446–448, 1962.

[177] E. Hecht, *Optics*. Reading, MA USA: Addison Wesley, 4$^{\text{th}}$ ed., 2002.

[178] Z. Jiang and X.-C. Zhang, *Sensing with Terahertz Radiation*, vol. 85 of *Optical Sciences*, ch. Free-Space Electro-Optic Techniques, pp. 155–192. Berlin: Springer, 2003.

[179] M. Weissbluth, *Photon-Atom Interactions*. San Diego, CA USA: Academic Press, 1989.

[180] M. Fox, *Quantum Optics: An Introduction*. New York, NY USA: Oxford University Press, 2006.